Hadronic final states in diffractive pp scattering at $\sqrt{s} = 13$ TeV using the ATLAS detector

By

Sabina Czekierda

The H. Niewodniczański Institute of Nuclear Physics
Polish Academy of Sciences

A dissertation submitted for the degree of
Doctor of Philosophy in Physics

Prepared under the supervision of
thesis supervisor: Prof. Janusz Chwastowski
auxiliary supervisor: Dr. Rafał Staszewski

Kraków 2019

"I never guess. It is a capital mistake to theorize before one has data. Insensibly one begins to twist facts to suit theories, instead of theories to suit facts."

Sir Arthur Conan Doyle

ABSTRACT

This thesis is devoted to a study of the charged particle distributions in diffractive events. Diffractively scattered protons were tagged using a dedicated forward detector of the ATLAS experiment at the LHC, the AFP detector. This detector was installed in the LHC tunnel in 2016. The present analysis was performed using the data sample corresponding to an integrated luminosity of 51 nb^{-1} of proton–proton collisions at the centre-of-mass energy of 13 TeV, collected in 2017. It is worth to emphasize that this is the first physical analysis using data collected by the AFP detector.

The charged particle multiplicities, their transverse momenta and pseudorapidities were measured. The measurements were performed in different regions of the relative energy loss of diffractively scattered protons. Events were selected by asking at least one primary stable charged particle with a transverse momentum of at least 500 MeV and the absolute value of pseudorapidity smaller than 2.5. The relative energy loss range of diffractively scattered protons in this dissertation is between 0.035 and 0.08 what can be translated into the diffractive mass ranges of 2.4 TeV and 3.7 TeV. The measured distributions were corrected for two estimated kinds of background. Corrections related to the vertex and track reconstruction efficiences were applied. Finally, the obrained distributions were compared with the results offered by two Monte Carlo generators, PYTHIA 8.2 and EPOS.

STRESZCZENIE

Niniejsza praca doktorska jest poświęcona badaniom rozkładów cząstek naładowanych produkowanych w oddziaływaniach dyfrakcyjnych proton-proton zachodzących na akceleratorze LHC. Jedną z sygnatur takich oddziaływań jest nietknięty, lecz spowolniony proton poruszający się w przód pod bardzo małym kątem względem osi wiązki, tzw. *proton rozproszony dyfrakcyjnie*. W danych użytych w tej pracy protony dyfrakcyjne były rejestrowane przez specjalnie do tego celu skonstruowane detektory AFP, stanowiące jeden z poddetektorów eksperymentu ATLAS. Zostały one zainstalowane w tunelu LHC w 2016 roku.

Analiza przeprowadzona w niniejszej pracy jest oparta na danych o scałkowanej świetlności wynoszącej około 51 nb^{-1}, pochodzących z oddziaływań proton–proton zachodzących przy energii w układzie środka masy równej 13 TeV. Zostały one zebrane podczas jednego z tzw. *runów* w 2017 roku. Warto podkreślić, że jest to pierwsza analiza fizyczna wykorzystująca dane zebrane przez detektory AFP.

W tej rozprawie zmierzono rozkłady cząstek naładowanych produkowanych w centralnej części detektora ATLAS. Rozkłady te przedstawiają krotności produkowanych cząstek, ich pędy poprzeczne oraz zmienną *pseudorapidity*, mówiącą o rozkładzie kątowym cząstek. Domyślny obszar, w którym mierzone są rozkłady cząstek, odpowiada względnej stracie energii protonu dyfrakcyjnego wynoszącej 3,5 – 8%. Dodatkowo zakres ten został podzielony na trzy podobszary równej szerokości, w których również zostały zmierzone wspomniane wcześniej rozkłady cząstek.

W analizie akceptowano przypadki, w których wymagano, aby pęd poprzeczny cząstki był większy od 500 MeV i by wartość bezwzględna *pseudorapidity* była mniejsza niż 2,5. Zmierzone rozkłady zostały poprawione ze względu na obecność tła. Zastosowano również poprawki związane z efektywnością rekonstrukcji wierzchołków i śladów oraz akceptancją detektorów. Przewidywania dwóch modeli oddziaływań: PYTHIA 8.2 i EPOS zostały porównane do danych.

ACKNOWLEDGEMENTS

This thesis was funded by the Henryk Niewodniczański Institute of Nuclear Physics Polish Academy of Sciences. The Author of this thesis was granted the KNOW scholarship and financial support within the NCN grant 2015/19/B/ST2/00989.

First of all, I would like to express my gratitude to my supervisors: Prof. Janusz Chwastowski and Dr. Rafał Staszewski for their guidance and attention throughout my whole PhD studies. The special thanks to Dr. Rafał Staszewski for many hours of stimulating discussions. I especially appreciate that he often did not answer my questions directly but encouraged me to think myself.

I would also like to thank my colleague collaborator Krzystof Cieśla with admirable programming skills. Thank you Krzysztof for always having time to rescue me when all hope seemed lost.

My research would have been impossible without the aid and support of the AFP community. Naming the closest collaborators, acknowledgements to Dr. Maciej Trzebiński for his help on the detector operation side. To Dr. Eng. Elżbieta Banaś who introduced me to the DCS world and was constantly checking whether I got lost in it. To Dr. Eng. Leszek Adamczyk for keeping a watchful eye on my results.

Last but not least, a very special thank you to Dr. Eng. Grzegorz Gach who was taking care of the quality of the data that I was working on and helped me a lot on the programming side. You made the challenging time of writing this dissertation a way better. You make every day of my life much better.

Dedicated to my beloved and dearest future husband

TABLE OF CONTENTS

CHAPTER 1

INTRODUCTION

The advent of particle physics can be associated with discovery of the electron by Joseph John Thomson in 1897 and thus proving that the concept of indivisible atoms suggested by John Dalton is incorrect. The 1913 discovery of isotops by Frederick Soddy and Joseph John Thomson prompted Ernest Rutherford to suppose that all nuclei besides hydrogen contain chargeless particles, which he named the neutrons. In 1918 Ernest Rutherford established that the hydrogen nucleus is a particle with positive charge, which he named the proton.

In 1950s came the era of particle accelerators, with energies of about hundreds of MeV. It brought the time of discoveries of short-lived resonances. A little later, improvements in particle accelerators and particle detectors led to a bewildering variety of particles found in high-energy experiments.

In 1970s the theory describing strong interactions, Quantum Chromodynamics (QCD), was established. It describes the strong interaction in terms of exchanges of gluons between quarks that are also constituents of hadrons. This theory widely exploits methods offered by the perturbative approach. However, the perturbative theory breaks down in certain kinematic regions. They are known as "soft" and are currently described by different models. Studies of the regions where the perturbative theory starts to break can broaden the scope of knowledge about strong interactions. One of the processes that stretches from perturbative to soft region is the diffractive scattering.

Diffractive events were discovered in early pp experiments at the SPS accelerator at CERN. This discovery was confirmed later at HERA, Tevatron and also many fixed target experiments. These events were characterized by large regions of the detector completely devoid of particles and some could be associated with “hard” interactions, i.e. photoproduction of jets or heavy mesons. The biggest surprise were the results from ep collisions at HERA, where about 10% of hard events were of the diffractive nature. In $p\overline{p}$ collisions at Tevatron the observed fraction was lower, about 1%. This difference brought in a concept of the gap survival probability and is related to the re-scattering and other final state effects.

Recently, at the LHC, another possibility of detection of diffractive events was revived. Another signature of such events, apart from large rapidity gap(s), is the presence of the intact forward scattered particle. Forward detectors, like the AFP detector discussed in this dissertation, installed far away from the interaction point, allow the registration of intact protons scattered at very small angles.

Determination of kinematics of a surviving particle allows constraining the models of phenomena that are still not fully understood. Additionally, a tag on forward protons enables studies of central exclusive processes, like exclusive production of di-jets, lepton pairs and others.

In this thesis the diffractive events at the centre-of-mass energy of $\sqrt{s} = 13$ TeV were studied, with a particular emphasis on the distributions of charged particles produced within these interactions and registered by the ATLAS central detector. Signature of a forward proton in diffractive events is exploited in the signal sample selection. It is worth stressing that this dissertation presents first results of measurements based on the AFP detector.

The thesis is organised as follows. Chapter 2 introduces the theoretical framework of diffractive physics. It begins with a description of interaction governing the diffractive events – the strong interaction, described by QCD. Then soft diffraction processes studied in this thesis and their mechanisms are presented, including a brief description of Regge theory. Next, various types of hard diffraction are considered. Finally, the used Monte Carlo generators are introduced, PYTHIA 8.2 and EPOS.

Chapter 3 is devoted to the experimental apparatus description. It starts with a characterization of the LHC. The structure of the beam is featured. Then, the ATLAS Detector and its main components are outlined. The ATLAS forward detectors are described in greater details, with a special emphasis on the AFP detectors dedicated to the diffractive measurements.

Chapter 4 is dedicated to the explanation of the event reconstruction procedure, starting with the track and vertex reconstruction using the ATLAS Inner Detector. Then, the reconstruction of the calorimeter clusters is briefly described. The last part of this chapter is devoted to a detailed description of objects reconstructed using the AFP detectors and the alignment of these detectors.

Starting from Chapter 5 the physics analysis is covered. At first, the data sample is discussed. The AFP detector performance plots are presented both for the data and PYTHIA 8.2 Monte Carlo and compared. Subsequently, the signal sample selection is introduced and the detector level distributions of the charged particles produced within the ATLAS Inner Detector acceptance are presented.

Chapter 6 is devoted to the description of the corrections for the ATLAS detector inefficiencies, including the vertex and track reconstruction efficiencies. Chapters 7 and 8 are dedicated to the estimation of the backgrounds. In Chapter 9 the unfolding procedure of the multiplicity distribution is described. Finally, results are presented in Chapter 10.

The thesis is closed with a summary and conclusions (Chapter 11). Different data and Monte Carlo selections used for different purposes within the whole analysis part are summarized in Appendix A. Two methods of the estimation of the MBTS detector inefficiency are described in details in Appendix B.

The developed methods of the estimation of two types of background are the author's original work. They are fully data driven and can be used in other future analysis. All corrections for the MBTS trigger inefficiency were designed and implemented by the author. Also the unfolding procedure was implemented by the author. During the entire PhD studies, the author was a member of the AFP Detector Control System (DCS) team and was responsible for the design and implementation of the AFP DCS FSM panels – they are presented in Appendix C. The author participated also in one of the tests of the AFP detector on the beam.

CHAPTER 2

THEORETICAL FRAMEWORK

The Standard Model (SM) of particle physics includes all known elementary particles and describes their interactions. It comprises three of the four known forces: the electromagnetic, weak and strong. The description of gravity is still not incorporated. The Standard Model is a theory of interacting quantum fields. Excitations of the fields are related to particles and each particle type corresponds to a separate field. These particles, except for the Higgs boson, can be classified into three groups: quarks, leptons and gauge bosons (see Fig. 2.1). The Higgs field is responsible for the mass of other particles.

Quantum Electrodynamics (QED) is the gauge theory of electromagnetism which describes the interaction of charged particles via exchange of a photon. The weak interaction, describing interactions between fermions (quarks and leptons) through mediating charged or neutral gauge bosons ($W^{\pm}$ or Z^0, respectively), can be unified with electromagnetism and they are jointly described by the electroweak theory.

2.1 Strong interactions

Quantum Chromodynamics describes the strong interactions through the exchange of massless color mediators called gluons. As an analogy to the electic charge in QED, the property of *color* was suggested. Combination of the three colors (red, green and blue) yields a neutral color. A combination of a color and a corresponding anti-color also results in a neutral color. The quarks carry color while gluons carry an octet combination of color and anti-color. Thanks to that feature, gluons may interact with each other. However, the gluons may group in a way that their color charges add up forming a color singlet. A neutral object like this behaves in a different way than single gluon with a color charge.

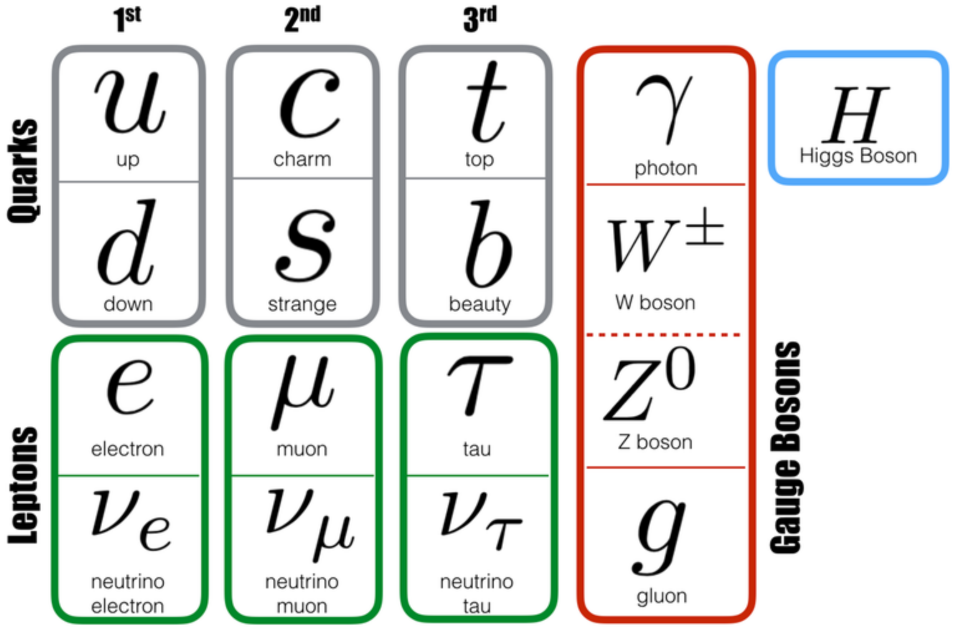

Figure 2.1: The elementary particles of the Standard Model. From [1].

The range of the strong force is of the order of 10^{-15} m. Strong interactions are responsible for the existence of nuclei and hadrons. Hadrons are particles consisting of two or three (anti)quarks and can be further distinguished into mesons and baryons. All hadrons are color singlets. Mesons, like pions, consist of a linear combination of pairs of a quark and an anti-quark. Baryons, like protons and neutrons, consist of three quarks.

The strength of the interaction is governed by the strong coupling constant, α_S, whose value is in fact not constant but depends on the distance between the interacting particles. With increasing value of the scale (shorter distances), α_S gets smaller (see Fig. 2.2) which is a signature of the *asymptotic freedom*. For small scales, α_S value is large and the strong interaction bounds *partons* (quarks and gluons) inside hadrons tightly. This phenomenon is known as *confinement*. Colored partons are thus never observed as free.

There is another interesting feature of strong interactions. One can imagine two color charges (for instance a $q\overline{q}$ pair) as held together by a spring. A tension of this spring decreases while bringing the quarks closer to each other. When the quarks are separated then the spring tension gets larger and in some conditions the spring breaks which corresponds to a creation of a new $q\overline{q}$ pair. This phenomenon is called hadronization and it is schematically presented in Fig. 2.3. In general, it is repeated many times, resulting in a jet of different hadrons in a cone around the original direction of a quark.

The structure of hadrons may be probed in collider experiments. When a probe strucks a parton inside a hadron, for instance inside a proton, the parton may be scattered off at large transverse momentum and makes the rest of the hadron system colorful. The proton

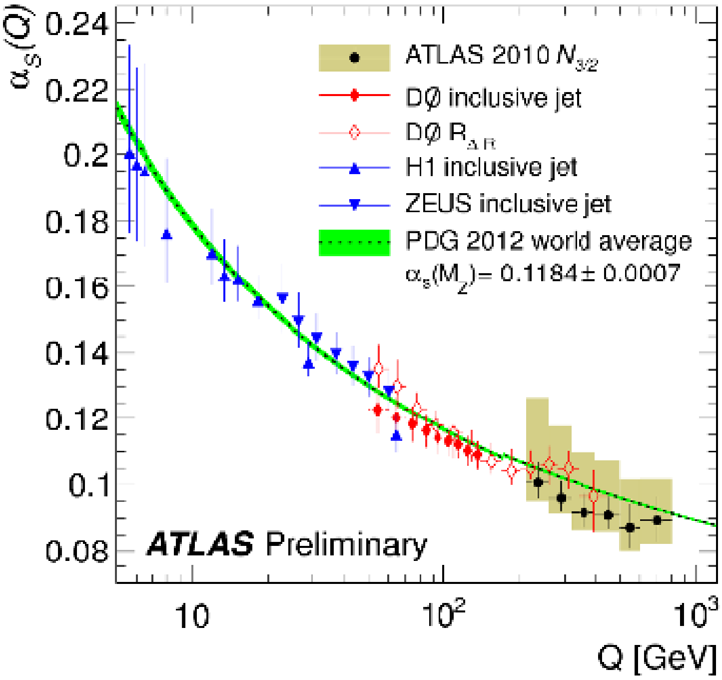

Figure 2.2: Measurement of the strong coupling constant α_S as a function of the scale (exchanged momentum) Q for the ATLAS, D0, ZEUS and H1 experiments. From [2].

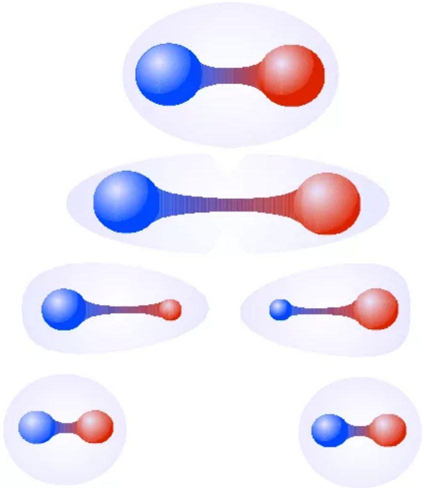

Figure 2.3: Scheme of hadronization. Blue and red balls represent the quarks and anti-quarks. Their separation increases the energy of the color field what allows production of another $q\bar{q}$ pair. From [3].

is broken up and the system has to reconfigure its color field as only colorless states can be observed. Consequently, some number of particles with small transverse momenta called the *proton remnants* leave the interaction.

2.2 Diffractive dissociation

2.2.1 Soft Diffraction

The phenomenon of diffractive dissociation was predicted in 1960 by Good and Walker [4]. They suggested what nowadays is called a *soft diffraction*. In case of hadron–hadron collisions, which are driven by a strong force, one can imagine it as a quasi-elastic scattering between two hadrons where one of the hadrons is excited into a higher mass state retaining its quantum numbers [5]. It requires small transverse and longitudinal momentum transfers between colliding hadrons.

A diffractive collision is characterized by an exchange of a color singlet state consisting of gluons and quarks, called a Pomeron. This exchange is colorless and with the quantum numbers of the vacuum. As a result, a region of rapidity devoid of particles may be observed, the so-called *rapidity gap*.

Four types of diffractive events can be distinguished:

(a) elastic scattering,

(b) single-diffractive dissociation,

(c) double-diffractive dissociation,

(d) central diffraction.

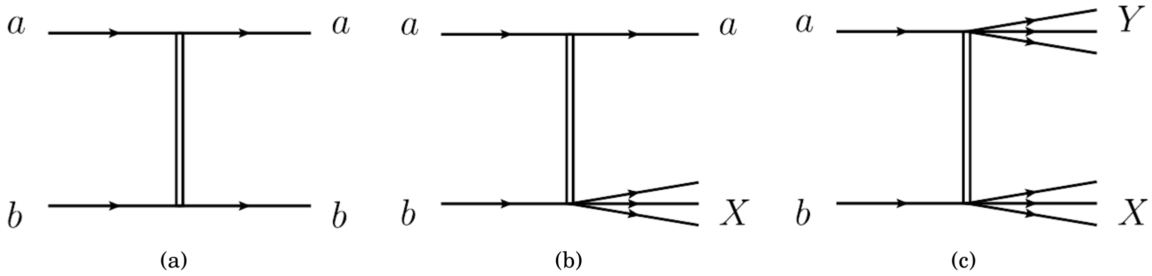

(a) (b) (c)

Figure 2.4: Feynman diagrams of some of the diffractive scattering processes: (a) elastic scattering, (b) single-diffractive dissociation, (c) double-diffractive dissociation. The double line represents the Pomeron exchange. From [6].

Elastic scattering

In elastic scattering the initial and final state particles are identical. It is a binary process, $2 \to 2$:

$$a + b \to a + b\,. \tag{2.1}$$

The diagram representing this process is shown in Fig. 2.4(a). Elastic interaction may be governed not only by the strong force but also by the electromagnetic one, especially at small values of the four-momentum transfer, t. Then, instead of a Pomeron, a photon is exchanged.

Single-diffractive dissociation

Single-diffractive dissociation (called also single diffraction) is a process in which one of the initial particles dissociates into a system X, which carries quantum numbers of parent particle, while the second particle remains intact. Spin and parity of system X may differ from those of an initial particle as some orbital angular momentum can be transferred to X in the collision [7]. The process can be expressed as:

$$a + b \rightarrow a + X\,. \tag{2.2}$$

The diagram representing it is shown in Fig. 2.4(b). The intact, difractively scattered particle will be refffered to as a *diffractively scattered proton* in case of a proton–proton collisions. It is emitted at very small angles, of the order of microradians, with respect to its original direction. This region is called a *forward region* thus the diffractively scattered particle is often reffered to as a *forward particle*. In the forward region the rapidity gap is produced, separating the diffractively scattered particle and the dissociated system.

In order to describe this process, the relative energy loss ξ of a diffractively scattered particle is defined as:

$$\xi = \frac{E_0 - E}{E_0}\,, \tag{2.3}$$

where E_0 and E are the initial and the final energies of the diffractively scattered particle, respectively. The invariant mass, M_{X}, of the multi-particle system X may take quite large values and is given by:

$$M_{\mathrm{X}}^2 \approx \xi \cdot s\,. \tag{2.4}$$

An interesting feature of that process is that the differential $d\sigma/d\xi$ distribution exhibits the form of $1/\xi$ [8]. This behaviour can be seen in Fig. 2.5 presenting the differential cross section as a function of $\log\xi$ for the single-diffractive dissociation. A consequence of this behaviour is that the differential cross section $d\sigma/dM_X^2$ is proportional to $1/M_X^2$.

Double-diffractive dissociation

Double-diffractive dissociation (called also double diffraction) is a process in which both colliding particles dissociate into systems X and Y:

$$a + b \rightarrow Y + X\,. \tag{2.5}$$

The diagram representing this process is shown in Fig. 2.4(c). Each of the dissociated systems carries the quantum numbers of its parent particle. The systems are separated by a central rapidity gap.

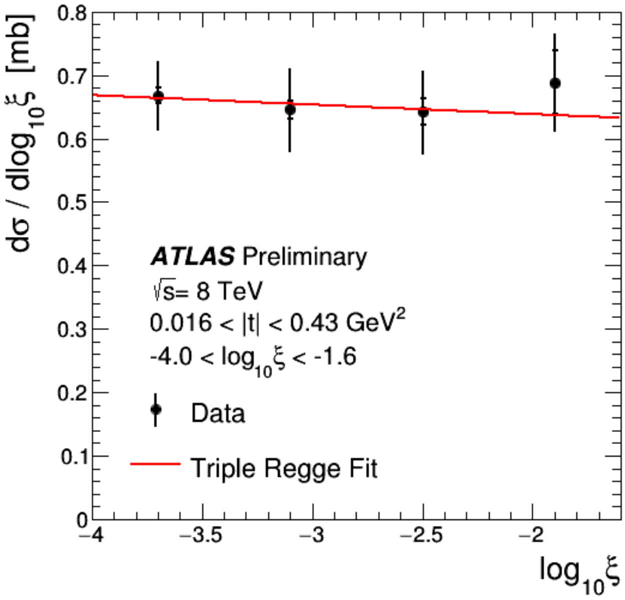

Figure 2.5: The differential cross section as a function of $\log_{10}\xi$. Data points are compared with the Regge theory predictions. From [9].

Central diffraction

Central diffraction is a class of processes in which system Z with quantum numbers of vacuum is produced in the central region. As both incoming particles emit a Pomeron, this process is also called *double Pomeron exchange*. The simplest case has the following structure:

$$a + b \rightarrow a + Z + b \,, \tag{2.6}$$

where both incoming particles remain intact. Also here, they are scattered at very small angles.

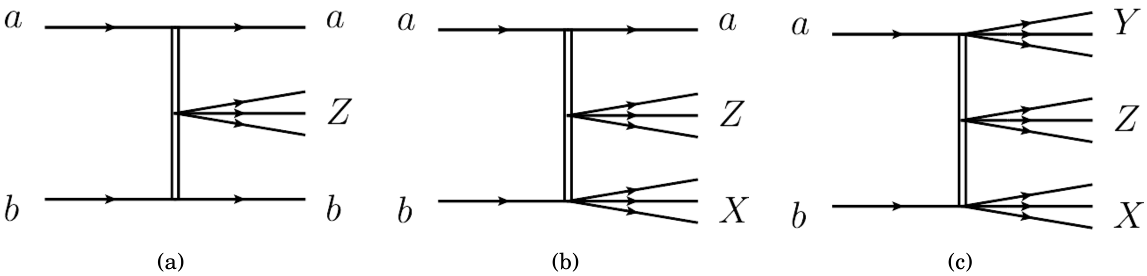

(a) (b) (c)

Figure 2.6: Feynman diagrams of central diffractive processes with: (a) both particles staying intact, (b) one particle staying intact and the other one dissociated, (c) both particles dissociated. The double line represents the Pomeron exchange. From [6].

However, one or both of them may dissociate as well like in the case of single and double diffraction. The processes of central diffraction are illustrated in Fig. 2.6.

Non-diffractive and minimum bias processes

Apart diffractive events, there is also a group of processes called as *non-diffractive interactions*. An example of such a process is presented in Fig. 2.7. In principle, the signature of non-diffractive processes is different from that of diffractive ones as an effect of the color exchange between colliding particles, i.e. there should be neither a large rapidity gap nor a remaining initial particle. However, a lack of a large rapidity gap in an event can be ambigouos. In diffractive events the size of the rapidity gap depends on the event kinematics – the bigger the initital particle energy loss, the smaller the size of a gap. For that reason, a gap can remain undetected when an initital particle looses a large part of its energy. From the other point of view, large rapidity gaps can occur in non-diffractive events as statistical fluctuations of the distance between nearby particles. In addition, because of the baryon number conservation, one naturally expects neutrons or protons in the final state of proton–proton non-diffractive processes. However, the average energy of such protons is much smaller than that of diffractively scattered protons [6]. What is more, a lack of detection of intact particle does not determine the nature of the process. First of all, it is possible that the incoming particles in a diffractive interaction dissociated. Another aspect is that the dedicated forward detectors have limited acceptance and thus may not register the intact particle.

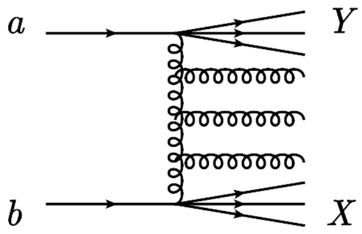

Figure 2.7: Feynman diagram of non-diffractive process. In this reaction three jets are produced (spring lines). From [6].

All the above mentioned reasons cause that non-diffractive interactions are the irreducible background for diffractive events. A term of *minimum bias processes* is taken as to refer to both non-diffractive and diffractive processes, except for the elastic scattering. Minimum bias measurements involve the event selection which is as unrestrictive as possible and cover measurements of charged particle spectra. They were performed at lower-energy e^+e^-, ep and hadron collisions for various centre-of-mass energies [10–13]. They provide insight into the strong interaction in the low-scale, non-perturbative region of QCD which is typically described by QCD-inspired models implemented in Monte Carlo (MC) event generators with free parameters that can be constrained by such measurements. Typically, the charged particle multiplicity, transverse momentum and pseudorapidity distributions are measured.

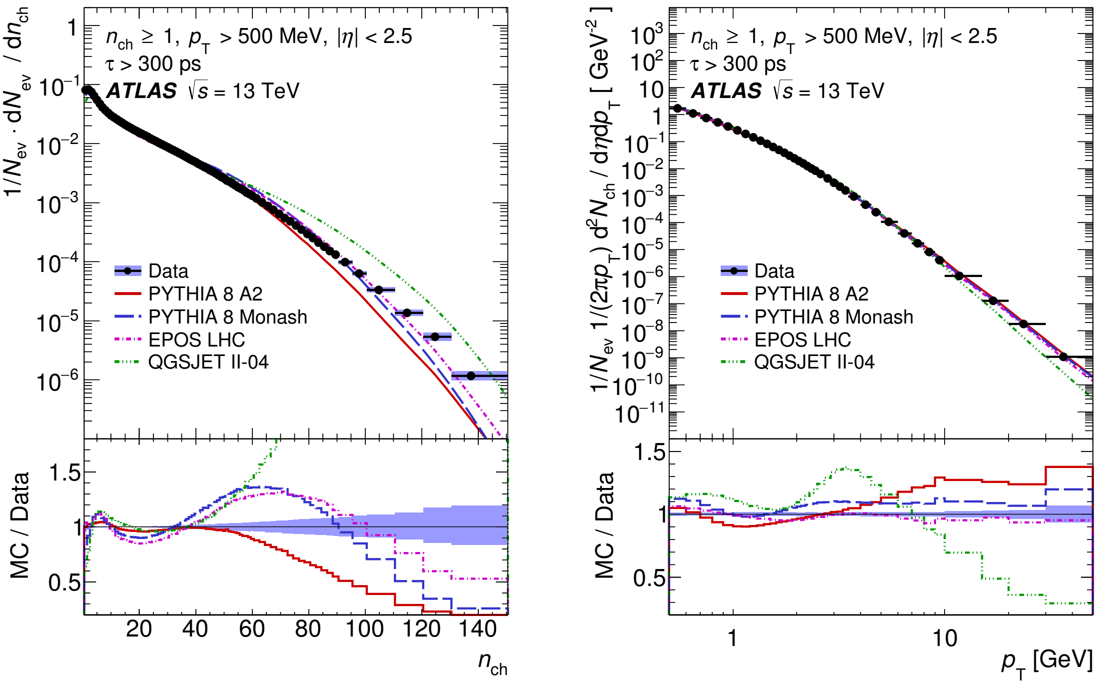

(a) (b)

Figure 2.8: Primary charged particle (a) multiplicity distribution, (b) multiplicities as a function of transverse momentum. From [14].

The example of such spectra measured by the ATLAS at the centre-of-mass energy of $\sqrt{s}$ = 13 TeV are presented in Figs. 2.8 and 2.9. One can see that MC generators describe the shape of the data multiplicity distribution quite properly only for multiplicities lower than 50. Also the transverse momentum ditribution is better described for lower values of p_T than for higher. Various MC models predict similar shape of the pseudorapidity distribution even though the values of the mean particle density are different. It can be concluded that the kinematics of the most common, minimum bias processes is still not sufficiently well understood. The measurement described in this dissertation is analogous to the one presented above, with the additional tag on a forward proton. It should indicate how well the kinematics of the diffractive processes is known. Potential discrepancies between the data and MC distributions can be used to the further tuning of MC models.

Gribov-Regge theory

The Gribov-Regge theory [15, 16] delivers phenomenological models which describe the soft diffractive interactions. It was suggested before the parton model and before quarks have been proposed. Regge phenomenology assumes that all resonances that can mediate the scattering contribute to the hadron–hadron interactions. These resonances can be assembled into families containing particles that differ from each other only by spin and mass. It turns out that

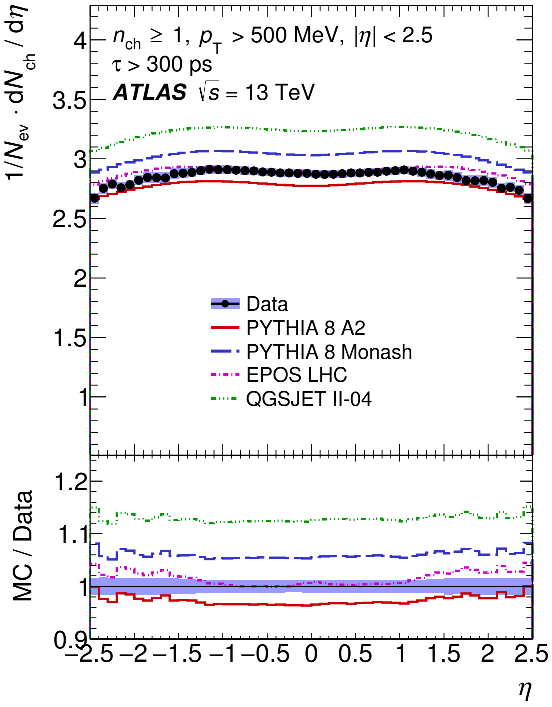

Figure 2.9: Primary charged particle multiplicities as a function of pseudorapidity. From [14].

in a squared mass - spin plane (the so-called Chew plane) particles from one family can be parametrised by a straight line (see Fig. 2.10), given as:

$$\alpha(t) = \alpha(0) + \alpha' t. \tag{2.7}$$

This line is called a *Regge trajectory*. For hadrons the trajectory has a separate name – *Reggeon*. All known resonances lie on Reggeons with the intercepts $\alpha(0) < 1$.

The total cross section for a hadron–hadron interaction can be approximated by [18]:

$$\sigma_{\mathrm{tot}} \approx \sum_i A_i s^{\alpha_i(0)-1}, \tag{2.8}$$

where the sum is over all contributing Regge trajectories and A_i are the corresponding coefficients. If interactions were mediated only by Reggeons, the total cross section should decrease with growing s. However, the experimental data show a rise of the total cross section in the region of high centre-of-mass energy (see Fig. 2.11), irrespectively of the type of interacting particles.

Regge phenomenology based only on Reggeons is not able to reproduce this rise. In order to describe this phenomena, a trajectory corresponding to a particle with the vacuum quantum numbers was introduced [20]. This trajectory is called a Pomeron and is parametrised with $\alpha(0) = 1.0808$ [21, 22]. It is presented in Fig. 2.12.

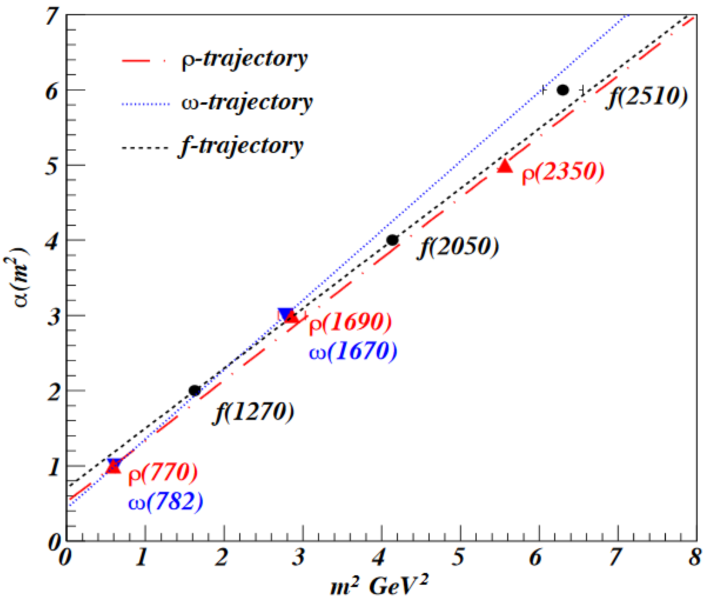

Figure 2.10: Regge trajectories for mesons ρ, ω and f parametrized by $\alpha(t) = \alpha(0) + \alpha' t$. For all of them $\alpha(0) < 1$. From [17].

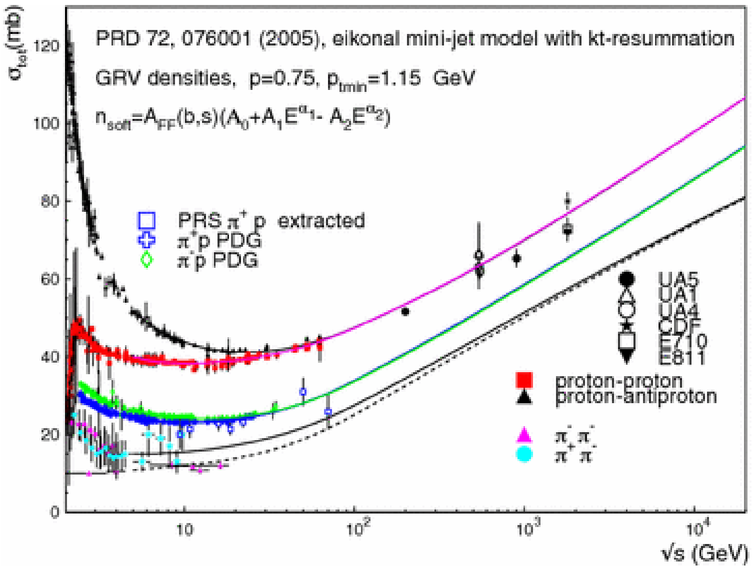

Figure 2.11: Proton and pion total cross sections as a function of the centre-of-mass energy $\sqrt{s}$. Cross sections grow with the increasing value of $\sqrt{s}$ until reaching the $\sqrt{s}$ above about 10 GeV. From [19].

2.2.2 Hard Diffraction

There are two distinct regimes in which the diffraction manifests itself. First of them is the described above soft diffraction that takes place at low momentum transfers. At high momentum transfers the so-called hard diffraction is observed.

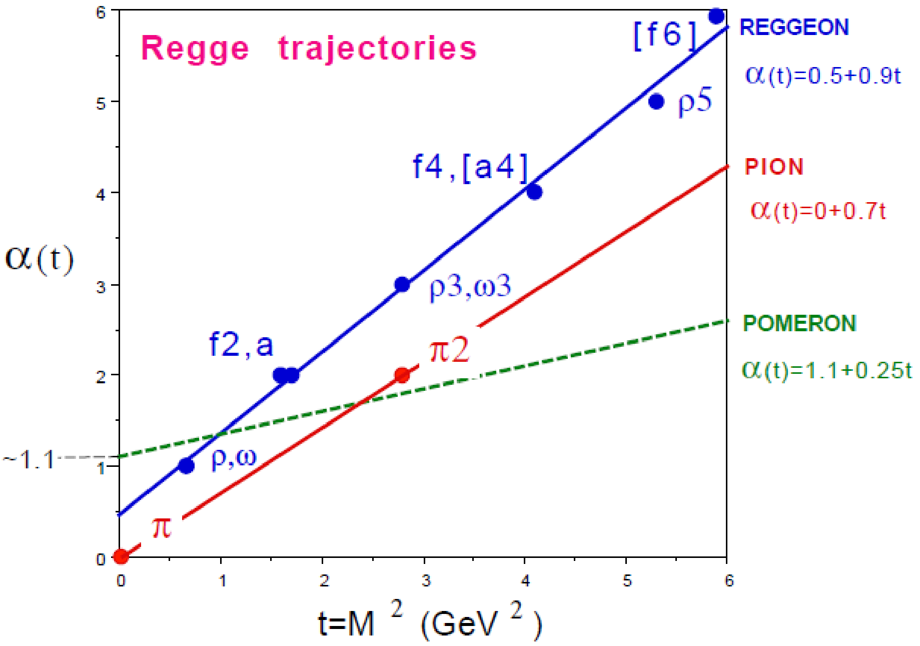

Figure 2.12: Regge trajectories for mesons (reggeon), pions and Pomeron. From [5].

The first evidence for the existence of a hard component in diffractive scattering was reported by the UA8 Collaboration [23, 24] in 1988 at the S$\bar{p}$pS collider in a study of dijet events produced in association with a leading proton . Later hard diffraction was intensively studied at HERA and also in $p\overline{p}$ collisions at the Tevatron.

The diffractive signature of a rapidity gap or a forward intact proton can be found also in hard diffractive processes. As in soft diffraction, this process is believed to be mediated by a Pomeron exchange [8]. Similar to the case of soft diffraction, several types of hard diffractive interactions can be considered.

Feynman diagrams for two types of hard diffractive interactions, single-diffractive and central-diffractive, are presented in Fig. 2.13. In these, one (or two) initial particle emits a Pomeron. The exchanged Pomeron reveals its partonic structure and one of its partons interacts either with the other initial particle (a hard single-diffractive process, see Fig. 2.13(a)) or with a parton from the other Pomeron (a hard central-diffractive process, see Fig. 2.13(b)) [6]. The interaction parton carries only a part of Pomeron energy, so one can talk about the Pomeron remnant, analogous to proton remnants appearing in non-diffractive processes. The whole process can be treated as a non-diffractive interaction between an initial particle and a Pomeron (Pomeron and Pomeron).

Hard diffraction is described using the perturbative QCD. The Pomeron is interpreted there as a colorless compound object with the quantum numbers of the vacuum and with an internal, partonic structure, represented in the lowest order by a pair of gluons. The idea of characterization of the hard diffractive interactions using the parton distribution functions came from the hard

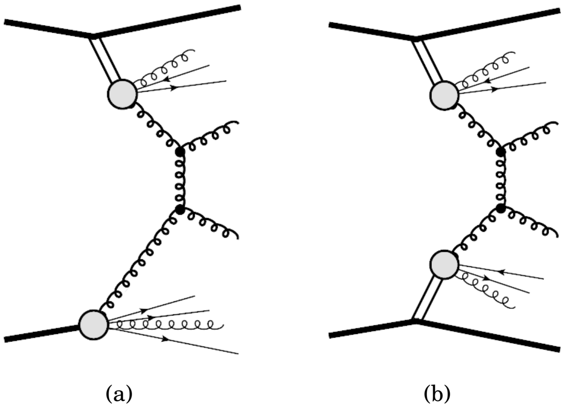
(a) (b)

Figure 2.13: Feynman diagrams of hard diffraction processes: (a) single-diffractive, (b) central-diffractive, The double line represents the Pomeron exchange. The blobs denote the partonic structure of the Pomeron and that of the incoming hadron. In both interactions a pair of jets is produced. From [6].

non-diffractive interactions [25–27]. The distribution of partons within a proton is known from many experiments, mainly HERA, Tevatron and LHC. Experiments showed that the partonic structure of a Pomeron is dominated by gluons [5].

2.3 Monte Carlo

Monte Carlo generators are commonly used in high-energy physics as the event structure is complex and not predictable from first principles. Event generators allow dealing with the simulation by subdividing it into smaller parts. Some of these can be described using first principles while the others need to be based on appropriate models with parameters tuned to data [28]. Inevitably, MC generators allow simulation of interactions of particles with matter, including full detector simulations.

The components of the MC generators dealing with hard physics are based upon perturbative QCD. The soft hadronic phenomena, including hadronization and the formation of the underlying event rely upon QCD-inspired models [29].

In this analysis two MC generators are used:

1. PYTHIA 8.2 [30]

   In PYTHIA 8.2 the total, elastic and inelastic cross sections are obtained from Regge fits to data (the used Donnachie-Landshoff parametrisation is described in [21]). Diffractive interactions are treated as non-diffractive hadronic collisions between a proton and a Pomeron [30]. A separate description for low and high masses of the diffractive system is applied. For $M_\text{X} < 10$ GeV the diffractive system is assumed to exhibit no perturbative effects and thus treated as non-perturbative hadronizing string with the quantum numbers of the original hadron [31]. For higher masses a perturbative description is implemented, with the initital and final state radiation effects included and the multiple parton interactions allowed, resulting in underlying events.

The inelastic cross section is split into diffractive and non-diffractive parts, with following contributions:

- single-diffractive processes with σ_{SD} = 12.83 mb,
- double-diffractive processes with σ_{DD} = 8.798 mb,
- non-diffractive processes with σ_{ND} = 56.79 mb.

The used inelastic (signal) sample is constructed from the samples of three above mentioned processes, weighted according to their cross sections.

In this analysis the A2-MSTW2008LO tune [32] is used – this is a tune dedicated to minimum bias analysis in which central-diffractive processes are not considered. Anyhow, their contribution to the total cross section is negligible. This tune uses parton distribution functions called "MSTW 2008 LO" [33], determined from hard-scattering data, based on the CDF data and tuned to early LHC data [34].

2. EPOS [35]

   EPOS stands for *Energy conserving quantum mechanical approach, based on Partons, parton ladders, strings, Off-shell remnants, and Splitting of parton ladders*. As opposed to PYTHIA 8.2, the calculations are not based on the parton distribution functions, but exploit the parton-based Gribov-Regge theory, describing soft and hard interactions simultaneously – each of the many binary pp interactions creates a parton ladder. The LHC tune [36] is used in the present analysis.

   In contrary to PYTHIA 8.2, EPOS does not allow selection of the generated process.

Event samples were processed by the Geant4-based [37] ATLAS simulation framework [38]. The simulation uses a detailed description of the ATLAS detector.

CHAPTER 3

EXPERIMENTAL APPARATUS

Diffractive processes sketched in the previous chapter can be investigated experimentally. In this dissertation the data collected by the ATLAS Experiment at the LHC have been used. Their experimental apparatus is described below.

3.1 The Large Hadron Collider

The Large Hadron Collider (LHC) [39], which started its operation in 2008, is the main and the largest accelerator of the European Organization for Nuclear Research (CERN). It is located in the former Large Electron–Positron (LEP) [40] tunnel of nearly 27 km circumference. The accelerator is placed about 100 m below the ground level.

The accelerator may store and accelerate beams of protons or ions and may deliver proton-proton, proton-ion and ion-ion interactions. Its beams are stored in two separate beam pipes. The clockwise-circulating beam (viewed from above the LHC ring) is called *beam1* and the anti-clockwise-circulating one – *beam2*. About 140 m away from the interaction point the two beam pipes merge into a single one and the beams are brought to a collision. The beams collide in four interaction points (IP) named: IP1, IP2, IP5 and IP8 (see Fig. 3.1).

To keep the beams on the orbit, 1232 dipole superconducting magnets providing magnetic field of 8.3 T are used. Additionally, 392 quadrupole superconducting magnets are installed to precisely control the optics of the beams. To accelerate the beams, superconducting RF cavities are used. Their basic frequency is 400 MHz. The LHC beams are created in few stages. Those related to the proton beam creation are the following. At first, hydrogen atoms are stripped of the electrons and passed to the linear accelerator, Liniac 2, where they are accelerated to the energy of 50 MeV and then transferred to the Proton Synchrotron Booster (PSB). The PSB accelerates

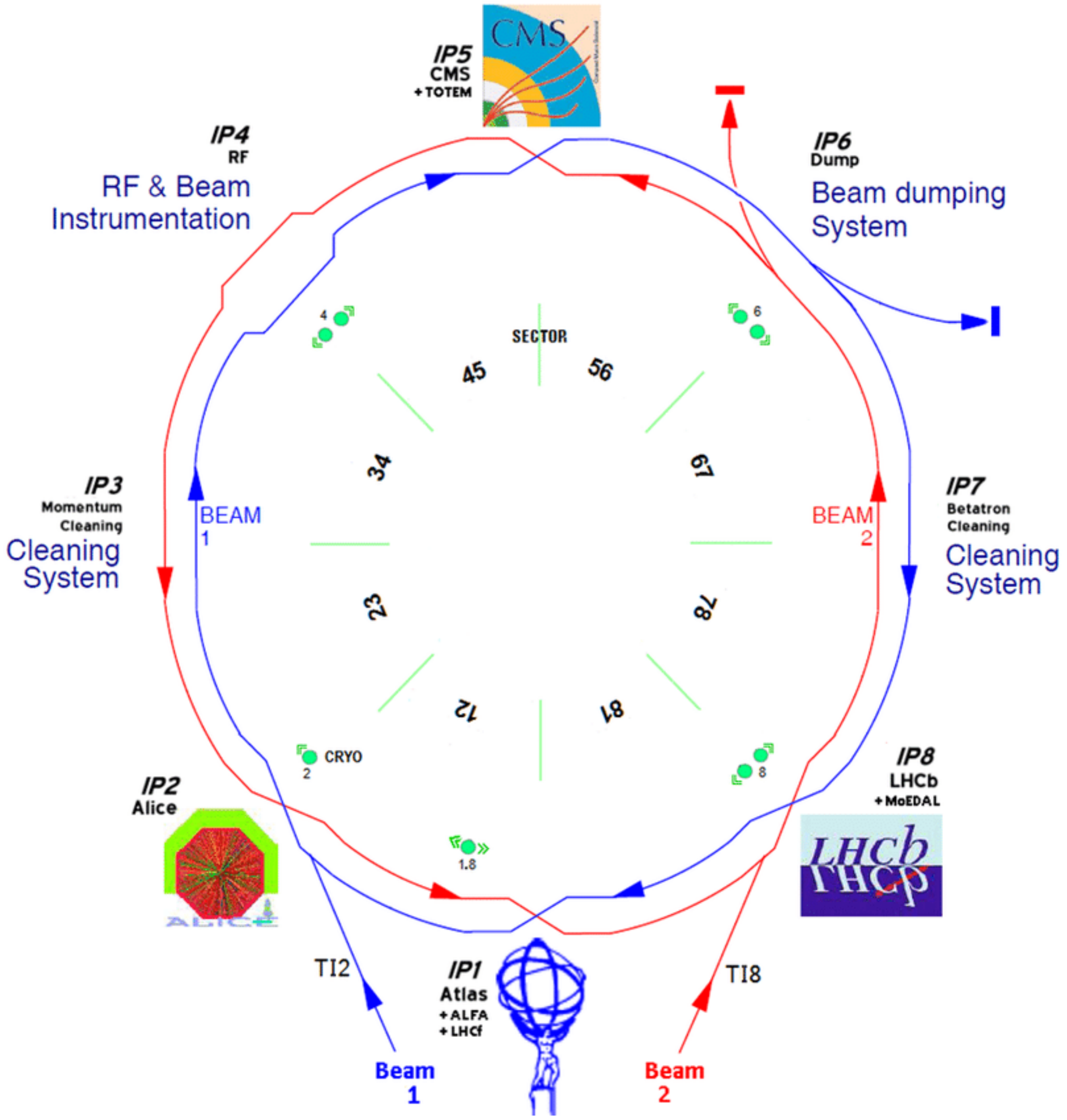

Figure 3.1: Sketch of the LHC with the eight interaction points labelled IP1 to IP8. At IP1 the ATLAS and LHCf experiments are installed, at IP2 the ALICE experiment, at IP5 the CMS and TOTEM experiments and at IP8 the LHCb and MoEDAL experiments. From [41].

the protons to 1.4 GeV energy and the particles are injected into the Proton Synchrotoron (PS) where they reach energy of 25 GeV and the bunch structure is formed. Next, the bunches are transferred to the Super Proton Synchrotron (SPS) where they are accelerated to 450 GeV and eventually injected into the LHC. The LHC accelerates both beams to the final energy in about 20 minutes.

The LHC accelerates proton and ion beams to previously inaccessible energies. The design energy of the proton beams is 7 TeV, resulting the centre-of-mass system energy of $\sqrt{s} = 14$ TeV. Such energy will be reached after the accelerator modifications introduced during the Long

Shutdown 2 (2019-2021). Up till now, the maximum value of the centre-of-mass energy was $\sqrt{s} = 13$ TeV. In case of lead nuclei, the nominal energy amounts to 5.52 TeV per nucleon.

The collisions at the LHC are studied by seven experiments, including four main ones: ATLAS, CMS, ALICE and LHCb and the three smaller ones: TOTEM, LHCf and MoEDAL. Each of these experiments has it own set of detectors and the physics programme.

The ATLAS (*A Toroidal LHC Apparatus*) [42] and the CMS (Compact Muon Solenoid) [43] are general-purpose detectors. However, they differ in the sense of the design and the applied technologies. Both detectors cover large solid angles in order to maximise their acceptance. Additionally, forward detectors aiming at the registration of protons scattered in the forward directions (into the detector openings containing the beam pipe) are installed along the beam pipe.

The ALICE (*A Large Ion Collider Experiment*) [44] experiment is optimised to study heavy ions collisions. In such interactions, where the matter interacts strongly at extreme energy densities, the quark-gluon plasma may be created. The detectors deliver information on the produced particles which serves as a basis for the studies of the properties of hot, dense matter.

The LHCb (*LHC beauty*) [45] experiment aims at the investigation of the CP-symmetry violation in the B-meson sector and at the studies of rare exotic processes. Such studies, inter alia, can help to explain the matter-antimatter asymmetry of the Universe and can shed a light on BSM physics.

The small experiments share interaction points with the main ones. The TOTEM (*TOTal Elastic and diffractive cross section Measurement*) [46] detectors are located in vicinity of the CMS experiment. They provide a coverage of the very forward rapidity region and they can register diffractively scattered protons.

The LHCf (*LHC forward*) [47] is located 140 m from the ATLAS interaction point, on both its sides. It is dedicated to the detection of neutral particles produced in the forward region.

The MoEDAL (*Monopole and Exotics Detector At the LHC*) experiment [48] is located close to the LHCb experiment and searches for exotic particles such as magnetic monopoles, dyons or other highly ionizing particles.

3.1.1 The proton beam structure and the LHC optics

The LHC beam has a certain time structure. The machine basic frequency is 400 MHz and it introduces the so-called beam RF-buckets. In total there are 35640 buckets of 2.5 ns length per beam. Nominally, only every tenth can be filled with particles and is called a bunch. Thus, the bunches are separated by 25 ns, which can be translated into a distance of 7.5 m between consecutive bunches. They pass the interaction point with 40 MHz frequency. Taking into account the breaks needed for the machine filling and the beam dumps, at maximum only 2808 bunches can be used for collisions. Each of possible crossings is labeled by an integer named the Bunch Crossing ID (BCID). However, the LHC can work with various beam configuration starting with a single bunch per beam. The nominal length of a bunch is 75 mm. Its nominal transverse widths are about 16 μm in the horizontal and vertical directions. Number of protons in a given bunch can be tailored during the beam shaping process and it can reach even 10^{11}.

The beams do not collide head-on but at an angle of a couple of hundred microradians to avoid parasitic collisions of bunches leaving the interaction region with those coming into it and belonging to the other beam. Therefore, the **crossing angle** has to be large enough to provide a separation that reduces also long-range interactions between the beams to an acceptable level [49]. Fig. 3.2 presents structure of the beams and the crossing angle between beams.

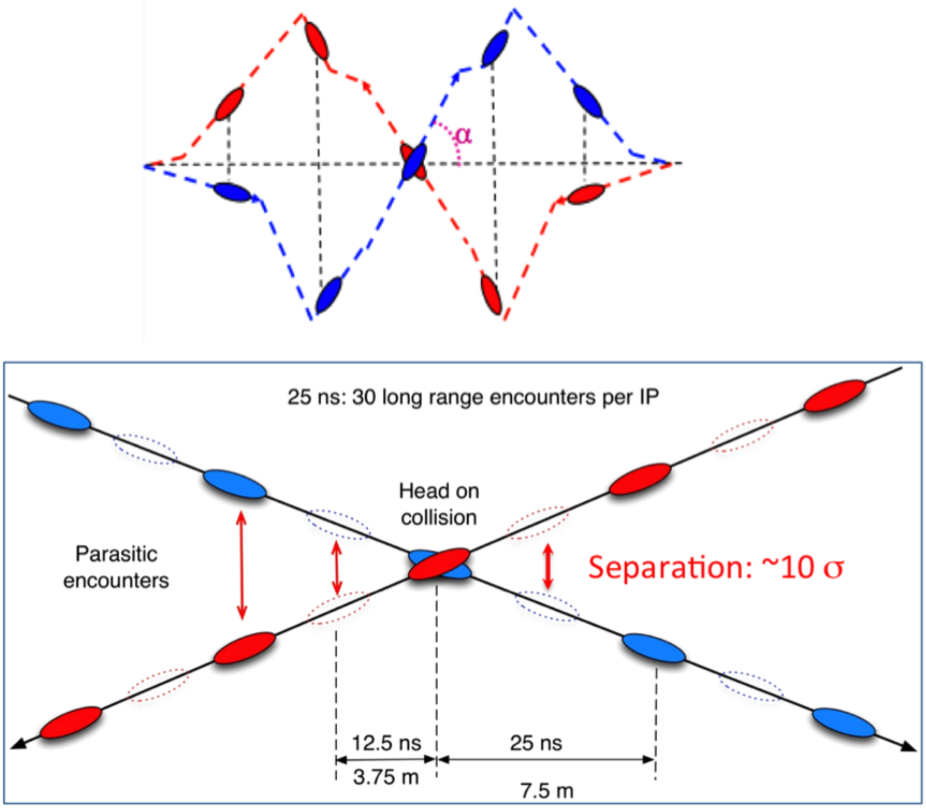

Figure 3.2: Sketch of the beams consisting of bunches, colliding at a crossing angle, which is marked by α on the top drawing. The vertical scale is not preserved. From [49].

The LHC machine settings, including settings of the magnets, are commonly reffered to as the “LHC optics” or the “beam optics”. They determine the trajectories of the beam particles. In fact, the crossing angle is one of the beam optics parameters. Below some other are described.

An important function describing the beam is the **betatron function** $\beta(s)$. This function is a function of the position s[1] along the beam trajectory. It measures the distance at which the transverse beam dimension is doubled. The value of the betatron function at the interaction point is customarily denoted by β^*. The lower is the value of β^*, the smaller is the beam size [50]. The

---

[1] One should notice that symbol s does not indicate on the Mandelstam variable in this context.

standard LHC setting, optimised to maximise the number of proton–proton interactions, is the so-called *collision optics*. Its designed value is $\beta^* = 0.55$ m. Presently, for the collision optics it is $\beta^* = 0.4$ m.

Another important beam parameter is its **emittance** ε. It is a measure of the average spread of the beam in a position–momentum phase space. Its nominal value is $\varepsilon = 3.75$ μm·rad.

The transverse beam widths along the orbit at a given point s are related to the $\beta(s)$-value by:

$$\sigma_{x,y}(s) = \sqrt{\frac{\beta_{x,y}(s)\cdot\varepsilon}{\gamma}} \tag{3.1}$$

and the beam angular divergences are given as:

$$\sigma_{\theta_{x,y}}(s) = \sqrt{\frac{\varepsilon}{\beta_{x,y}(s)\cdot\gamma}}\,, \tag{3.2}$$

where $\gamma = E/m$ is the beam Lorentz factor.

The rate of a given process, dN_{process}/dt, is proportional to its cross-section, $\sigma_{\mathrm{process}}$, and the proportionality coefficient is called the **instantaneous luminosity**, L:

$$\frac{dN_{\mathrm{process}}}{dt} = L\cdot\sigma_{\mathrm{process}}\,. \tag{3.3}$$

The LHC nominal instantaneous luminosity is $2\cdot 10^{34}$ cm^{-2}s^{-1}. This value can also be calculated using the beam properties:

$$L = \frac{n_b\cdot N_1\cdot N_2\cdot f_{\mathrm{rev}}\cdot\mathscr{F}}{4\pi\cdot\sigma_x^*\cdot\sigma_y^*}\,, \tag{3.4}$$

where n_b is the number of colliding bunches per beam, N_1 and N_2 are the numbers of particles per bunch in *beam1* and *beam2*, respectively, f_{rev} is the beam revolution frequency, $f_{\mathrm{rev}} = 11245.5$ Hz – it is the frequency of one bunch of protons to revolve the LHC ring, $\mathscr{F}$ is the geometric luminosity reduction factor due to the crossing angle at the interaction point which is equal to one in case of head-on collisions and is given by:

$$\mathscr{F} = \left(1 + \left(\frac{\theta_c\cdot\sigma_z^*}{2\sigma^*}\right)^2\right)^{-1/2}\,, \tag{3.5}$$

where θ_c is the crossing angle at the IP, σ_z^* is the bunch length at the IP and σ^* denotes the transverse beam size at the IP. Parameters σ_x^* and σ_y^* in (3.4) are measured using van der Meer scans (beam-separation scans) [51]. The principle of these scans is to measure simultaneously the collision rate at zero beam separation and the corresponding beam currents. The observed event rate is recorded while scanning the two beams across each other separately in the horizontal and vertical direction. This measurement yields two bell shaped curves, with the maximum rate at zero separation, from which one extracts the values of σ_x^* and σ_y^*. One should note that for the data considered in this dissertation $\sigma_x^* = \sigma_y^* = \sigma^*$, i.e the beam envelope at the IP is circular.

Using (3.5) and (3.1), Eq. (3.4) can be rewritten as:

$$L = \frac{n_b \cdot N_1 \cdot N_2 \cdot f_{\text{rev}} \cdot \gamma \cdot \mathscr{F}}{4\pi \cdot \varepsilon \cdot \beta^*}, \tag{3.6}$$

showing a clear inverse-proportionality of the luminosity and the β^* value.

The luminosity value gives also the mean number of pp interactions, μ, occurring during a collision of two proton bunches. If one assumes that the luminosity is uniformly distributed over all bunches colliding with frequency f_{coll}, then μ can be calculated as:

$$\mu = \frac{\sigma_{\text{total}} \cdot L}{n_b \cdot f_{\text{rev}}}, \tag{3.7}$$

where σ_{total} is the total pp cross section.

The distribution of the number of pp interactions per bunch crossing is given by Poisson distribution with mean μ. The phenomenon of having multiple proton-proton interactions in a single bunch crossing is called *pile-up*. The pile-up multiplicity at the LHC can be quite large, reaching above 70.

3.2 The ATLAS Detector

The ATLAS experiment [42] is one of the four major experiments carried out at the LHC. It is a general-purpose experiment, designed to explore a wide range of physics phenomena. The ATLAS detector is one of the largest (46 m of length and 25 m in diameter), most expensive and most complex scientific instruments ever built.

The ATLAS detector consists of many concentric layers of various sub-detectors centered at the interaction point. Its central part is called the "barrel" while the more forward regions at both sides of the interaction point are named the "end-caps". The ATLAS sub-detectors allow the measurement of trajectories, momenta and energies of particles created in the interactions, and hence deliver information which can be used to identify the produced particles.

3.2.1 The ATLAS coordinate system

ATLAS uses a right-handed reference frame (see Fig. 3.3) which origin is located at the nominal interaction point (IP1), with the z axis along *beam2* and the x axis pointing towards the center of the LHC ring. Side of the ATLAS interaction point with negative values of z is called side C, whilst the other one is called side A.

The transverse plane is defined with respect to the beam. Cylindrical coordinates (r, φ) are used in the transverse plane, φ being the azimuthal angle measured around the beam-axis. The pseudorapidity, η, is defined in terms of the polar angle of a particle, θ (measured from the beam-axis), as:

$$\eta = -\ln \tan(\theta/2)\,. \tag{3.8}$$

The sign of pseudorapidity on each side of the interaction point is the same as the sign of z coordinate.

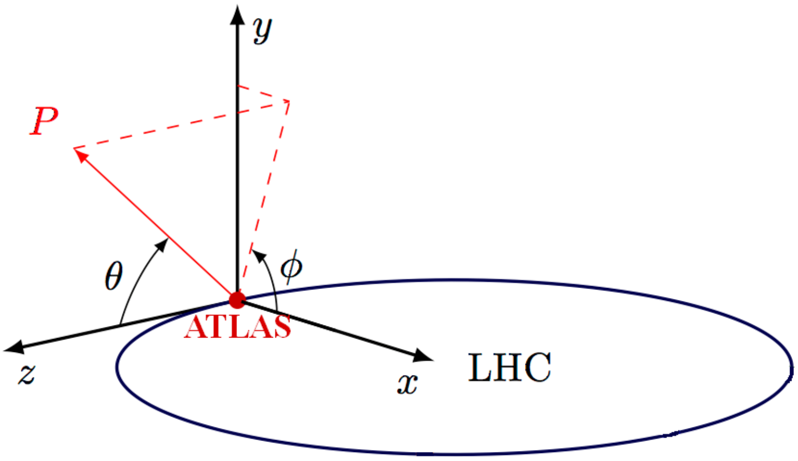

Figure 3.3: The ATLAS coordinate system. "P" is a given point, z axis is along *beam1*, the transverse plane is a $x-y$ plane. A θ angle is a polar angle whilst φ an azimuthal angle. Based on [52].

Protons trajectories are usually described in a curvilinear, right-handed coordinate system (x, y, s). The local s axis is tangent to the reference orbit at a given point of the beam trajectory. The axis origin is located at the IP.

3.2.2 The Inner Detector

The most central part of the ATLAS Detector is the Inner Detector (ID) [53, 54]. Its outer radius is 1.15 m and its length about 6 m. It provides the reconstruction of the charged particle tracks up to $|\eta| < 2.5$. The ID consists of three detection systems, each of them of high granularity and providing a high precision of the registration of trajectories of charged particles. In the barrel region (see Fig. 3.4) the detectors are organized in concentric cylinders around the beam-axis, while in the end-cap region (see Fig. 3.5) the detectors are mounted on disks perpendicular to the beam-axis. All ID subdetectors are immersed in the strong magnetic field of 2 T of the Central Solenoid. This field is parallel to the beam-axis. The magnetic field bends the trajectories of produced charged particles, so the measurement of their curvature allows one determine the particle momentum and charge.

First component of the Inner Detector, situated closest to the interaction point, is the **Pixel Detector** [56]. It consists of three pixel barrels placed at radii of 5, 9 and 12 cm and of three pixel end-cap discs on each side located at $|z| = 50$, 58 and 65 cm with $9 < r < 15$ cm. Typically, the Pixel Detector provides three measurements, the so-called *space-points*, of the track position with the highest spatial resolution of all of the ATLAS subdetectors. The resolution is 10 μm in $r \cdot \varphi$

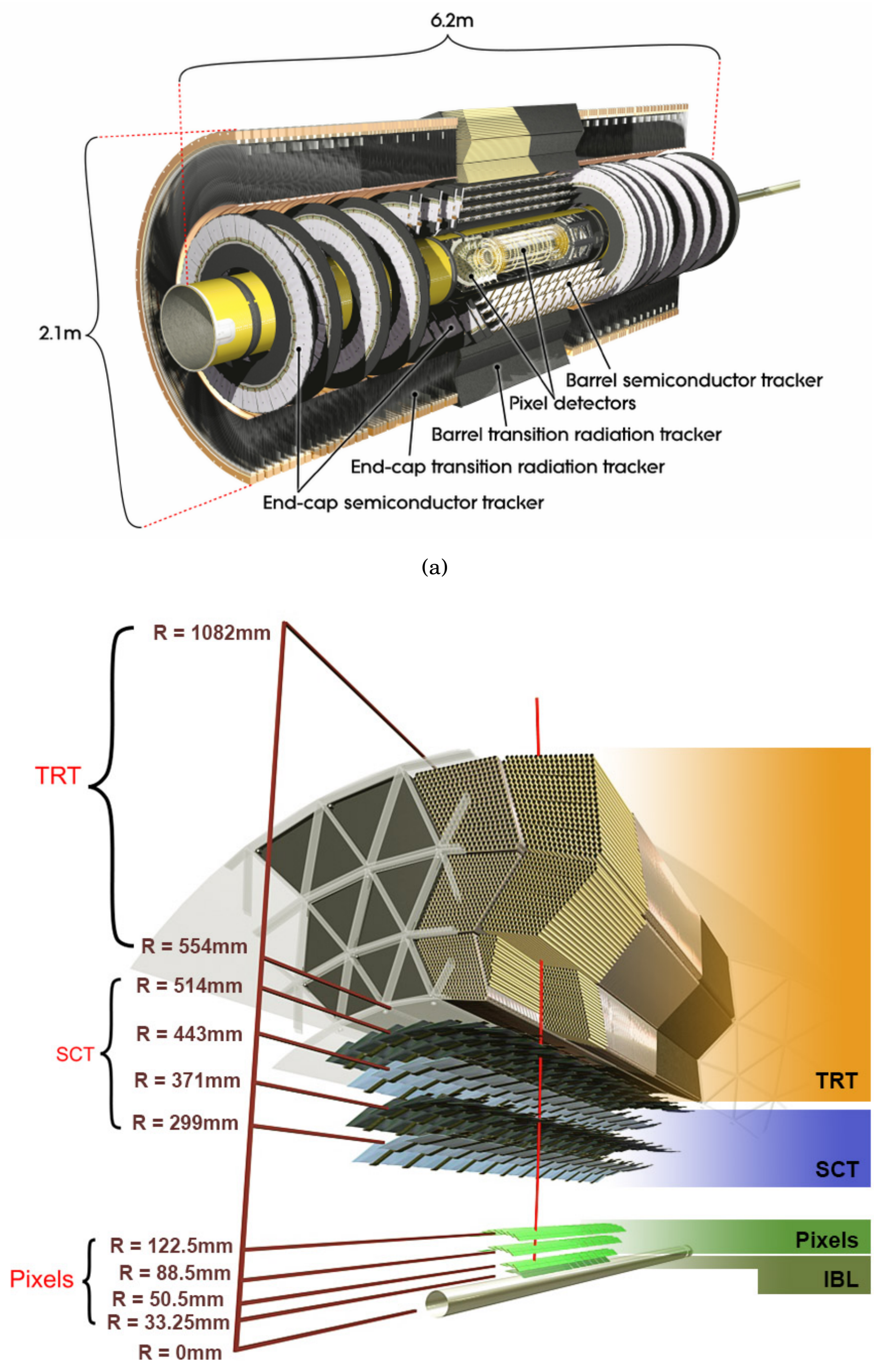

(a)

(b)

Figure 3.4: Central part of the ATLAS Detector, the Inner Detector with its subsystems: Pixel Detector, Semiconductor Tracker (SCT) and Transition Radiation Tracker (TRT). Bottom layout shows the barrel part. From [42].

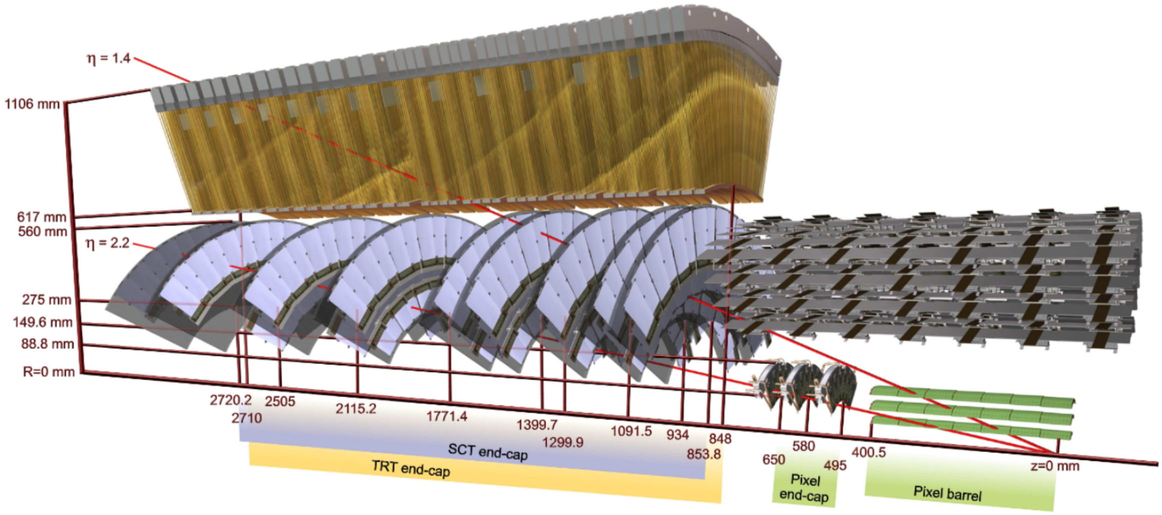

Figure 3.5: Layout of the end-cap part of the Inner Detector. From [55]

for both barrel and end-cap regions, 115 μm along z axis (barrel region) and 115 μm in r (end-cap region).

The second subsystem of the Inner Detector is the **Semiconductor Tracker** (SCT) [57], which surrounds the Pixel Detector. It is made of silicon mictrostrips layers, arranged in four barrels and two end-caps of nine discs each. In the barrel the layers are placed at $r = 30$, 37, 44 and 51 cm and $|z| < 75$ cm. The end-cap layers are symmetrically located at $|z| = 85$, 93, 109, 130, 140, 177, 212, 251 and 272 cm. The r range spanned by the SCT end-caps varies from layer to layer. The upper limit is 56 cm for each layer. The lower limit equals 34 cm for the first and seventh layer, 28 cm for layers from two to five, 41 cm for the eighth layer and 44 cm for the ninth one.

The SCT detector uses a sandwich module structure, i.e. each layer consists of a pair of sensores modules that are glued together back to back and rotated by a stereo angle of 40 μrad with respect to each other (see Fig. 3.6). Measurements from each pair are combined into a single *space-point*. Typically, the SCT provides four positions along the particle trajectory. The resolutions are: 17 μm in $r \cdot \varphi$ for both barrel and end-cap regions, 580 μm along z axis (barrel region) and 580 μm in r (end-cap region).

The outer part of the Inner Detector is the **Transition Radiation Tracker** (TRT) [58]. It is built with straw tubes of 4 mm in diameter. Each straw is filled with a non-inflammable gas mixture, containing 70% Xe, 27% CO_2 and 3% O_2. In the center of each straw an anode in a form of gold-plated thin wire is spanned. Coating of the inner straw wall is conductive and plays a role of a cathode. Charged particle, while passing through the straw, causes the gas ionization which leads to the creation of an electrical signal (see Fig. 3.7).

In the barrel there is about 50000 straws placed parallel to the beam-axis and covering

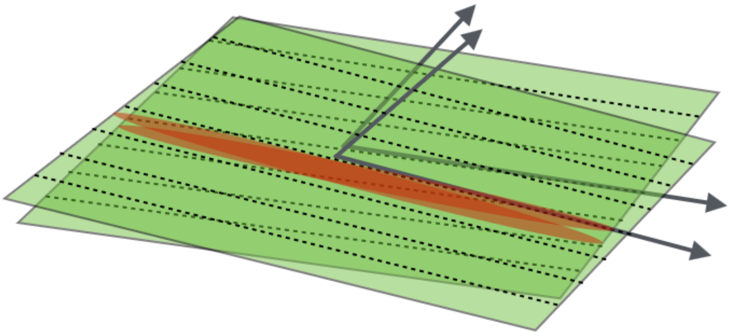

Figure 3.6: Layout of a silicon layer of the SCT, made of a pair of sensors rotated by the stereo angle of 40 μrad with respect to each other, improving precision of a strip system. Arrows represent the direction of drift of the electrons that were set free by the incoming particle. From [55].

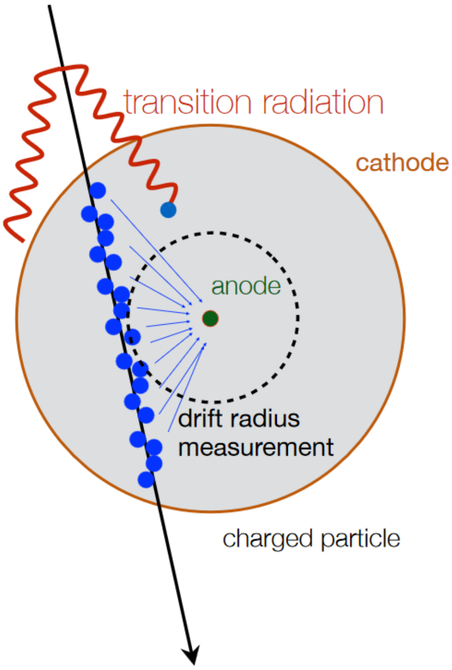

Figure 3.7: Scheme of a single TRT straw. Passing charged particle causes gas ionization inside a straw. Emerged electrons drift to the anode, leading to the creation of electrical signal. Transition radiation produced outside the straw leads to an additional energy deposit in the gas inside the straw. From [55].

a region of $56 < r < 109$ cm and $|z| < 72$ cm. In each end-cap region the straws are arranged in eighteen wheels positioned perpendicular to the beam-axis and covering $83 < |z| < 277$ cm and $62 < r < 111$ cm. The end-caps contain 250000 radial straws in total. The spaces between the straws are filled with polymer fibres (barrel) and foils (end-caps) in which the transition radiation (photons) [59] is created by passing charged particles. The emerged transition radiation is absorbed by Xe atoms, leading to additional energy deposits in the gas inside straws. They cause the enhancement of the electrical signal produced by the particle inside the straws. Strength of the transition radiation depends on the particle Lorentz factor and can be used for particle identification. The TRT spatial resolution is 120 μm in $r \cdot \varphi$ for both barrel and end-cap regions.

3.2.3 The Calorimeters

Calorimeters are detectors that provide the energy measurement of particles by absorbing them. In fact, the so-called particle showers are created by primary particles hitting a calorimeter. Showers consist of secondaries created in self-repeating interactions of particles with the calorimeter material. The composition, dimensions and development of created showers depend not only on the energy of the primary particles but also on their type which allows to some extent the primary particle identification. Due to the type of particles being measured, one can distinguish electromagnetic and hadron calorimeters. The former are designed to measure the energy of electrons, positrons and photons while the latter – the energy of hadrons.

The ATLAS detector uses sampling calorimeters. They consist of layers of “passive” high-density material, where the showers are created, interleaved with layers of an “active” medium allowing conversion of the energy deposited by particles into the electric signals. The calorimeters are located around the Inner Detector and the solenoid magnet. In contrast to the Inner Detector they are able to detect neutral particles.

The ATLAS calorimetry system, consisting of both electromagnetic and hadron calorimeters, is presented in Fig. 3.8. There are two calorimeter subsets, made of different active material: the Liquid Argon (LAr) Calorimeter and the scintillator Tile Calorimeter (TileCal). They provide coverage up to $|\eta| < 4.9$.

The **LAr Calorimeter** [60] consists of four calorimeters:

1. LAr electromagnetic barrel ($|\eta| < 1.475$, the passive material is lead, the energy resolution $\Delta E/E = 10\%/\sqrt{E(\text{GeV})} \oplus 0.7\%$),
2. LAr electromagnetic end-cap (EMEC) ($1.375 < |\eta| < 3.2$, the passive material is lead, the energy resolution $\Delta E/E = 10\%/\sqrt{E(\text{GeV})} \oplus 0.7\%$),
3. LAr hadronic end-cap (HEC) ($1.5 < |\eta| < 3.2$, the passive material is copper, the energy resolution $\Delta E/E = 50\%/\sqrt{E(\text{GeV})} \oplus 3\%$),
4. LAr Forward (FCal) ($3.2 < |\eta| < 4.9$, the passive materials are copper and tungsten, the energy resolution $\Delta E/E = 100\%/\sqrt{E(\text{GeV})} \oplus 10\%$).

Each LAr cell has a transversal dimensions of $\Delta\eta \times \Delta\varphi = 0.025 \times 0.1$.

The **Tile Calorimeter** [61] surrounds the LAr Calorimeter and consists of two hadronic calorimeters:

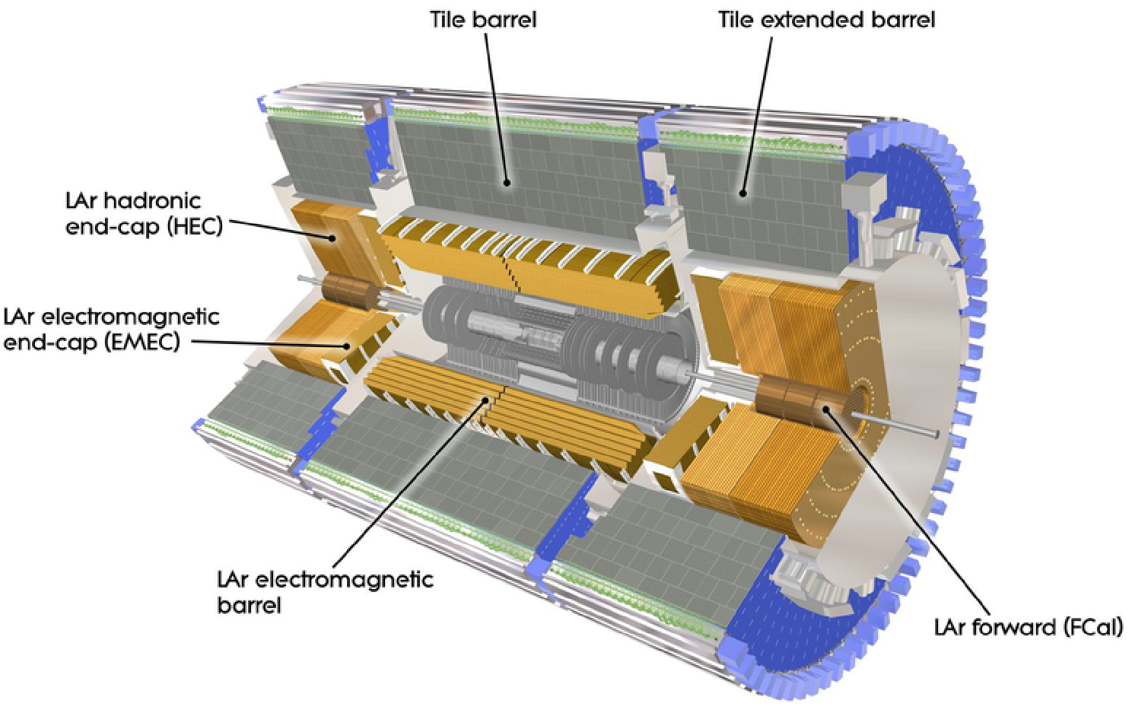

Figure 3.8: Layout of the ATLAS calorimetry system, consisting of the Liquid Argon Calorimeter and the Tile Calorimeter. From [42].

1. Tile Barrel ($|\eta| < 1.0$),
2. Tile extended barrel ($0.8 < |\eta| < 1.7$).

The basic detecting unit of the calorimeter is a cell. In total, the Tile Calorimeter has approximately 5000 cells. Each of them has the transversal dimensions of $\Delta\eta \times \Delta\varphi = 0.025 \times 0.1$.

The energy resolution shows a significant dependence on the pseudorapidity. The single hadron energy resolution obtained in beam tests is described by $\Delta E/E = 52\%/\sqrt{E(\mathrm{GeV})} \oplus 5.7\%$ for $\eta = 0.2$ while the jet energy resolution is $\Delta E/E = 50\%/\sqrt{E(\mathrm{GeV})} \oplus 3\%$.

In the Tile Calorimeter steel is used as the passive material and scintillating plastic tiles as the active medium. The particles excite atoms of scintilator tiles which eventually emit a fluorescent radiation. It is guided to the photomultiplier and on the output one gets an electric charge which amount is proportional to the energy deposited by the incident particle. The total number of read-out cells, including both end-caps of the calorimeter system, with pre-samplers, is almost 200000 [62].

3.2.4 The magnet system

The ATLAS magnet system consists of the already mentioned superconducting Central Solenoid surrounding the Inner Detector and three superconducting toroid magnets: one Barrel Toroid and two End-cap Toroids for the Muon Spectrometer (see Section 3.2.5) in order to bend the muon trajectory and provide the muon momentum measurement. In total, the magnet system is 22 m in diameter and 26 m in length. It is sketched in Fig. 3.9.

The Barrel Toroid consists of eight flat coils, each 25 metres long and 5 metres wide, grouped in a torus shape. It produces a toroidal magnetic field of approximately 4 T. The End-cap Toroids are also constructed from eight coils each and produce magnetic field of the same strength.

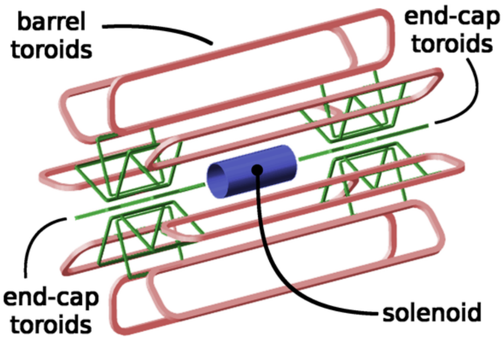

Figure 3.9: Scheme of the ATLAS magnet system. Central Solenoid is surrounded by the Barrel Toroid and End-cap Toroids. From [63].

3.2.5 The Muon Spectrometer

Muons, due to their relatively high mass, lose very little energy on their passage through the ATLAS Detector material. The Muon Spectrometer [64] is designed to identify muons and measure their momenta by registering muons trajectories in the magnetic field. It consists of four subsystems: the Monitored Drift Tubes (MDT), the Cathode Strip Chambers (CSC), the Resistive Plate Chambers (RPC) and the Thin Gap Chambers (TGC), as presented in Fig. 3.10. As a whole, these subsystems cover the range of $|\eta| < 2.7$ and are able to register muons within the range 3 GeV $< p_\mathrm{T} <$ 1 TeV.

The precision tracking chambers in the barrel use the MDTs (mostly) and the CSCs (in the forward region $2 < |\eta| < 2.7$). The single hit resolution in the bending plane for the MDT and the CSC is about 80 μm and 60 μm, respectively [65]. The RPCs and the TGCs are used for triggering purposes.

The Muon Spectrometer provides the momentum measurement with a relative resolution better than 3% over a wide range of transverse momenta and up to 10% at $p_\mathrm{T} \approx 1$ TeV.

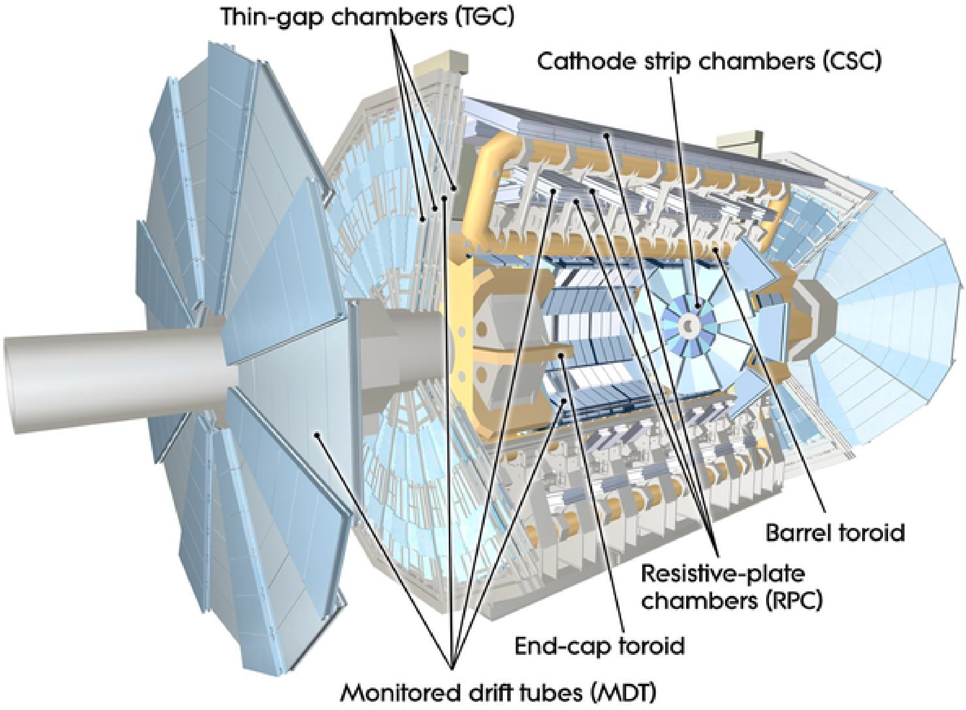

Figure 3.10: Layout of the ATLAS Muon Spectrometer. From [42].

3.2.6 The ATLAS Trigger and Data Acquisition system

The **Data Acquisition system** (DAQ) is used to read out data from detectors, to assemble full events from the fragments from different detector channels and to store them.

When the proton beams are already formed and LHC detectors start to take data, the machine settings and resulting conditions inside the beam pipe may still change. What is more, in some periods of time some of the detectors may malfunction. Therefore, short periods of time known as *luminosity blocks* (LB), lasting approximately one minute, are defined. The precise duration of a LB is set by the ATLAS DAQ. During an individual LB the data taking conditions are considered to be constant. All data-quality information, as well as the luminosity, are stored in a relational database for each LB. Once the data quality checks have been performed and the calibrations have been validated, a luminosity calculation algorithm is chosen as the “preferred” off-line algorithm for physics analysis and stored as such in the database. Corrections for the trigger prescales, DAQ deadtime and other sources of data loss are performed on an LB-by-LB basis when the integrated luminosity is calculated.

The DAQ system provides also tools for control and monitoring. The front-end electronics continuously preprocess and digitize analog data from the detectors.

Bunch crossings at the interaction point can take place at the nominal frequency of 40 MHz. A typical compressed event size is of the order of 1.6 MB what results in a huge amount of data delivered by the ATLAS detector. It is impossible to process data in such short time and store all of them. In practice, only about 200 events per second can be saved, thus it is crucial to decide which events should be kept and which rejected, since the interesting processes can be very rare and one can not afford to loose them. That verdict is settled by the trigger system.

The ATLAS **Trigger system** performs the selection process in two stages [66]. The Level-1 trigger (L1) is a hardware-based system. It works on a subset of information from the calorimeter, the muon and forward detectors. The decision is taken within 2.5 μs after the collision, based on a simplified reconstruction of muons, electrons, photons and jets and also on the hit information from the forward detectors. Finally, information from all the so-called Regions of Interest (RoIs), like the transverse momentum of particle or the large energy deposit, is combined resulting in a final decision. Out of nominal 40 million bunch crossings per second about 75000 are accepted by the L1 trigger.

The High Level Trigger (HLT) is software-based. It is run on a large array of custom processors that analyse further specific RoIs identified by the L1 system for each event, using information from all subdetectors. The decision time is about 4 s for each event. Events left after the HLT analysis are stored for future off-line analysis.

The Data Acquisition system together with the Trigger system form the TDAQ system. The data flow of the TDAQ system is presented in Fig. 3.11.

3.3 The forward detectors

Measurement capability of the ATLAS Detector is expanded by the forward detectors, dedicated to the special measurements in the forward directions. Their range of $|\eta|$ is larger than that of the Inner Detector. They are located up to about 240 m from IP1 and presented schematically in Fig. 3.12.

3.3.1 MBTS

One can aim not only at measurements of any particular physical process, but also measure inclusive particle distributions, with as much unbiased selection of interactions as possible – the minimum bias events. The Minimum Bias Trigger Scintillator (MBTS) [68] was designed for that purpose. It provides a trigger for charged particles produced in the interaction (the MBTS trigger requirements are described in Section 7.2.1).

MBTS consists of two polystyrene scintillator disks located symmetrically with respect to the IP1 at $|z| = 3.56$ m, on the LAr end-cap cryostats. Light emitted by the scintillators is collected by wavelength-shifting optical fibers and guided to photomultiplier tubes. Disks are segmented into two rings, each of them consisting of sixteen sectors. The outer ring spans $2.08 < |\eta| < 2.78$, while the inner one $2.78 < |\eta| < 3.75$.

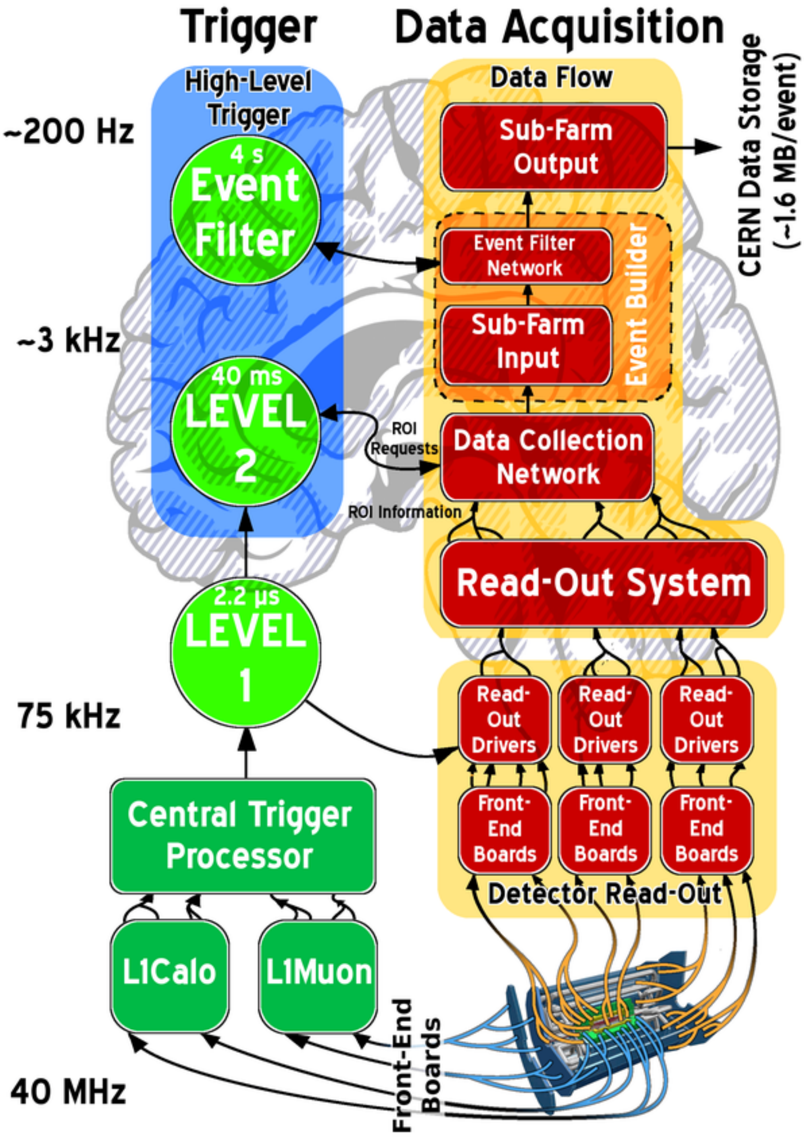

Figure 3.11: The data flow of the ATLAS TDAQ system. At present, the Event Filter and Level-2 trigger are not specified, being replaced by the High Level Trigger. From [63].

3.3.2 LUCID

The LUCID (*LUminosity measurement using Cerenkov Integrating Detector*) [69] is a Cherenkov light detector of passing charged particles. Its main purpose is both to measure the integrated luminosity and to provide the on-line monitoring of the instantaneous luminosity and the beam conditions (see details in Section 7.2.1). The two LUCID detectors are installed in the ATLAS end-cap regions, at a distance of approximately $z = \pm 17$ m from the interaction point, at a radial distance of approximately 10 cm from the beam line and cover $5.61 < |\eta| < 5.93$.

In 2015, the LUCID-1 detector was redesigned and replaced by a LUCID-2 [70]. At present,

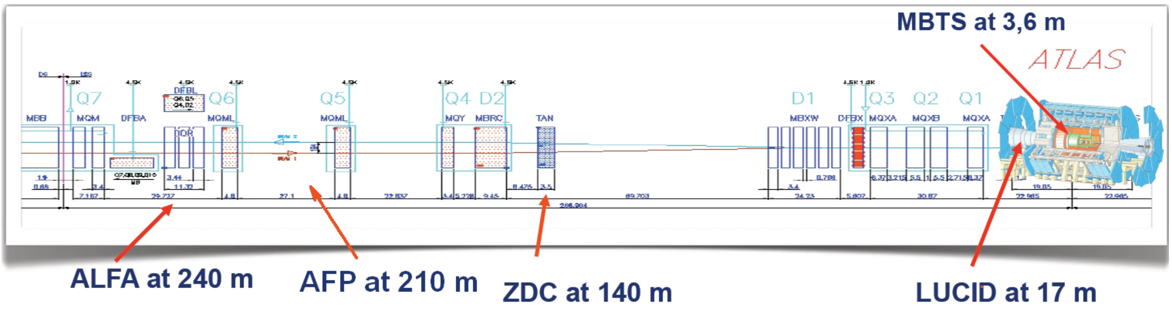

Figure 3.12: Layout of the forward detectors of the ATLAS experiment. For the sake of simplicity, only one side of the interaction point is shown. Based on [67].

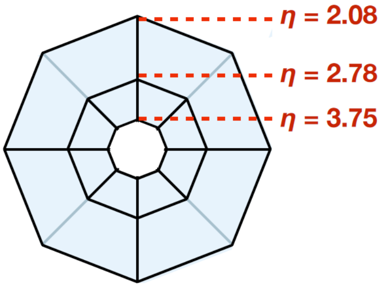

Figure 3.13: Layout of the MBTS detector. From [68].

each LUCID detector consists of twenty photomultipliers. The photomultipliers form in total five different sub-detectors on each side of the interaction point:

(a) the MODIFIED detector, consisting of 4 photomultipliers with reduced acceptance,

(b) the LED detector, consisting of 4 photomultipliers, calibrated with LED signals,

(c) the BI detector, consisting of 4 photomultipliers, calibrated with ^{207}Bi sources,

(d) the SPARE detector, identical to the LED detector but not turned on (kept in reserve),

(e) the FIBER detector, consisting of 4 quartz fiber bundles.

Photomultipliers are equipped with a 10 mm diameter quartz window acting as the Cherenkov medium. The photomultipliers belonging to different sub-detectors are shown in Fig. 3.14. The detectors are the threshold counters, triggered when the incident particle energy is at least 2.8 GeV for pions and 10 MeV for electrons.

3.3.3 ZDC

The ZDC (*Zero-Degree Calorimeter*) [71] was designed to detect neutral particles with $|\eta| > 8.3$, interacting electromagnetically or strongly. It plays also an important role in determining the

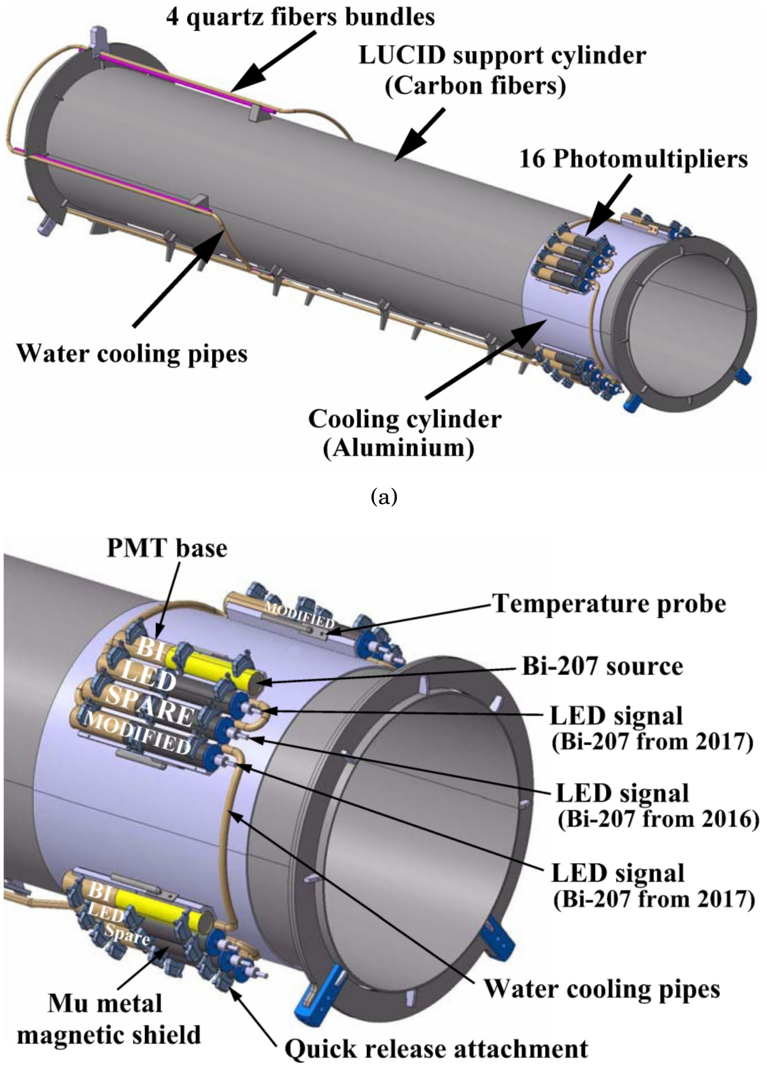

(a)

(b)

Figure 3.14: (a) The LUCID support cylinder with the four quartz bundles at the back and the 16 photomultipliers at the front. (b) The support and cooling structure of the photomultipliers. From [70].

centrality of heavy ion collisions by detecting spectator neutrons. It is located at both sides of IP1 at about $|z| = 140$ m, at the location where the straight section of the beam pipe bifurcates into two independent beam pipes, in the opening of the LHC Target Absorber Neutral (TAN) [39].

Each ZDC arm consists of four calorimeter modules, an electromagnetic followed by three hadronic ones. The modules are composed of tungsten with an embedded matrix of quartz rods. This detector was not running in the considered time range.

3.3.4 ALFA

The ALFA (*Absolute Luminosity For ATLAS*) [72] detectors aim at registering protons scattered at small angles, both elastically and diffractively. The elastically scattered ones can be used to determine the proton-proton total cross section, using the elastic cross section via the optical theorem. This, in turn, can lead to the absolute luminosity measurement and calibration of the relative luminosity detectors, e.g. LUCID.

The arrangement and geometry of the ALFA detectors were optimised to achieve acceptance for elastic events with $\xi = 0$ in dedicated beam optics conditions, with $\beta^* = 90, 1000$ or 2625 m. Protons scattered at very small angles, especially the elastically scattered ones, traverse the beam pipe separated very close to the circulating beams. Hence, the detectors dedicated to their measurement have to be placed far away from the interaction point and as close to the beam as possible. However, for some time after the beam injection into the LHC, the proton beams may be unstable. Such conditions do not allow maintaining detectors inside the beam pipe as they could get damaged. Thus, the technology allowing complete extraction of the detectors from the beam pipe was developed and is used – this is the Roman Pot technology. It allows also setting of the detector position independently for each run as well as the movement of the detectors inside the beam pipe during the run. The ALFA detectors consist of four station located at around $|z| = 237$ m and $|z| = 241$ m. Each station is equipped with two vertical Roman Pots.

A single ALFA detector consists of the *Main Detector* (MD) and two *Overlap Detectors* (ODs) (see Fig. 3.15). They are made of scintillating fibers with transverse dimensions of 0.5×0.5 mm^2.

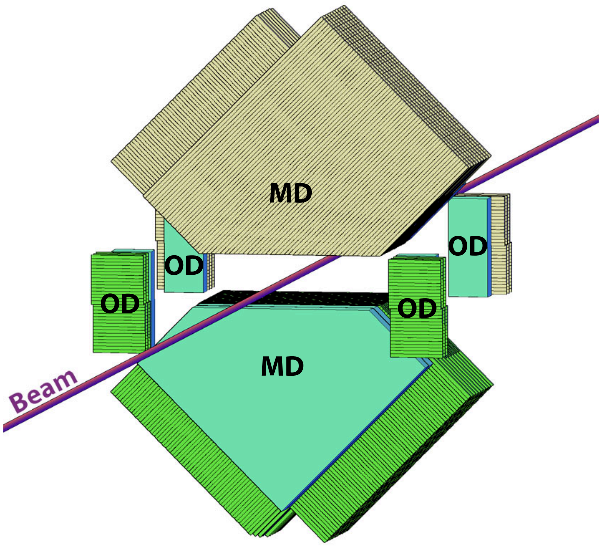

Figure 3.15: Layout of the ALFA station, consisting of two ALFA detectors. From [73].

In MD, the fibers are arranged in ten detection planes, each of them made of two layers of 64 parallel fibers. The fibers are oriented at the angle of 90° with respect to each other and at the angle of ±45° with respect to the y axis. Effectively, the active area of the detector has a shape of a pentagon, as presented in Fig. 3.16. The spatial resolution of the scattered proton trajectory measurement is 30 μm.

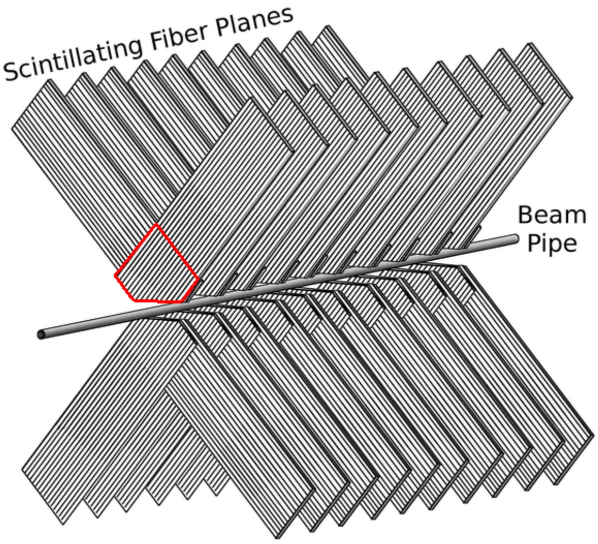

Figure 3.16: Layout of the ALFA detector scintillating planes. A red pentagon shows the shape of the active area of the detector. From [63].

The Overlap Detectors [72] are designed to the measurement of the vertical distance between the two MDs in the station. They are mounted on both sides of the MD, at a fixed and well known position with respect to them, and comprise three planes of 30 fibres. Their active area has the shape of two vertical stripes of 6×15 mm^2. During the ALFA detectors insertion into the beam bipes the ODs move with the MDs. The active areas of the ODs start to overlap when the two MDs are separated by about 17 mm. This distance can be determined from the measurement of particles which traverse overlapping parts of ODs, mainly the beam halo particles.

3.3.5 AFP

The AFP (*ATLAS Forward Proton*) detector is dedicated to the registration of the diffractively scattered protons. Four stations are located at two sides of IP1 at $|z| = 205$ m (Near Stations) and $|z| = 217$ m (Far Stations). Similar to the ALFA detectors, the AFP detectors are placed inside Roman Pots. These Roman Pots allow horizontal insertion of the detectors into the LHC beam pipes. The AFP detectors are fully described in Section 3.4.

3.4 The AFP Detectors

3.4.1 LHC magnet structure in the vicinity of the ATLAS interaction point

The proton beams at the LHC are steered by the magnetic lattice. It is responsible for shaping the orbits of protons beams, focusing the beams close to the interaction points and separating them from each other when they leave the interaction point areas.

The magnet structure in the vicinity of the ATLAS detector consists of drift spaces where protons go in straight lines and sets of magnets, including dipole and quadrupole magnets. Dipole magnets are responsible for bending the nominal orbit of the beams. Quadrupole magnets take care of changing the beam transverse shape, which can be expressed in focusing and defocusing terms. However, they will only influence trajectories of those protons which are not exactly in the beam axis. The absence of magnets with multipole field expansion moments higher than the quadrupole ones ensures the independence of the proton horizontal trajectory position and its momentum vertical component and vice versa.

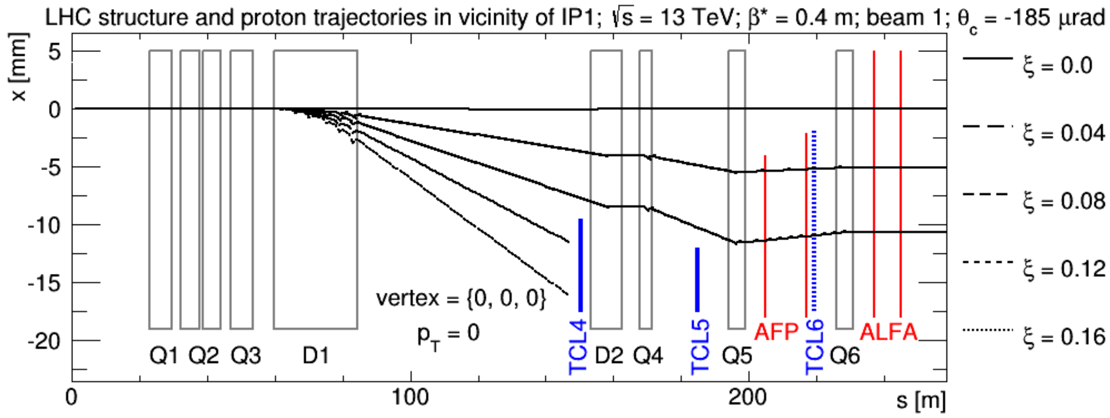

Figure 3.17: The LHC magnet structure close to the ATLAS interaction point. The quadrupole magnets are labelled with the letter Q while the dipole ones with the letter D. Objects labelled with “TCL” are the collimators. Different lines represent diffractively scattered protons trajectories in $s-x$ plane (on side C) depending on the proton ξ, for protons with $p_{\mathrm{T}}=0$. Courtesy of Maciej Trzebiński.

Magnets installed in the vincinity of the IP1 are presented in Fig. 3.17. On a way of the diffractively scattered proton moving from IP1 to the AFP detectors there is a set of dipole and quadrupole magnets. The settings of these magnets have a direct impact on the position of the diffractively scattered protons at the AFP detector location. The final focusing triplet (Q1, Q2 and Q3) is positioned about 40 m away from IP1. Other quadrupoles (Q4, Q5 and Q6) are located around 160 m, 190 m and 220 m from IP1. Between the IP1 and AFP two dipole magnets are installed, D1 at 70 m and D2 at 150 m. TCL4 and TCL5 collimators protect the magnets from stray particles (*beam halo*) and radiation induced by them which may cause the magnet quenching [74]. Collimator TCL4 is installed in front of the D2 dipole whereas TCL5 in front of the Q5 quadrupole magnet. Downstream the AFP detector an additional collimator, TCL6, is placed. Its role is to protect the ALFA detector.

When a diffractively scattered proton traverses through the described above magnetic fields, its trajectory depends both on its scattering angle (transverse momentum) and its energy. One can imagine a situation when it passes the beam pipe with p_{T} equal to zero. Then, when it encounters the quadrupole magnet along its magnetic axis, no change of its trajectory takes place, regardless on its ξ value. The property that will differentiate it from the beam protons will be its z momentum component, p_z. However, if it is within some distance from the beam center, its further trajectory depends on its ξ and the quadrupole orientation and settings. In effect, if a diffractively scattered proton comes across few quadrupole magnets defocusing in a given direction, it can be significantly separated from the beam center.

Dipole magnets in the LHC are designed to bend the beam trajectory only in $x-z$ plane, therefore they do not influence the y position of protons. The action of the dipole magnet on a diffractively scattered proton depends on p_z. When a proton has a non-zero ξ value, its trajectory will be bend at larger angle than the beam, resulting in separation of the diffractively scattered proton from the beam in the x direction. The larger ξ is, the larger is the separation of the diffractively scattered proton from the beam.

Example trajectories in $s-x$ plane of diffractively scattered protons with $p_{\mathrm{T}}=0$ and non-zero ξ are presented in Fig. 3.17, while the trajectories of diffractively scattered protons in $s-x$ and $s-y$ planes, with non-zero p_{T} and $\xi=0$, are shown in Figs. 3.18 and 3.19, respectively.

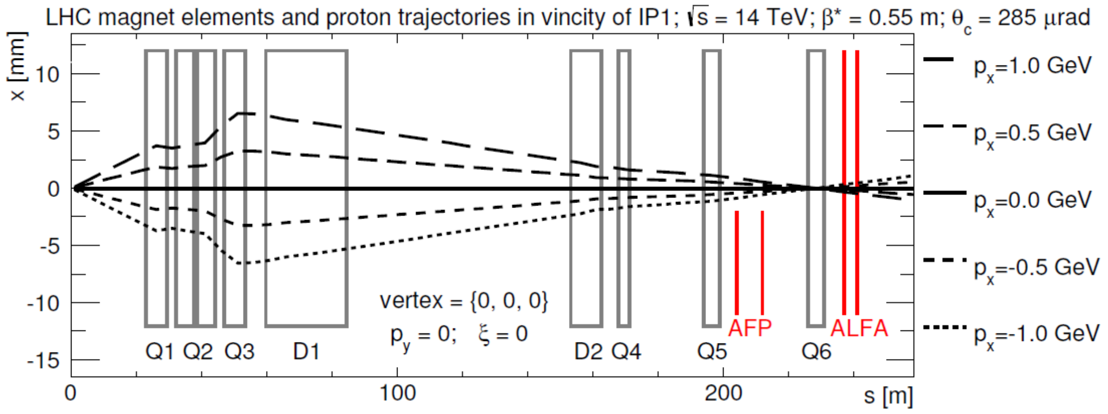

Figure 3.18: p_y momentum dependence of the proton trajectory in the $s-x$ plane (side C) for $\sqrt{s}=14$ TeV, $\beta^*=0.55$ m and the crossing angle in horizontal plane $\theta_{\mathrm{c}}=285$ μrad. Protons were generated at point $(0,0,0)$ with different p_y momenta and with $\xi=0$. Irrespectively of p_y value, protons with $\xi=0$ do not reach AFP detectors. From [50].

It is necessary to mention that a diffractively scattered proton, already separated from the beam, may also encounter a collimator on its way. If the proton ξ will be too large, such a proton will collide with the accelerator beam pipe or a collimator and eventually will be removed. The

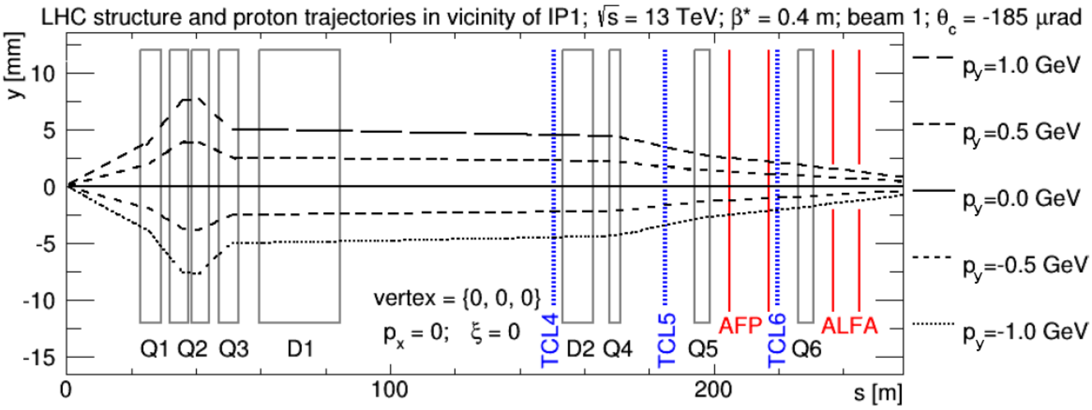

Figure 3.19: p_x momentum dependence of the proton trajectory in the $s-y$ plane (side C) for $\sqrt{s} = 13$ TeV, $\beta^* = 0.4$ m and the crossing angle in horizontal plane $\theta_c = -185$ μrad. Protons were generated at point (0,0,0) with different p_x momenta and with $\xi = 0$. Courtesy of Maciej Trzebiński.

positions of TCL4 and TCL5 collimator jaws were set to the distance of 15σ and 35σ from the beam, respectively.

3.4.2 Detector construction

As noted earlier, the AFP detector consists of two stations on each side of the ATLAS interaction point. Layout of the detector is presented in Fig. 3.20.

Roman Pots

The AFP stations use the Roman Pot technique. A single AFP Roman Pot station (see Fig. 3.21) contains the pot and the mechanics positioning it in the vicinity of the beam. It uses a stepper motor. In case of non-stable beams, the AFP detectors are kept in a so-called garage position (about 40 mm from the beam). During the data-taking, they are at a distance of 2-3 mm from the beam center.

Silicon Tracker

Each of the stations contains the Silicon Tracker detector (SiT). Silicon Tracker is a high resolution 3D silicon pixel detector, consisting of the pixel planes, each of them containing 336×80 pixels of a size 50 μm × 250 μm, in x and y directions, respectively. The pixel thickness is 230 μm. The total active area of a single pixel plane is 1.68×2.00 cm^2. To achieve a good position resolution, each SiT detector consists of four pixel planes. The distance between planes is 9 mm. In addition, the planes are alternately staggered in y direction by a quarter of the pixel width (see Fig. 3.22).

Silicon detectors are positioned almost perpendicularly to the beam (almost in the $x-y$ plane), rotated at the angle of 14° around an axis parallel to the y axis and passing through the edge of the plane placed closer to the beam (it is visible in Fig. 3.20 and Fig. 3.23(a)). This

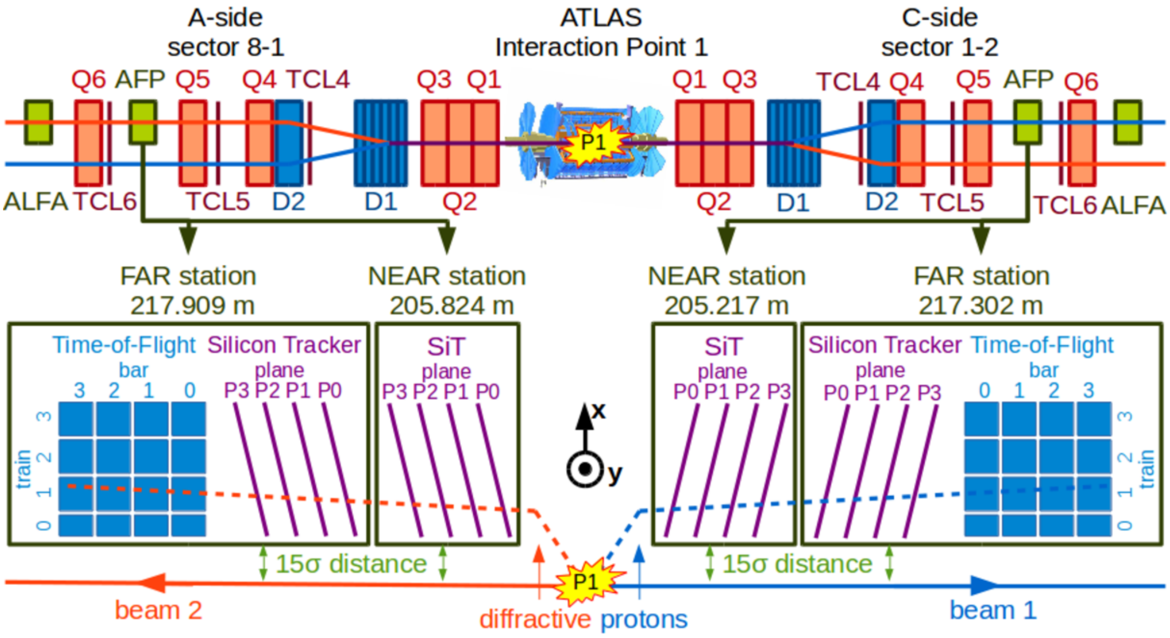

Figure 3.20: Layout of the AFP detectors. The upper part shows location of the AFP in the vicinity of IP1, magnet system and ALFA forward detectors. The lower part presents subdetectors placed in each of the AFP stations together with the diffractively scattered proton trajectories. From [75].

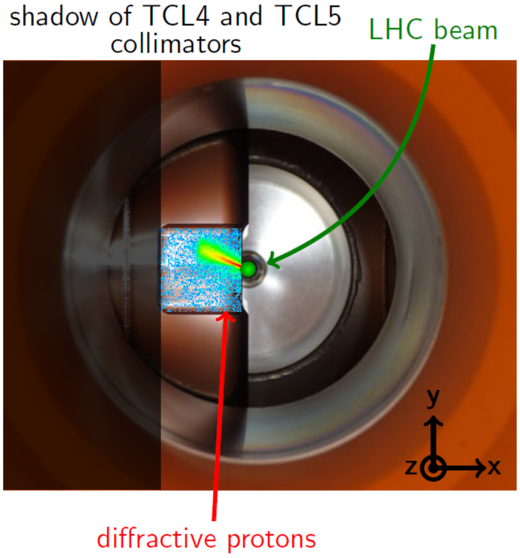

Figure 3.21: Roman Pot seen from the inside of the beam pipe, with a pot inserted very close to the beam. On a pot surface the pattern left by protons reaching the AFP was added. Courtesy of Maciej Trzebiński.

rotation is dictated by the fact that trajectories of the diffractively scattered protons are almost parallel to the beam (the mean trajectory slope is about 20 μrad) and allows improvement of

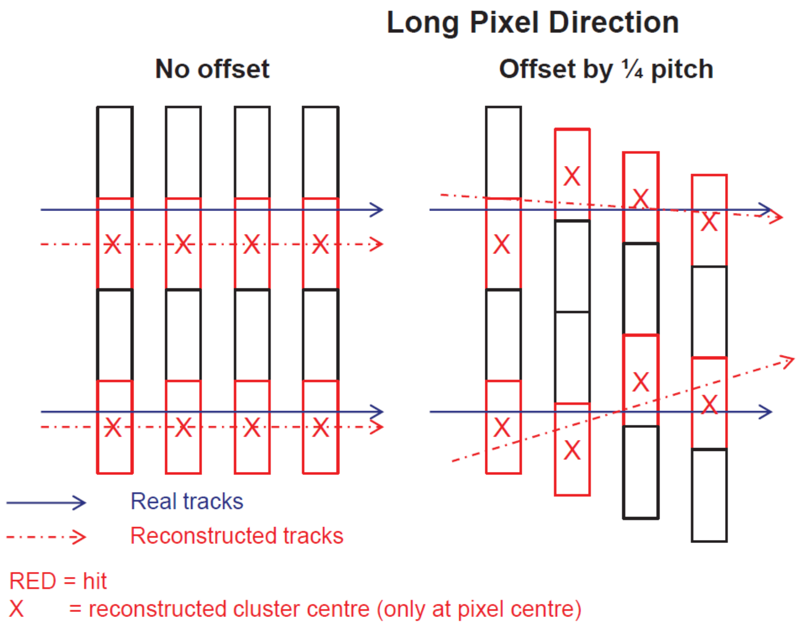

Figure 3.22: Sketch of the track reconstruction in y direction in case of non-staggered planes (left) and staggered planes with an offset of 1/4 of bin width between successive planes (right). From [76].

the x position resolution. While passing through a perpendicular pixel plane, the electric charge would be induced mainly in only one pixel. The plane tilting allows the charge sharing between few adjacent pixels (see Fig. 3.23). Finally, the position reconstruction resolution is about 10 μm in x direction and about 30 μm in y direction [76].

Time of Flight detector

Far Stations, besides the SiT detector, may host also the Time of Flight (ToF) detector [76]. ToF system is designed to measure the arrival time of the scattered protons. The difference of the arrival times allows determination of whether two protons, registered on the opposite sides of the IP, come from the same primary vertex and relating it to the vertex reconstructed by the ATLAS ID. For the AFP low-luminosity physics program, the ToF detector is not required.

The ToF detector is a set of L-shaped quartz bars (LQbars) which guide the Cherenkov light created by protons. They are oriented at the Cherenkow angle of 48° with respect to the beam-axis [76]. The created Cherenkov light passes along the radiators to the 90° bend and is guided to the photomultipliers. The baseline solution consists of 16 LQbars organised into four rows of four LQbars each, as presented in Fig. 3.24. The time measurement resolution is about $20-50$ ps.

Roman Pots position control

The beam optics determines the size of the beam at the detector location. To avoid potential

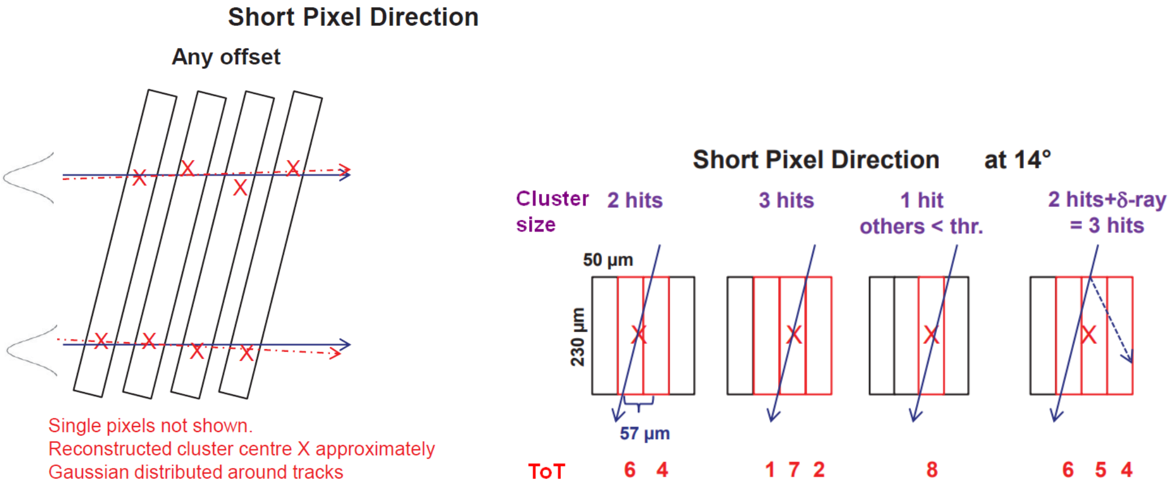

(a) (b)

Figure 3.23: (a) Sketch of the track reconstruction in case of tilted silicon planes. View from above. (b) Sketch of the pixel hits and clusters in case of tilted planes. ToT is time-over-threshold (given values are examples). View from above. From [75].

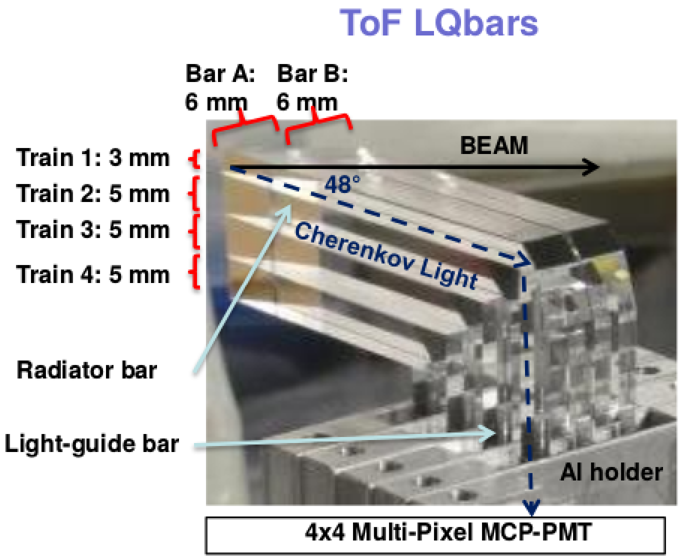

Figure 3.24: Main part of the ToF detector: 16 L-shaped quartz bars guiding Cherenkov light, organised into four rows (so-called trains). From [75].

damages, the detectors cannot be placed too close to the beam. Thus, the distance of the detector from the beam center (equivalently, the distance of the detector from the edge of the beam pipe) has to be precisely controlled.

Precise knowledge of the actual detector position is also essential for the proton kinematics reconstruction. In order to obtain a 10% resolution in ξ, the required relative horizontal alignment precision of the stations is 100 μm and 200 μm for the absolute horizontal alignment precision [76].

Three systems are involved in the detector position control. The pot movement is controlled by a precise stepper motor which accuracy is up to 5 μm. The motor displayed position is cross-checked with a precise Linear Variable Differential Transformer (LVDT) readout and with a resolver readout [77]. For the safety reasons, the detector position is not only monitored but in case of a power failure the Roman Pot can by mechanically retracted using dedicated springs [6].

Position of the Roman Pot station with respect to the beam is determined in the so-called beam based alignment (BBA). BBA is a special LHC run performed for every machine optics planned to be used. The main goal of this run is to determine the beam size at every collimator setting, for each of the LHC collimators. For that purpose, each jaw of the collimator is moved separately towards the beam trajectory, in 5 μm steps, until a peak appears in the signal of the Beam Loss Monitors (BLM) [78].

From the AFP point of view, the goal of the BBA is to correlate the beam position with the AFP position settings readout. It is a cornerstone of the AFP alignment with respect to the beam center. In this procedure, the AFP detectors are slowly approaching the beam, which was already trimmed by the collimators to a known width, until the contact, i.e. appearance of the BLM peak (see Fig. 3.25).

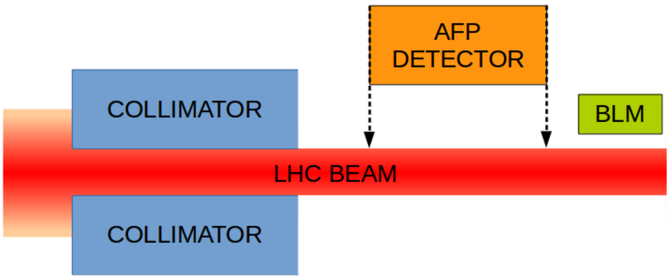

Figure 3.25: BBA: procedure of determining position of the AFP detector with respect to the center of the LHC beam. A beam was trimmed by the collimators at the known width expressed in terms of σ. Courtesy of Maciej Trzebiński.

3.4.3 Detector acceptance

The optics magnets settings together with the shape of the beam chamber between IP1 and the AFP determine the measurement capabilities of the AFP detectors. Not all of the diffractively scattered protons can be registered in the detectors. The geometric acceptance is defined as the ratio of the number of protons with a given relative energy loss (ξ) and transverse momentum (p_{T}) that reached the AFP detector to the total number of protons having given ξ and p_{T}. The AFP acceptance depends on the distance (d) of the detectors edge from the beam, hence on the horizontal position of the detectors. At the optics of $\beta^* = 0.4$ m this is $15\sigma + 500$ μm from the center of the beam. Fig. 3.26 presents the geometric acceptance for the AFP detector located in the Near Station. The region of high acceptance (> 80%) is limited by $p_{\mathrm{T}} < 2.5$ GeV and $0.02 < \xi < 0.10$. Small ξ values are limited due to the beam-detector distance whereas large ξ values are cut due to the collimators settings.

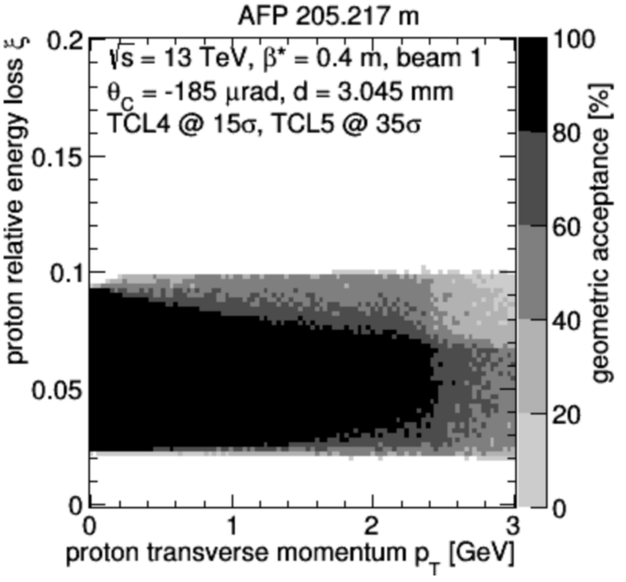

Figure 3.26: Geometric acceptance of the AFP detector in the Near Station on the side C as a function of the proton relative energy loss ξ and its transverse momentum p_{T}. The distance d was set to 15σ and 500 μm of detectors dead material was added. Courtesy of Maciej Trzebiński.

3.4.4 AFP TDAQ

Trigger

The AFP detector provides an L1 trigger signal [79], which is later sent to the ATLAS trigger system. The AFP detector trigger signal in each station is based on the SiT detector. On the side C, three out of four SiT planes are used for triggering while on the side A two out of four. The trigger signal is obtained as follows:

1. Once a particle crosses a given SiT plane, a hit signal of an OR of all the pixels in the pixel sensor (so-called hitOR) is sent to the station hitbus chip.

2. The hitbus chip combines hitOR signals from silicon planes, resulting in a signal from any of the possible trigger logics. These logics include: single channel signal pass-through, logical OR/AND of the three inputs and a majority vote logic (i.e. two-out-of-three trigger signal) [80]. The combined signal is synchronized with the LHC clock within the hitbus chip.

3. Eventually, the signal is sent from the station through an almost 300 m long optical fibre to the ATLAS Central Trigger Processor (CTP).

In this analysis the L1 trigger formed as the logical AND of both stations on the side C was used. Since the trigger information is based only on the logical combination of hits in given planes, then if a particle is within the AFP geometric acceptance, the AFP trigger efficiency does not depend on particle kinematics.

Data Acquisition (DAQ)

The main component of the AFP data acquisition system is the High Speed Input Output (HSIO) board [79]. Two such boards receive data from the SiT and ToF detectors and also send commands and clock signal back to them. The data from the HSIO are sent to the ATLAS readout system, which is an interface between the detector specific DAQ and the central ATLAS DAQ. The readout system gets event information fragments from AFP DAQ and includes into full event structure.

3.4.5 Detector Control System (DCS)

The AFP Detector Control System (DCS) [77], which is integrated with the ATLAS DCS system, controls the safe operation of the AFP detector. It has several functions. First of all, it controls the supply and pressure in the components of the detector. It also controls the Roman Pot stations movement and continuously monitors the most important detector parameters. In case of some technical problems with the detector operation, the DCS signals any anomalous behaviour and performs pre-programmed actions. Furthermore, the DCS stores a predefined subset of the detector parameters in the on-line data bases for later inspections. A graphical user interface has been prepared to allow the visualisation of the detector state as well as the control of its operation (see Appendix C).

CHAPTER 4

EVENT RECONSTRUCTION

After accepting events by the ATLAS trigger system, the objects of interest such as electrons, jets or forward protons have to be reconstructed from the low-level detector signals, like information from the tracking detectors, energy deposits in the calorimeters or information from any other dedicated subdetectors. Below the reconstruction of objects used in this analysis is described.

4.1 Track reconstruction in the Inner Detector

The track reconstruction in the Inner Detector consists of two parts [55, 81, 82]. Firstly, the reconstruction of the tracks of primary particles, i.e. particles with mean lifetime, τ, larger than $3 \cdot 10^{-11}$ s, either directly produced in pp interactions or from subsequent decays of directly produced particles with $\tau < 30$ ps, is performed using the *inside-out* algorithm [81]. This algorithm starts from the most central part of the Inner Detector. The Pixel Detector and SCT hits are used to create the three-dimensional objects referred to as *Space Points*. In the Pixel Detector, a *Space Point* is the center of a cluster of pixels. In the SCT, a *Space Point* is constructed by finding the intersection of the strips on the front and back sides of a module. Next, the algorithm performs a fast z-vertex scan using all the *Space Points*. The vertex x and y coordinates are taken from the centre of the assumed beam spot. Then, starting from the determined nominal interaction point, the successive *Space Points* located further away from the interaction point are merged into a track seed (see Fig. 4.1). This is performed using a combinatorial Kalman filter [83] which combines forward filtering, backward smoothing and an outlier rejection.

Once the track seeds are found, a narrow path is set up along each of them. The *Space Points* falling within such a path are collected and a full track fit is performed (see Fig. 4.2). If any

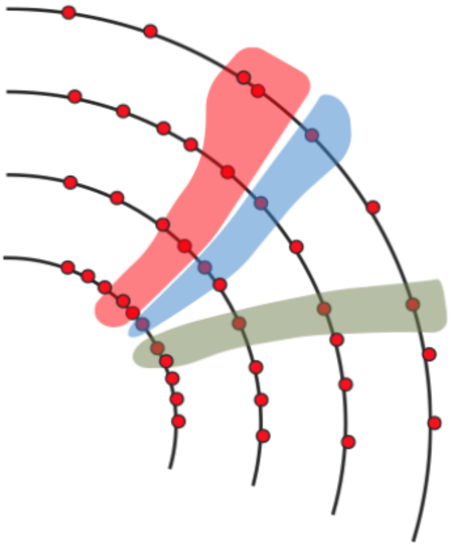

Figure 4.1: Result of the track seeds searching procedure within the Pixel Detector and the SCT in the Inner Detector. Red dots are the *Space Points*. Colored areas represent found track seeds pointing towards the determined nominal interaction point. From [84].

ambiguities in the track forming process occur, they are resolved and then the track candidates are extrapolated into the TRT.

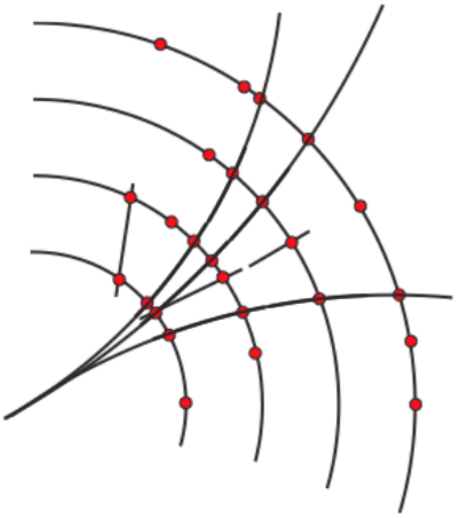

Figure 4.2: Result of the track fitting procedure within the Pixel Detector and the SCT in the Inner Detector. Red dots are the *Space Points*. Black lines are the reconstructed tracks. From [84].

Subsequently, the track parameters: φ_0, θ_0, d_0, z_0 and q/p are reconstructed. These paramaters are defined in a reference point of the closest approach of the track to the z axis: φ_0 is the angle in the $x-y$ plane at this point, θ_0 is the angle with the z axis, d_0 is the signed distance to the z axis – it is defined to be positive when the direction of the track is clockwise with respect to the origin. The z_0 is the z coordinate of the reference point within the ATLAS reference system and q/p is the ratio of the charge to the momentum of the particle. The tracks reconstructed by the *inside-out* algorithm are required to have $p_\mathrm{T} > 400$ MeV. The whole procedure is schematically shown in Fig. 4.3.

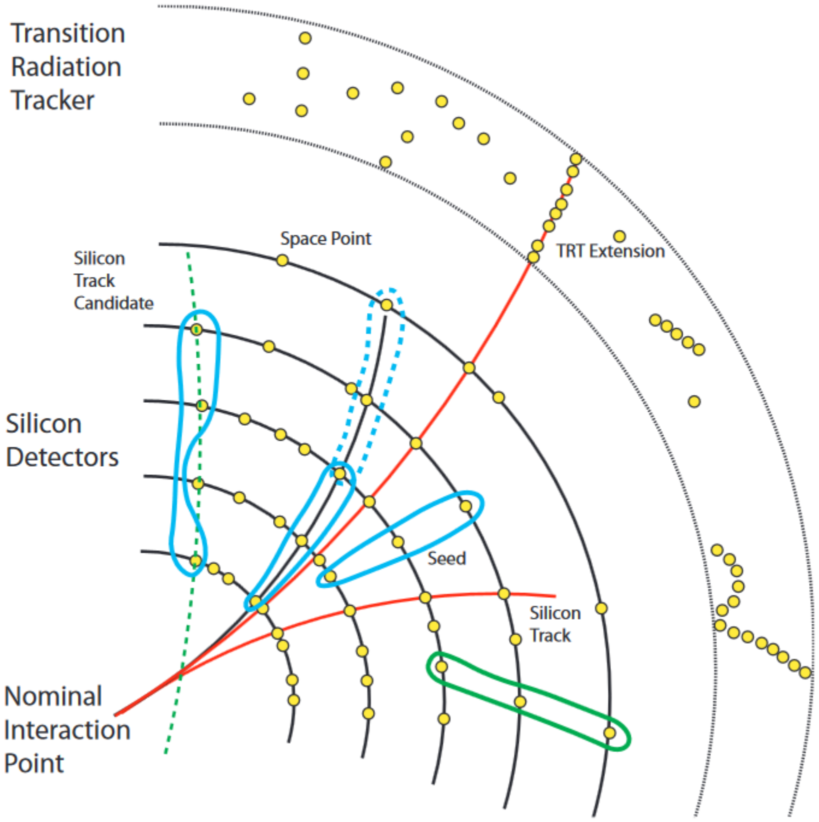

Figure 4.3: A scheme of the track reconstruction within the Inner Detector, presented at diffrent stages of a reconstruction. At first, the Space Points (yellow dots) are created. Then the nominal interaction point is calculated and track seeds pointing towards it are formed (areas marked with blue and green solid lines). Subsequently, track candidates are fitted and then accepted (blue dashed lines) or rejected (green dashed lines). Finally, tracks are extended towards the TRT (red solid lines). "Silicon Detectors" stands both for the Pixel and SCT. From [55].

The second step of the track reconstruction is the application of the *outside-in* algorithm, which is a back-tracking. It aims at the reconstruction of secondary particles which result from interactions of primary ones. Tracks of secondary particles are observed further inside the Inner Detector volume thus they may not be reconstructed by the *inside-out* algorithm. A track search starts from segments reconstructed in the TRT. The TRT drift tubes do not provide any information about the coordinate along the straw direction thus the reconstruction of segments has to be done in projective planes. In the barrel region this is the $r-\varphi$ plane and in the end-cap regions the $z-\varphi$ plane. If the tracks originate from the nominal interaction point, then the TRT track segments from tracks with $p_{\mathrm{T}} > 500$ MeV appear as straight lines in the selected planes [81]. The Hough transform [85] is used to reconstruct segments in the TRT. Selected track candidates are successively tracked back into the SCT and Pixel detector and the secondary vertices are found.

4.2 Vertex reconstruction in the Inner Detector

The reconstruction of the interaction vertiex is based on the tracks reconstructed in the Inner Detector and exploits an iterative algorithm [86].

In the first step, the tracks used for the primary vertex reconstruction are preselected – they have to originate from primary interactions so they have to be compatible with the expected beam spot region. Thus the following criteria are imposed:

- $p_{\mathrm{T}} > 400$ MeV,
- $|d_0| < 4$ mm,
- $\sigma(d_0) < 5$ mm,
- $\sigma(z_0) < 10$ mm,
- at least 4 hits in the SCT,
- at least 9 hits in the Pixel and SCT,
- no Pixel holes, at most one SCT hole, where a hole is defined as a non-existing but expected hit on a given track trajectory.

Then the so-called vertex seed is selected. For this purpose, the tracks are extrapolated to the beam-axis and their z positions are used to set the vertex seed. An exact vertex position is calculated by an iterative χ^2 fit of the tracks nearby to the vertex seed. Tracks incompatible with the vertex are used to seed a new vertex – the procedure is repeated until no unassociated tracks are left or no additional vertices can be found. Reconstructed vertices are required to contain at least two tracks.

Both the transverse and longitudinal position resolution of the reconstructed primary vertices is approximately 2 mm when there are only two or three tracks present in the event. For events with high track multiplicities, approaching 70, it is 30 μm in the transverse plane and 50 μm along the longitudinal direction [86].

4.3 Reconstrucion of calorimeter clusters

The ATLAS calorimeters measure the energy deposits of passing particles and positions of these deposites in the cells. During the reconstruction procedure, the signals of all the calorimeter hits are corrected for the local calorimeter channel defects and associated with the calorimeter cells. The cluster reconstruction starts with a selection of a *cluster seed*. This is the cell in which the measured signal is at least four standard devations above the average noise of that cell. All the neighbouring cells are added to the cluster. If one of the added cells has the energy deposit greater than two standard deviations above the average noise, it becomes a secondary seed for which the procedure is repeated. This procedure results in a collection of calorimeter *topological clusters* [87].

Calorimeter topological clusters can be used to calculate the proton relative energy loss [88, 89]. A variable ξ_{cal} is defined as:

$$\xi_{\text{cal}} = \frac{1}{\sqrt{s}} \sum_i p_{\text{T}}^i e^{\text{sgn}(\eta_{\text{p}})\cdot\eta_i}\,, \tag{4.1}$$

where the sum runs over all calorimeter topological clusters. Parameters p_{T}^i and η_i coreresspond to the centers of calorimeter cells while η_{p} is the proton pseudorapidity.

4.4 Proton trajectory and kinematics reconstruction in the AFP detectors

A proton scattered at (x_0, y_0, z_0) is fully described by three independent variables, its energy and two emission angles: $\left(E, x_0', y_0'\right)$. It can be represented also in terms of the energy and components of transverse momentum: $\left(E, p_x, p_y\right)$ or only momentum components: $\left(p_x, p_y, p_z\right)$.

A diffractively scattered proton, after leaving the interaction point, passes through the accelerator lattice (see Section 3.4.1). Therefore, its trajectory depends not only on the emission angles but also on its energy.

The AFP delivers information about the diffractively scattered proton hit positions in each silicon plane in each station. These can be further translated into the diffractively scattered proton trajectory positions in two stations: $(x_{\text{Near}}, y_{\text{Near}})$, $(x_{\text{Far}}, y_{\text{Far}})$ or, equivalently, into position of the proton trajectory in a given station: $(x_{\text{AFP}}, y_{\text{AFP}})$ and proton trajectory elevation angles: x_{AFP}', y_{AFP}'. Knowing the position of the proton trajectory in the AFP detectors, the goal is to reconstruct full information about its momentum components at the interaction vertex.

4.4.1 Proton trajectory reconstruction

A diffractively scattered proton, after reaching the AFP detector, interacts with the detector material. Below, the algorithm leading from the electric charge deposits generated in the AFP silicon planes to the proton trajectory reconstruction is presented.

1. Traversing particle deposits energy by ionizing the detector material. Deposit of the electric charge in a pixel is called a **hit**.

2. Neighbouring hits within each silicon plane are combined into **clusters** – as discussed in Section 3.4.2, a diffractively scattered proton is expected to hit two or three pixels in a given plane.
3. The cluster position (x, y) is calculated as the charge-weighted mean of the pixel center positions.
4. Clusters used in a track reconstruction are selected.
5. Each **track** is built out of clusters. Its parameters (positions and slopes) are reconstructed by fitting a linear function to the centers of clusters in $x - z$ and $y - z$ planes.
6. A **proton trajectory** (a proton) is reconstructed from two tracks – one passing through the Near Station and the other one through the Far Station. It is requested that the transverse distance between them has to smaller than 2 mm.

4.4.2 Proton kinematics reconstruction

The procedure of the proton transport and reconstruction is schematically depicted in Fig. 4.4.

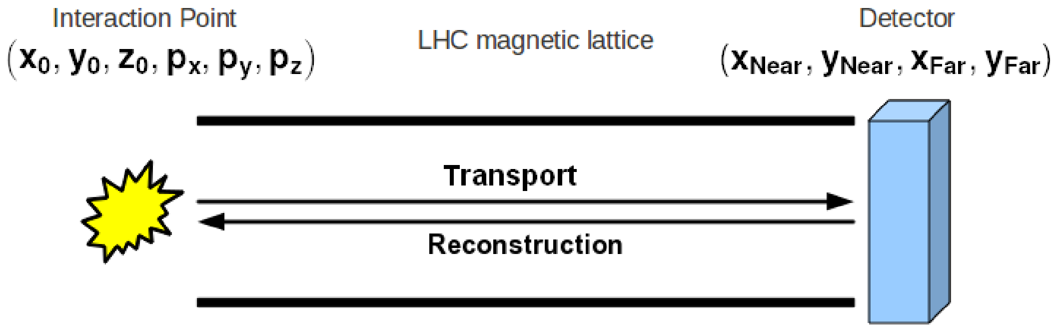

Figure 4.4: A scheme representing reconstruction of the proton kinematics for diffractively scattered protons measured in the AFP in case of MC events. At first, a proton with a known position of the interaction vertex and kinematics is transported into the AFP so its trajectory at the AFP is known. Then, from the AFP estimated proton trajectory, the proton kinematics is disentangled in the reconstruction process. The true and reconstructed parameters of the proton should be the same (or similar in case of the angular divergence at the IP and the detector smearing in the AFP applied). Courtesy of Maciej Trzebiński.

To disentangle information about the proton kinematics at the interaction point, the interaction vertex position is set to $x_0 = y_0 = z_0 = 0$ (one can also use information about interaction vertex position delivered by the ATLAS ID). Due to this assumption one can reduce the inversion problem of the 4 to 6 mapping (four coordinates delivered by the AFP to three proton spatial coordinates and three proton components of momentum) to 4 to 3 mapping.

The method of the proton kinematics reconstruction exploits the knowledge of the properties of the proton transport from the interaction point to a certain point located along the beam pipe. Assuming position of the interaction vertex and the scattered proton momentum components, one will get the position of a proton transported to the both AFP stations (situated at known z_{Near} and z_{Far}): $(x^{\text{trans.}}_{\text{Near}}, y^{\text{trans.}}_{\text{Near}})$, $(x^{\text{trans.}}_{\text{Far}}, y^{\text{trans.}}_{\text{Far}})$. One should note that such transport calculations can be performed in various ways. For example using Mad-X [90], the ATLAS delivered transport code FPTrack [91] or parametrisation of results of these programmes [92].

The proton kinematics is directly reconstructed by the minimization of a $\chi^2(\vec{p})$ function with respect to the proton momentum $\vec{p}$. It is done with help of ROOT `MINUIT` package [93]. This function has the following form:

$$\chi^2(\vec{p}) = \left[\frac{x^{\text{trans.}}_{\text{Near}}(\vec{p}) - x^{\text{meas.}}_{\text{Near}}}{\sigma_{x_{\text{Near}}}}\right]^2 + \left[\frac{y^{\text{trans.}}_{\text{Near}}(\vec{p}) - y^{\text{meas.}}_{\text{Near}}}{\sigma_{y_{\text{Near}}}}\right]^2 + \left[\frac{x^{\text{trans.}}_{\text{Far}}(\vec{p}) - x^{\text{meas.}}_{\text{Far}}}{\sigma_{x_{\text{Far}}}}\right]^2 + \left[\frac{y^{\text{trans.}}_{\text{Far}}(\vec{p}) - y^{\text{meas.}}_{\text{Far}}}{\sigma_{y_{\text{Far}}}}\right]^2, \tag{4.2}$$

where $\vec{p}$ is the proton momentum, $x^{\text{meas.}}_{\text{station}}$ and $y^{\text{meas.}}_{\text{station}}$ correspond to the position of measued proton trajectory and $\sigma_{x_{\text{station}}}$ and $\sigma_{y_{\text{station}}}$ are the position reconstruction resolutions (see Section 3.4.2).

FPTrack program computes the positions of particles using the optics files (the so-called *Twiss files*). They are produced using Mad-X [90] which is a principal beam transport program used by the LHC team. A faster method of the transport calculation is the use of the parameterisation of results delivered by Mad-X or FPTrack [92]. This method was used for the experimental data. In the presently available MC, combined with the ATLAS Geant4 simulation, information about the AFP hits is not simulated. The proton transport into the AFP is done using FPTrack During the proton transport simulation, the effects of the SiT detector resolutions and the multiple scattering are applied. Then the proton kinematics is reconstructed as described above.

A good proton trajectory reconstruction requires a good knowledge of the detector alignment. Otherwise, the reconstructed positions of the proton trajectory in the AFP detectors may be far from the true ones and lead to a wrong estimation of the proton kinematics. One should remember that the kinematics reconstruction is sensitive to the LHC optics.

4.4.3 Detector alignment

Alignment of the AFP station (four silicon planes) is divided into two parts:

(a) local alignment – shift and rotation of each plane in the station,

(b) global alignment – shift and rotation of the whole station.

At first, the **local alignment** procedure is run. The general idea of performing alignment of the silicon planes is schematically shown in Fig. 4.5 using an example of two shifted planes. Genuinely (picture signed as "reality"), the planes are shifted with respect to each other. In this example a proton trajectory marked by a blue line is exactly horizontal. However, without an alignment correction (picture "before alignment") positions of the planes were assumed to be the same in a vertical direction. It results in a vertical shift between hits left in the planes, marked by small crosses. The track reconstruction performed with the assumption that the track slope should be horizontal (picture "track reco."), as the diffractively scatered proton trajectories ale almost parallel to the beam, results in a track marked by red dashed line that do not pass though any of the hits. Without this assumption the reconstructed proton trajectory would be heavily rotated. The alignment correction uses the horizontally reconstructed track. The residual value, defined as distance between the reconstructed track position and the hits position is calculated (picture "alignment correction"). In an iterative procedure the residual values are minimized. Finally, each of the planes is shifted by the calculated value to its proper position.

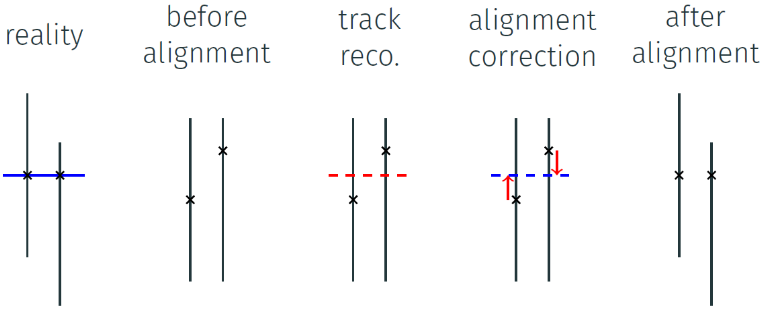

Figure 4.5: The concept of the local alignment correction on the example of two detector planes. Full description in the text. Courtesy of Rafał Staszewski.

Once the local alignment is settled and tracks are reconstructed, the **global alignment** is being determined. A goal of this procedure is to determine the distance of the SiT detector active area from the beam center, Δ_{SiT} (see Fig. 4.6). This distance can be expressed as:

$$\Delta_{\mathrm{SiT}} = \Delta_{\mathrm{beam}} + \Delta_{\mathrm{tracker}} + \Delta_{\mathrm{RP}}\,. \tag{4.3}$$

The beam position with respect to the center of the beam pipe, Δ_{beam}, is calculated during the BBA. The distance of the SiT active area from the Roman Pot wall, $\Delta_{\mathrm{tracker}}$, which includes the detector floor thickness, the detector-floor distance and the dead edge width, is known and set to 500 μm. The distance of the Roman Pot from the center of the beam pipe, Δ_{RP}, is taken from the resolver reading – this parameter is changed in a global alignment correction procedure.

A correction to the global alignment is a **relative alignment** between Near and Far stations. This correction is based on the fact that physics processes are symmetric in angle φ. Correcting for the crossing angle, the p_x and p_y distributions should be symmetric around 0.

If the relative alignment between the AFP stations is wrong, then p_x and p_y distributions will be shifted with respect to 0. To correct it, the position of one of the stations is fixed and then the second one is shifted until $\langle p_x \rangle = 0$ and $\langle p_y \rangle = 0$.

As there is a degree of freedom according to the choice of the station to be fixed, two alignment sets are available – they will be further denoted as "alignment Near" and "alignment Far". The

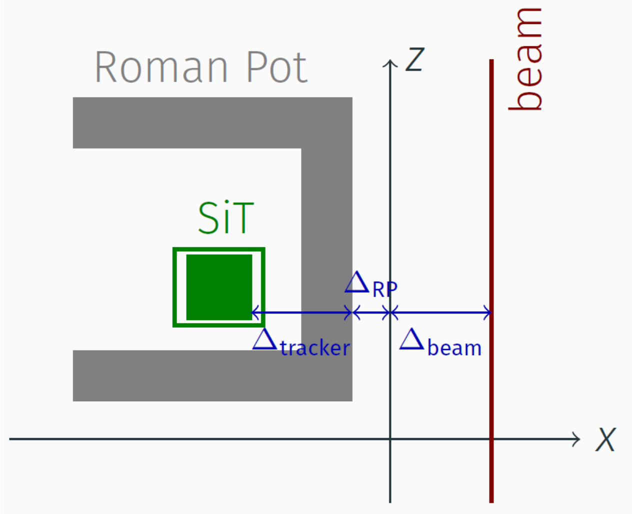

Figure 4.6: View on the Roman Pot from the top. The scale of particular distances is not preserved. Δ_{beam} is the beam position calculated during the BBA (assuming the known beam width, taken from the collimators settings), Δ_{RP} is the Roman Pot position, intended to be equal directly to the resolver position (taken from DCS) and Δ_{tracker} results from the width of the detector floor thickness, the detector-floor distance and the dead edge and is set to 500 μm. Courtesy of Rafał Staszewski.

method is sensitive to the relative alignment between the two AFP stations in both horizontal and vertical direction. Unfortunately, there is no sensitivity to the absolute alignment of each station [6].

CHAPTER

5

DATA SAMPLE AND SIGNAL SELECTION

In this chapter the data used in this analysis is described. Distributions illustrating the AFP detector performance, based on the selected Monte Carlo and data samples, are shown. In particular, the range of proton ξ in which this analysis is valid is presented and justified. Afterwards, the signal sample selection is discussed. Finally, the distributions at the detector level measured in the Innerd Detector are presented and discussed.

5.1 Data sample

Analysis presented in this dissertation has been performed based on the integrated luminosity L_{int} = 51.486 nb^{-1} of data collected in 2017 at the pp centre-of-mass energy of $\sqrt{s}$ = 13 TeV, during the AFP dedicated run (run number 336505), with β^* = 0.4 m and with $\langle\mu\rangle \approx 0.04$ (it was not constant during the run). Important parameters characterizing this run are listed in Table 5.1.

In this run the AFP detectors at both sides of the ATLAS interaction point were taking data, however, in the following only the data with the C side tag were considered due to the not fully understood the AFP detector performance on side A. Parameters related to the AFP are summarized in Table 5.2.

Table 5.1: Optics parameters during the run 336505: the centre-of-mass energy $\sqrt{s}$, the mean number of interactions per bunch crossing $\langle\mu\rangle$, the betatron function β^* and the vertical crossing angle θ_c.

$\sqrt{s}$ [TeV]	$\langle\mu\rangle$	β^* [m]	θ_c [μrad]
13	0.04	0.4	-140

Table 5.2: Parameters related with the AFP during the run 336505: the distance of the AFP detector edge from the beam in the Near Station d_{Near}, the distance of the AFP detector edge from the beam in the Far Station d_{Far} and the distance of the TCL4 and TCL5 collimators from the beam.

d_{Near} [mm]	d_{Far} [mm]	d_{TCL4} [σ]	d_{TCL5} [σ]
3.87	2.23	15	35

5.2 AFP performance distributions

Below the AFP performance distributions are presented. The proton trajectory and kinematics reconstruction were applied both to the data and MC. The alignment procedure was applied only to the data as there is no full simulation of the AFP in MC. First of all, the correctness of the algorihm reconstructing the ξ of the diffractively scattered proton was checked. For that purpose events with exactly one proton track reconstructed in the AFP on the side C were selected from the MC PYTHIA 8.2 single-diffractive sample. This MC generator was chosen also for further applications (like calculation of the track reconstruction efficiency or unfolding matrix for the track multiplicities) as it provides better description of the transverse momentum and pseudorapidity distributions. EPOS sample was used only to compare between data and MC distributions at the level of tracks and particles.

Fig. 5.1 presents the correlation of the reconstructed ξ_{reco} and the generated ξ_{truth} fractional energy loss of the diffractively scattered protons. One can see that this distribution has a very clear, narrow diagonal $\xi_{\mathrm{reco}} = \xi_{\mathrm{truth}}$. This indicates that the algorithm works correctly.

Then, the control distributions of the variables reconstructed in the AFP were made both for the data and single-diffractive MC. Events with exactly one proton reconstructed in the AFP on the side C were selected. The first is the distribution of the ξ of the proton reconstructed in the AFP (see Fig. 5.2). The MC distribution shape resembles that of the $1/\xi$ function, which is predicted by the theory [5]. For the data, a decrease of the distribution with increasing ξ is also observed, but is definitely much slower than for the MC sample. Significant discrepancies between these distributions may be partially related to the background present in the data sample. Different ranges of these distributions (a lack of events with higher values of ξ for the MC sample) result from the differences in collimator settings between the data and MC However, this divergence can be neglected in this analysis due to the cut on the ξ value introduced in the next paragraph.

The acceptance of the AFP detector, presented in Fig. 5.3, was determinated from MC as a fraction of events with a reconstructed proton in the same ξ bin as the generated proton. The acceptace plot is almost exactly flat and nearly one for $\xi \in \langle 0.035; 0.080 \rangle$. This range was chosen as a default ξ range in which this analysis was performed. Choosing a flat acceptance region

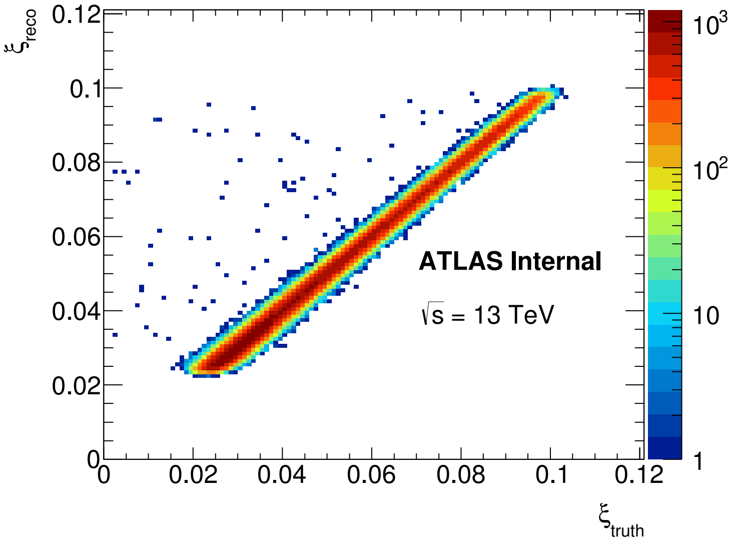

Figure 5.1: Dependence of the ξ of the proton reconstructed in the AFP: ξ_{reco} on the ξ of the generated proton which was diffractively scattered: ξ_{truth}. From PYTHIA 8.2 simulation.

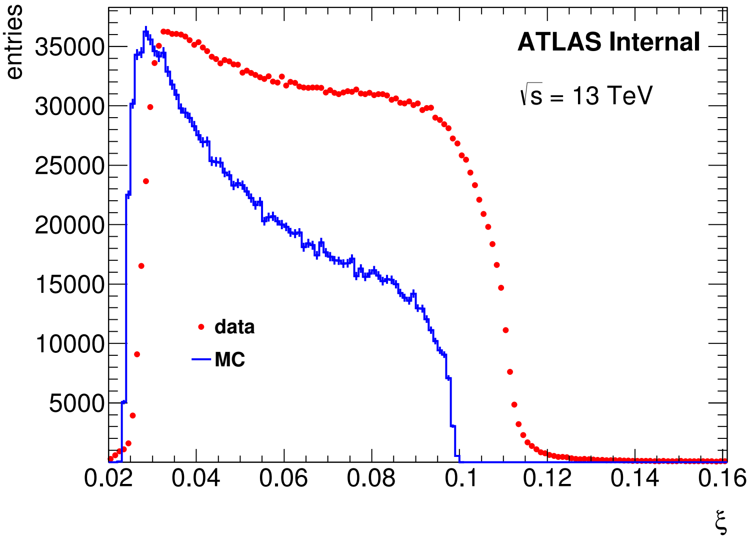

Figure 5.2: Distributions of the relatie energy loss of a proton, ξ, reconstructed in the AFP: for the data (red dots) and for MC (blue line). MC distribution was rescaled as to have a maximum of the same height as in the data distribution.

allows avoiding introducing a correction related to the AFP acceptance for different ξ values and does not remove too much of the data statistics. This range will be further divided into three bins of the same width to check the dependence of the particle distributions on the ξ value. These ranges will be the following:

(a) $\xi \in \langle 0.035; 0.050)$,

(b) $\xi \in \langle 0.050; 0.065 \rangle$,

(c) $\xi \in (0.065; 0.080\rangle$.

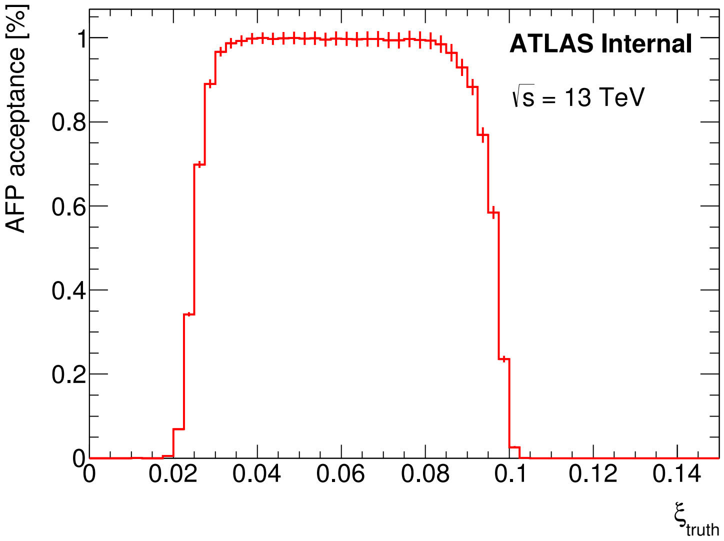

Figure 5.3: The AFP detector acceptance determined from MC as a function of ξ of the generated diffractively scattered proton, ξ_{truth}.

The following plots include the ξ cut. The distributions of the reconstructed p_x momentum component of a proton measured in the AFP are shown in Fig. 5.4. As described in Section 4.4, the AFP relative alignment was adjusted with respect to the p_x distribution, therefore the maximum of this distribution for the data should correspond to $p_x = 0$. However, one can notice that the distribution for MC is narrower and that the maximum of the data distribution is a bit shifted towards negative values. This shift may indicate on a residual misalignment in the data. The difference in widths of the distribution is related to the mismodelling of the AFP resolution.

Next plots illustrate the AFP positions of the diffractively scattered protons and the corresponding MC predictions. The upper part of Fig. 5.5 presents the (x, y) distribution of tracks that form protons in the AFP Near station, for the data (left pannels) and for the MC (right pannels). The proton beam is situated close to the right edge of the detector. The lower part of that figure concerns the AFP Far station. The shape of these distributions resembles shape of a drop and is called a “diffractive pattern”. One can notice that the distribution for the data is tilted with respect to the distribution for the MC. This is how the non-zero crossing angle manifests itself in the data distributions. One can also perceive the difference in the values of the y coordinate between the data and MC. Apart from the crossing angle effect, the discrepancy results from a lack of the AFP alignment along the y coordinate, which was not needed for the proton kinematics reconstruction and for that reason was not applied presently.

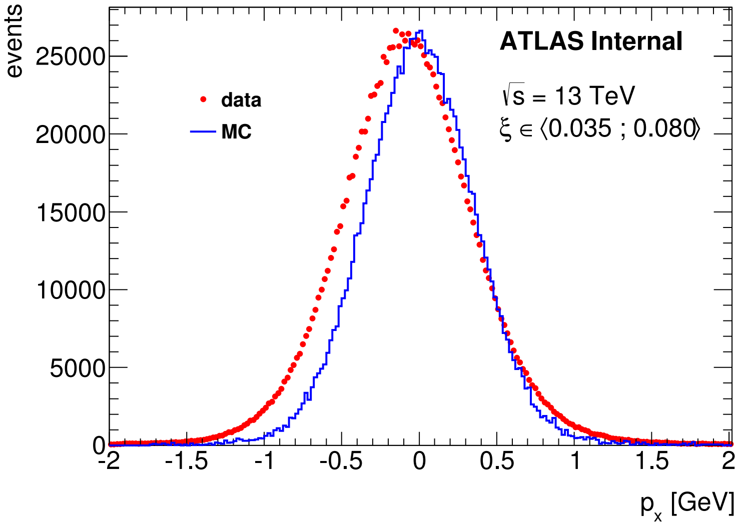

Figure 5.4: Distributions of the x momentum component p_x: for the data (red dots) and for MC (blue line). The MC distribution was rescaled to have a maximum of the same height as in the data distribution as to make the comparison of distributions easier.

As the x coordinate plays a very important role in the proton kinematics reconstruction, its distributions in the Near and Far AFP stations are presented in Fig. 5.6. One can see that the experimental distribution is slightly wider than the one for MC and that its peak is less pronounced.

In Fig. 5.7 one can see how the difference $x_{\mathrm{Far}} - x_{\mathrm{Near}}$ changes with x_{Near}. The further away is the proton from the beam, the larger is the difference. This effect is visible both for the data and MC. Finally, Fig. 5.8 shows the distribution of the difference $x_{\mathrm{Far}} - x_{\mathrm{Near}}$. This plot reveals that the distribution is more asymmetric for the data.

In summary, the distributions of diffractively scattered protons transported into the AFP differ between the data and PYTHIA 8.2. However, the main sources of observed discrepancies are understood and do not have significant impact on the final results.

5.3 Signal selection

The signal process is defined as a process where in a single bunch crossing there was exactly one interaction[1] which resulted in an experimental signature of:

- a proton reconstructed in the AFP detector,
- an interaction vertex associated with tracks reconstructed in the ID.

---

[1] interaction is defined as any process leading to the appearance of a signal in the detector

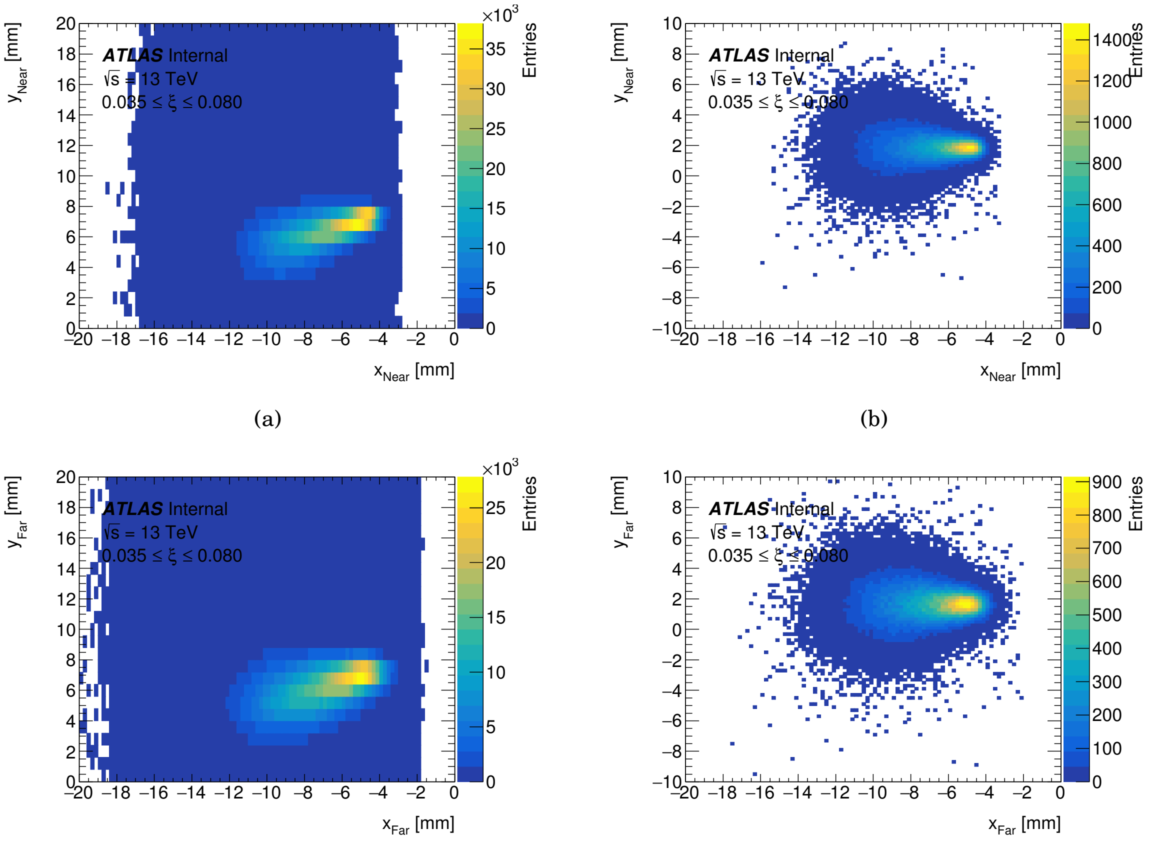

(a) (b)

(c) (d)

Figure 5.5: Distributions of proton positions in the AFP detector situated in the Near Station: data – (a), MC – (b) and in the Far Station: data – (c) and MC – (d).

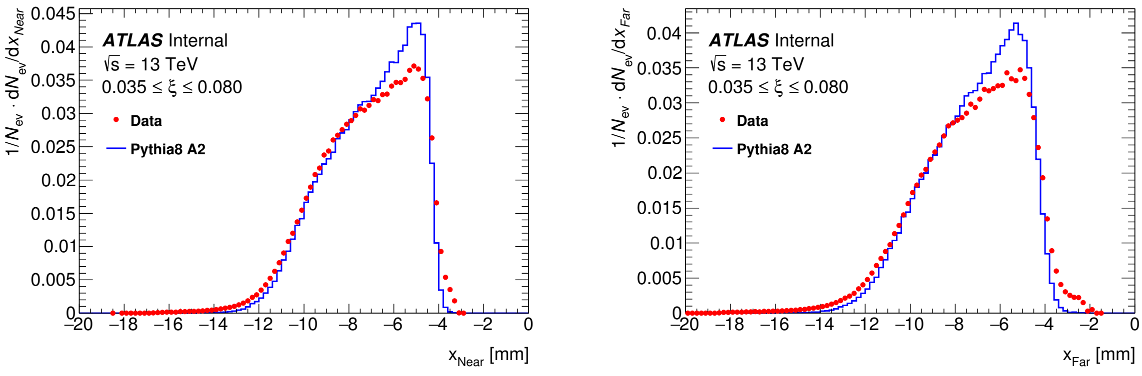

(a) (b)

Figure 5.6: The normalized distributions of a proton x position in the AFP (a) Near Station, (b) Far Station: for the data (red dots) and for MC (blue lines).

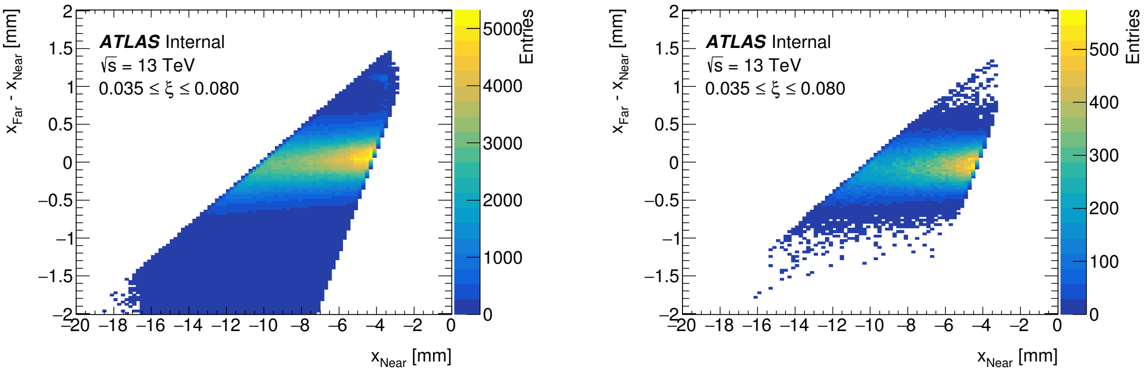

(a)

(b)

Figure 5.7: Distributions of a difference in a proton x position between Near and Far AFP Stations, $x_{\text{Far}} - x_{\text{Near}}$, as a function of its position in the Near Station, x_{Near} for (a) data, (b) MC.

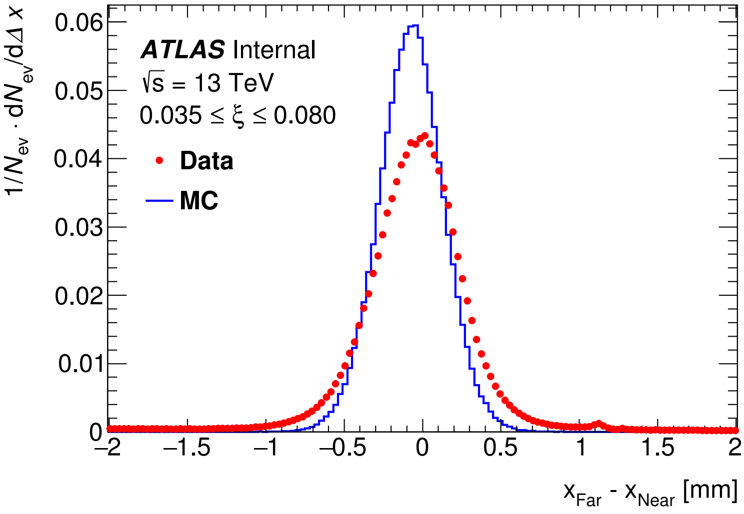

Figure 5.8: Distributions of a difference in a diffractively scattered proton x position between the Near and Far AFP stations, $x_{\text{Far}} - x_{\text{Near}}$: for the data (red dots) and for MC (blue line).

To reduce the background contribution, the signal sample was carefully selected among all registered events. The signal selection takes into account the AFP detector information, the ID information and also takes into account quality of selected data.

As already mentioned, in this analysis only the diffractive events with protons emerging on the side C of the ATLAS interaction point are of interest. To fulfill this requirement, a coincidence of both AFP C side stations was requested at the trigger level. It will be further denoted as the "AFP trigger". In this analysis the data were selected only for the range of the luminosity blocks where the trigger prescale was constant as this requirement does not remove too much of statistics but makes the analysis simpler. The prescale factor of this trigger was AFP_prescale = 20.

An event is accepted as a signal event if it fulfills the following selection criteria (otherwise it is rejected):

- the AFP trigger fired,
- exactly one proton reconstructed in the AFP on side C,
- ξ of the reconstructed proton within one of the predefined ranges,
- range of the LB with the AFP in data taking position and with constant trigger prescale (248 - 453),
- exactly one reconstructed primary vertex in the ID,
- at least one good track in the ID, where a good track is defined as having (the same track selection as in [14]):
  - transverse momentum $p_{\mathrm{T}} > 500$ MeV,
  - pseudorapidity $|\eta| < 2.5$,
  - at least 1 hit in the Pixel detector,
  - at least 6 hits in the SCT detector,
  - the transverse impact parameter d_0, calculated with respect to the LHC beam-axis, smaller than 1.5 mm,
  - the longitudinal impact parameter z_0, calculated withe respect to the primary vertex, multiplied by $\sin(\theta)$, smaller than 1.5 mm.

The signal selection for the MC samples is as for the data, except for the trigger and the LB (it is summarized in Appendix A.9) since the MC samples do not contain trigger information and the luminosity blocks are not defined. The proton transport to the AFP and reconstruction are implemented.

The contributions of particular processes to the signal sample for PYTHIA 8.2 are summarized in Table 5.3 for different ξ ranges. One can notice that the contribution of single-diffractive processes is the largest for the lowest value of ξ. Protons in double-diffractive and non-diffractive

Table 5.3: Fraction of the accepted SD, DD and ND processes in the PYTHIA 8.2 generated sample.

	$\xi \in \langle 0.035; 0.080\rangle$	$\xi \in \langle 0.035; 0.050)$	$\xi \in \langle 0.050; 0.065\rangle$	$\xi \in (0.065; 0.080\rangle$
SD	90.8 %	93.9 %	90.6 %	86.3 %
DD	5.4 %	3.8 %	5.7 %	7.7 %
ND	3.8 %	2.3 %	3.7 %	6.0 %

processes are not the intact ones – they are due to hadronization. According to PYTHIA 8.2, the amount of events with a proton resulting from hadronization is growing with the increasing proton ξ (see Fig. 5.9).

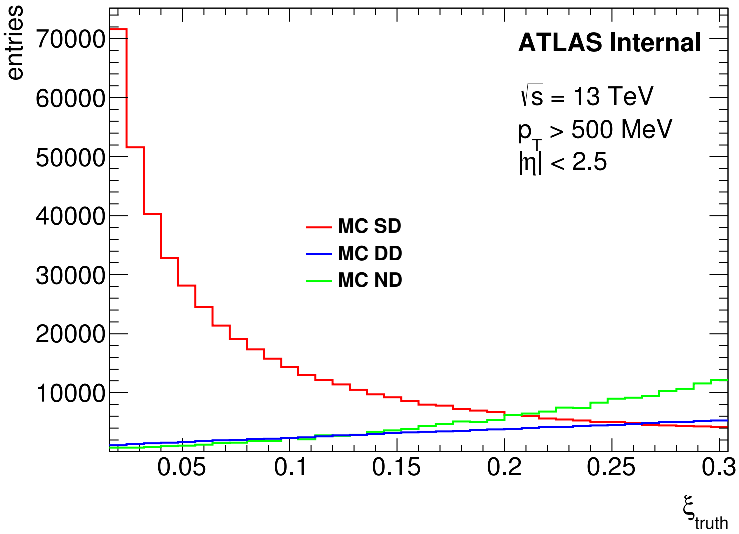

Figure 5.9: PYTHIA 8.2 simulation: number of single-diffractive (red line), double-diffractive (blue line) and non-diffractive (green line) events in the signal sample as a function of ξ of the truth proton, ξ_{truth}. Protons in double-diffractive and non-diffractive interactions result from hadronization.

5.4 Initial distributions of track observables

After applying the full selection criteria, the distributions of the track multiplicity, the track p_{T} and η were obtained both for the data and MC. The track multiplicity distributions (see Fig. 5.10) for the data and MC samples have different shapes – PYTHIA 8.2 predicts higher average multiplicities than observed in the data whilst EPOS much lower average multiplicities. One can notice almost lack of events for $n_{\text{trk}} > 26$ for EPOS sample. It is due to the fact that in the diffraction model implemented in EPOS the low multiplicities are much more populated than the higher ones. A very large sample would have to be generated to increase statistics for higher multiplicitis which was not of the crucial importance in this analysis.

The disagreement of the shapes is observed also for the transverse momentum distributions (see Fig. 5.11(a)). EPOS clearly underestimates the data for $p_{\text{T}} > 1$ GeV while PYTHIA 8.2 fairly well describes the shape of the experimental distribution.

A large discrepancy is visible in case of the pseudorapidity distributions as well (see Fig. 5.11(b)). The data distribution shows a clear left-right asymmetry. As already mentioned, a proton was reconstructed on the side with a negative values of η. PYTHIA 8.2 predictions show a very small asymmetry while EPOS predicts symmetrical η distribution.

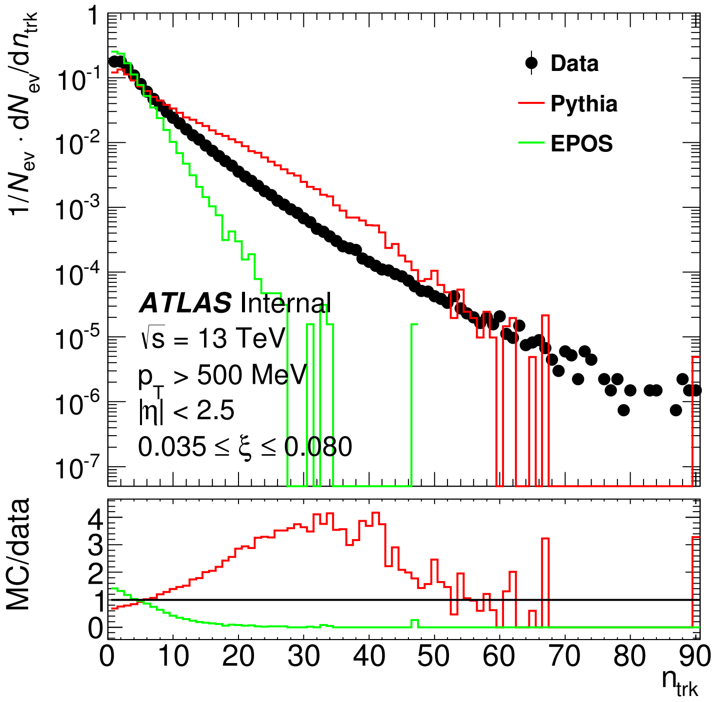

Figure 5.10: The normalized track multiplicity distribution. The black dots represent data, the red and green lines correspond to PYTHIA and EPOS, respectively.

Figs. 5.12, 5.13(a) and 5.13(b) present distributions of n_{trk}, p_{T} and η, respectively, for different ranges of the registered proton ξ. One can notice that there are no dramatic differences in the shapes of the distributions. However, for the highest values of ξ (blue curves) higher track multiplicities are slightly more populated (see Fig. 5.12), there is also a bit more tracks with higher transverse momentum (see Fig. 5.13(a)) and the negative values of pseudorapidity are more occupied (see Fig. 5.13(b)).

Distributions presented in this section were calculated for the tracks at the detector level, both for the data and MC. However, if one intends to compare these results with the results measured for instance by another experiment, they have to be off the detector effects. This implies that all the corrections related to the detector performance have to be implemented.

Another issue is the background, which in this analysis is related to pile-up (see Chapter 7) as few interactions occuring at the same time may be in some cases misidentified as only one interaction having the signal signature. This kind of a background is irreducible, which means that it is not possible to remove background events from the data sample during the selection. The way to deal with this background is to estimate distributions of particular variables for the background and then to subtract them statistically from the distributions for the preselected data sample.

Summarizing, the results already presented at the level of the tracks have to be corrected

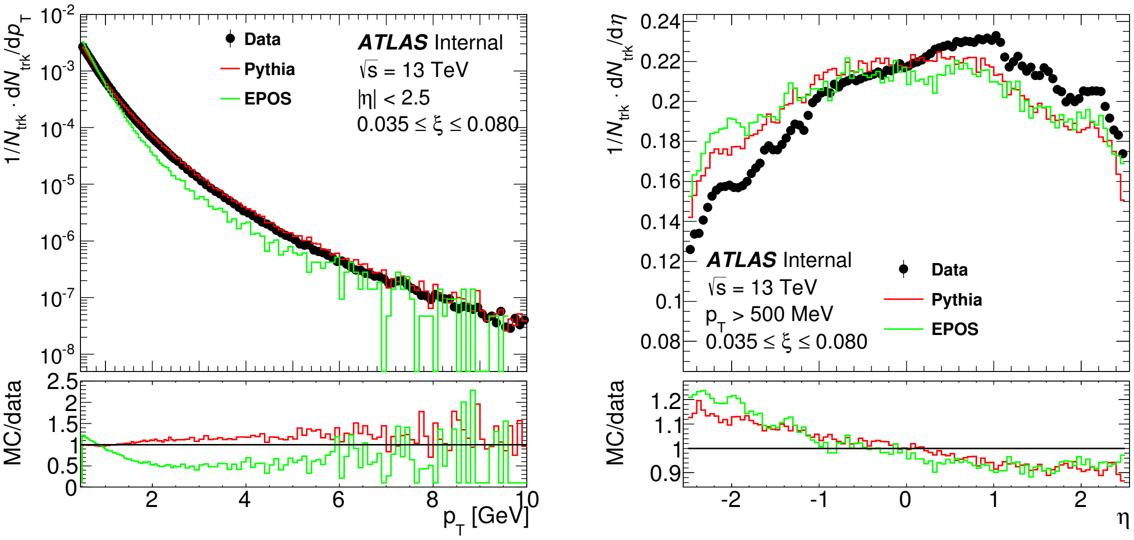

(a)

(b)

Figure 5.11: The normalized (a) transverse momentum, (b) pseudorapidity distributions of charged tracks. The black dots represent the data, the red and green lines correspond to PYTHIA 8.2 and EPOS predictions, respectively. The reconstructed proton had a negative value of η.

to the particle level, which involves both application of the corrections for the detector effects and the background subtraction. Otherwise, a comparison of the MC to the data may not be meaningful.

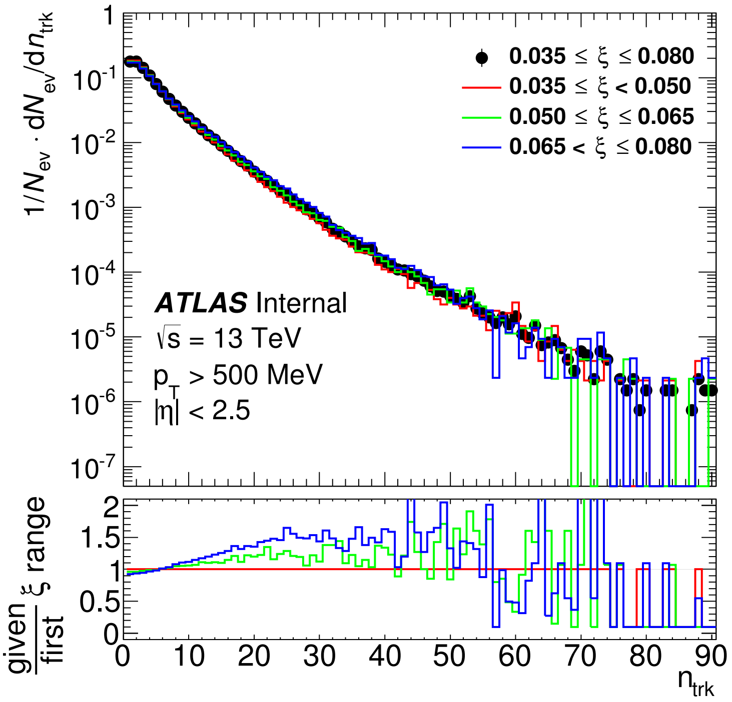

Figure 5.12: The normalized multiplicity distributions of charged tracks for different ranges of the proton ξ: black dots – whole range of ξ, colorful lines – narrower ranges of ξ.

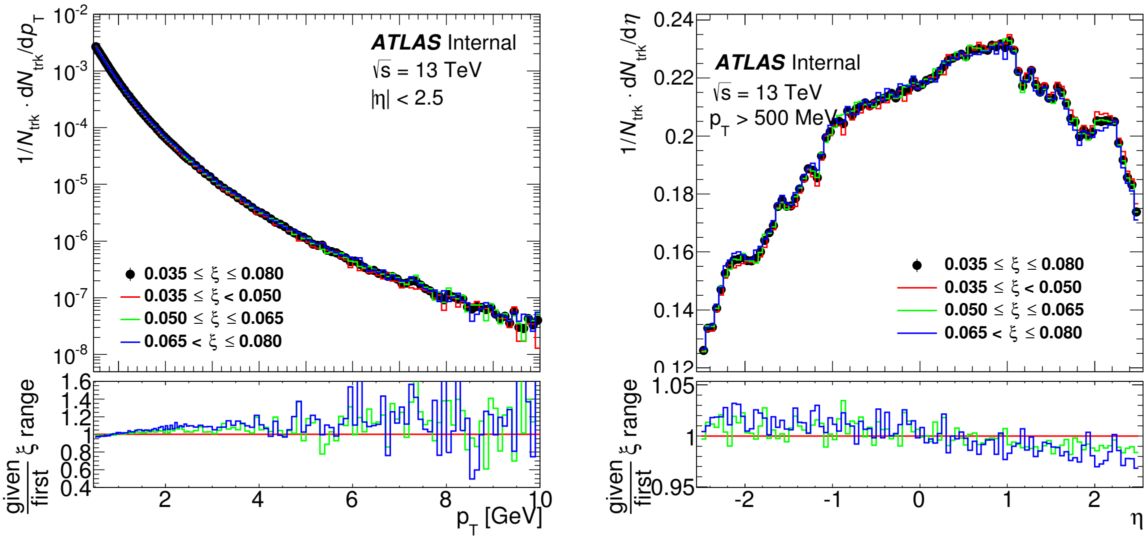

(a)

(b)

Figure 5.13: The normalized (a) transverse momentum, (b) pseudorapidity distributions of charged tracks for different ranges of the proton ξ: black dots – whole range of ξ, colorful lines – narrower ranges of ξ.

CHAPTER 6

THE INNER DETECTOR RELATED EFFICIENCIES

In this chapter the correction procedure related to the track and vertex reconstruction efficiences is described. These corrections are applied to the data sample before the background subtraction.

6.1 Vertex reconstruction efficiency

In some events it may happen that an interaction took place and particles where produced, but no interaction vertex was reconstructed.

The vertex reconstruction efficiency is calculated using the data sample and follows the procedure described in [14]. The selection criteria for events taken to its estimation follow the signal sample selection, except for the vertex presence requirement and hence besides the requirement on $z_0 \sin(\theta)$ for tracks. The multiplicity of selected tracks with relaxed selection is denoted as $n_{\mathrm{sel}}^{\mathrm{vtx}}$. Then the vertex reconstruction efficiency is calculated as:

$$\varepsilon_{\mathrm{vtx}}\left(n_{\mathrm{sel}}^{\mathrm{vtx}}\right) = \frac{\text{number of events with } n_{\mathrm{sel}}^{\mathrm{vtx}} \text{ tracks and with exactly one reconstructed vertex}}{\text{number of events with } n_{\mathrm{sel}}^{\mathrm{vtx}} \text{ tracks with no or one reconstructed vertex}}\,. \tag{6.1}$$

The vertex reconstruction efficiency $\varepsilon_{\mathrm{vtx}}$ as a function of $n_{\mathrm{sel}}^{\mathrm{vtx}}$ is presented in Fig. 6.1. For $n_{\mathrm{sel}}^{\mathrm{vtx}} = 1$ the vertex reconstruction efficiency is significantly lower than for events with higher multiplicities. Moreover, the efficiency dependence on the pseudorapidity of a single track, $\varepsilon_{\mathrm{vtx}}\left(n_{\mathrm{sel}}^{\mathrm{vtx}} = 1, \eta\right)$, can not be neglected (see Fig. 6.2). One can notice that this efficiency is asymmetric. It is related to the fact that the η distribution for the tracks in the selected sample is asymmetric, with more particles produced at $\eta > 0$. The vertex reconstruction algorithm requirements for the tracks are less restrictive than the above (see Section 4.2) thus more tracks than $n_{\mathrm{sel}}^{\mathrm{vtx}}$ could have been taken into account during the vertex reconstruction procedure. Higher number of tracks reconstructed in the ID at $\eta > 0$ favors the vertex reconstruction in that kinematic region.

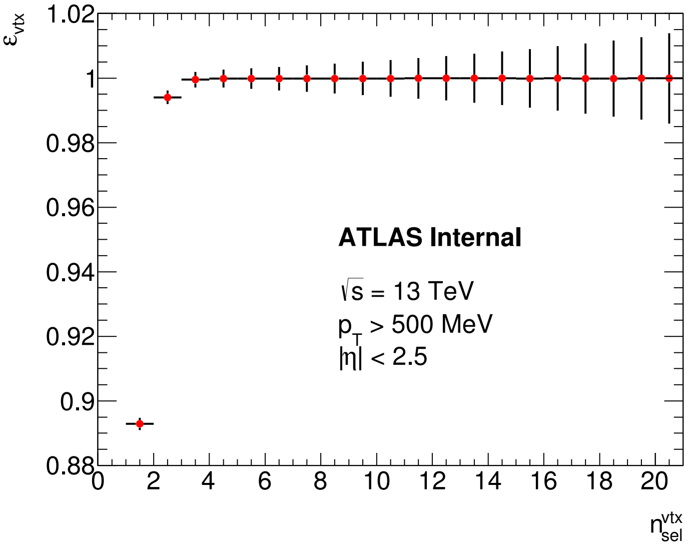

Figure 6.1: The vertex reconstruction efficiency as a function of $n_{\text{sel}}^{\text{vtx}}$.

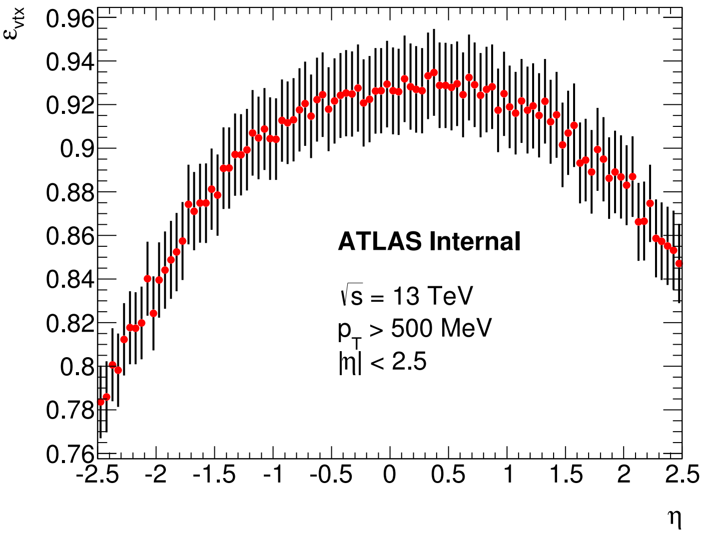

Figure 6.2: The vertex reconstruction efficiency for events with $n_{\text{sel}}^{\text{vtx}} = 1$ as a function of η.

Finally, the effect of event losts due to the vertex requirements is corrected by an event-by-event weight:

$$w\left(n_{\text{trk}}, \eta\right) = \frac{1}{\varepsilon_{\text{vtx}}\left(n_{\text{sel}}^{\text{vtx}}, \eta\right)}. \tag{6.2}$$

6.2 Track reconstruction efficiency

The reconstruction probability of a track due to a charged particle hitting the ID depends on the region of the ID the particle was travelling through. As physics processes and the ID are symmetric in the angle φ, the angular dependence can be expressed only in terms of a θ angle that will be further represented in terms of a particle η. The reconstruction probability depends also on the depth of the detector that a particle was penetrating through, hence on the p_{T} of the particle. That probability is called an efficiency of the track reconstruction. The track reconstruction efficiency is calculated using MC and following [14]. It is defined as:

$$\varepsilon_{\mathrm{trk}}\left(\eta, p_{\mathrm{T}}\right) = \frac{N_{\mathrm{reco}}^{\mathrm{matched}}\left(\eta, p_{\mathrm{T}}\right)}{N_{\mathrm{gen}}\left(\eta, p_{\mathrm{T}}\right)} \tag{6.3}$$

where η and p_{T} are the true kinematic variables of a generated particle, $N_{\mathrm{reco}}^{\mathrm{matched}}$ is the number of the reconstructed tracks matched to particles generated in the given $\left(\eta, p_{\mathrm{T}}\right)$ bin, whereas N_{gen} is the number of generated charged particles in the same $\left(\eta, p_{\mathrm{T}}\right)$ bin. The track reconstruction efficiency is determined using those MC events which passed the signal selection criteria. Matching of a reconstructed track to a true charged particle is performed applying the weighted matching probability P_{match} (see [14]), defined as:

$$P_{\mathrm{match}} = \frac{10 \cdot N_{\mathrm{Pixel}}^{\mathrm{common}} + 5 \cdot N_{\mathrm{SCT}}^{\mathrm{common}} + 1 \cdot N_{\mathrm{TRT}}^{\mathrm{common}}}{10 \cdot N_{\mathrm{Pixel}}^{\mathrm{track}} + 5 \cdot N_{\mathrm{SCT}}^{\mathrm{track}} + 1 \cdot N_{\mathrm{TRT}}^{\mathrm{track}}} \tag{6.4}$$

where $N_{\mathrm{detector}}^{\mathrm{common}}$ is the number of hits which are common to a given track and the corresponding true particle, while $N_{\mathrm{detector}}^{\mathrm{track}}$ is the number of hits which form the track. The track is matched to the true particle if $P_{\mathrm{match}} > 0.5$.

The obtained track reconstruction efficiency $\varepsilon_{\mathrm{trk}}\left(\eta, p_{\mathrm{T}}\right)$ is presented in Fig. 6.3. Its projections $\int \varepsilon_{\mathrm{trk}}\left(\eta, p_{\mathrm{T}}\right) dp_{\mathrm{T}}$ and $\int \varepsilon_{\mathrm{trk}}\left(\eta, p_{\mathrm{T}}\right) d\eta$ are presented in Figs. 6.4(a) and 6.4(b), respectively. The track reconstruction efficiency as a function of η is approximately constant and on average close to 85% for $|\eta| < 1$. For $|\eta| > 1$ one can observe a decrease of $\varepsilon_{\mathrm{trk}}\left(\eta\right)$ related to the increasing amount of the detector material in a particle path. Local maxima at $|\eta| \approx 2$ are associated with a large number of sensitive detector layers in the end-cap region that particles are passing through [14]. As can be observed, the track reconstruction efficiency practically does not depend on p_{T} and is on average close to 80%. Only for $p_{\mathrm{T}} < 1$ GeV it drops showing a threshold behaviour.

To correct for inefficiencies in the track reconstruction, the p_{T} and η distributions of the selected tracks are corrected for with a track-by-track weight:

$$w\left(p_{\mathrm{T}}, \eta\right) = \frac{1}{\varepsilon_{\mathrm{trk}}\left(\eta, p_{\mathrm{T}}\right)}. \tag{6.5}$$

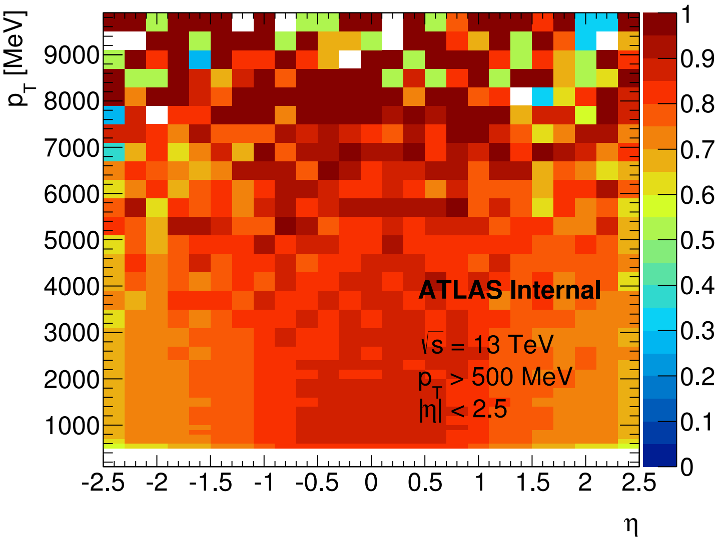

Figure 6.3: The track reconstruction efficiency as a function of p_{T} and η.

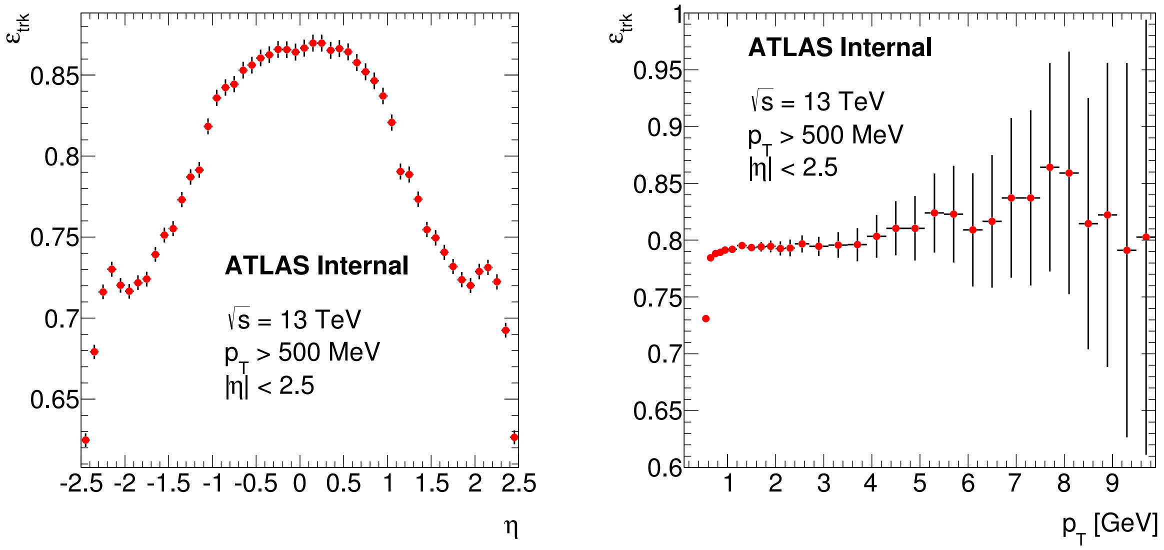

(a)

(b)

Figure 6.4: The track reconstruction efficiency as a function of (a) η, (b) p_{T}.

CHAPTER 7

COMBINATORIAL BACKGROUND

In the analysis performed within this dissertation the signal is defined as a process in which exactly one interaction occurred, resulting in an experimental signature of a diffractively scattered proton reconstructed in the AFP detector and a primary vertex reconstructed in the ID with at least one charged particle track associated with it. A sketch of the signal process is presented in Fig. 7.1.

Figure 7.1: Scheme of the signal process. The solid black dot represents the reconstructed vertex and the thick blue line a track reconstructed in the AFP.

Such a signature can be also due to a background event. A combinatorial background event is defined as an event in which within one bunch crossing there is a coincidence of two interactions, one providing a proton in the AFP and the second one delivering the reconstructed vertex. Such an event has the same signature as the signal event as is schematically presented in Fig. 7.2. A group of processes leading only to a reconstructed proton in the AFP is presented in Fig. 7.3.

(a) First of them is the halo process, where some particle reaches the AFP detector accidentally. The proton beams are surrounded by stray particles (so-called beam halo) which emmerge as a result of interactions of beam particles with collimation instrumentation or with residual gas in the vacuum chambers. These effects are coherent with the beam.

(b) Another possibility is a situation where a diffractive proton–proton interaction took place

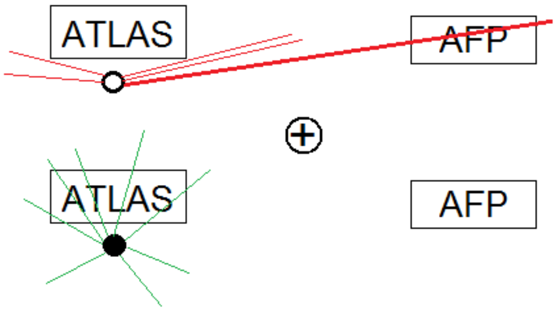

Figure 7.2: Scheme of the combinatorial background process where first interaction (the upper part of the figure) results in a proton in the AFP and the second interaction (the lower part of the figure) provides a reconstructed vertex. The hollow black dot on the upper part represents a lack of the reconstructed vertex.

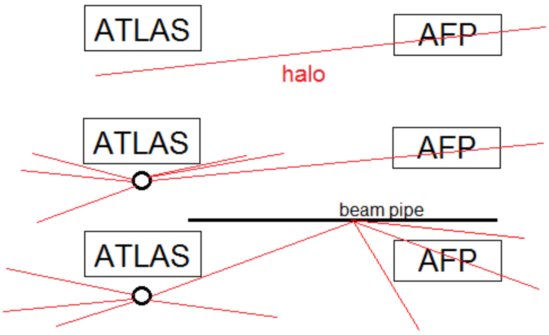

Figure 7.3: Scheme of processes providing only a particle reconstructed in the AFP. Top: beam halo process; middle: vertex not reconstructed in the ID; bottom: particle shower induced on the beam pipe close to the AFP.

and an intact proton reached the AFP but the interaction vertex was not reconstructed. In most cases a lack of the ID reconstructed vertex is related to the lack of tracks fulfilling the vertex reconstruction procedure criteria. However, sometimes the vertex reconstruction algorithm fails and a primary vertex is not reconstructed even though the ID tracks pass all the requirements.

(c) The last kind of processes is an interaction with a lack of reconstructed primary vertex in which some particle hits the beam pipe close to the AFP detector resulting in a creation of a shower. Shower particles may reach the AFP.

7.1 Statistical model

To estimate the combinatorial background contribution a statistical model was devised. This model considers only two signatures:

- reconstructed AFP proton,
- reconstructed primary interaction vertex.

These signatures are disjoint. Since it is impossible to register an event which is vertex- and AFP proton-less then there are only three classes of potential processes (see Fig. 7.4). They are characterized by:

- a reconstructed primary vertex and a lack of the AFP proton, denoted as “vtx”,
- a reconstructed primary vertex and the AFP proton, denoted as “p,vtx”,
- a lack of a reconstructed primary vertex and the AFP proton, denoted as “p”.

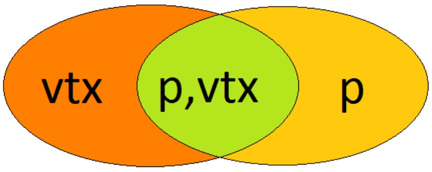

Figure 7.4: The statistical model classes.

A corresponding probability of occurence of a process is associated with each of these classes: p_{vtx}, $p_{\mathrm{p,vtx}}$ and p_{p}, respectively. These three probabilities are parameters of the discussed model. The fourth parameter of the model is μ – the mean number of pp interactions per bunch crossing.

As the three defined processes are a complete sample space, then:

$$p_{\mathrm{vtx}} + p_{\mathrm{p,vtx}} + p_{\mathrm{p}} = 1\,. \tag{7.1}$$

The probability distribution of the number of processes, n_{tot}, occuring in an event (bunch crossing) with the mean number of processes per bunch crossing equal to μ is given by Poisson distribution:

$$P\left(n_{\mathrm{tot}}, \mu\right) = e^{-\mu} \cdot \frac{\mu^{n_{\mathrm{tot}}}}{n_{\mathrm{tot}}!}\,, \tag{7.2}$$

with μ:

$$\mu = \mu_{\mathrm{vtx}} + \mu_{\mathrm{p,vtx}} + \mu_{\mathrm{p}}\,, \tag{7.3}$$

where μ_{vtx}, $\mu_{\mathrm{p,vtx}}$ and μ_{p} denote the mean numbers of processes per bunch crossing for the three defined classes and are given by:

$$\mu_\alpha = \mu \cdot p_\alpha\,, \tag{7.4}$$

where α denotes the process type.

7.2 The statistical model parameters

At first, one has to consider few possible scenarios that can be described by the statistical model and write down the equations representing their probabilities. These probabilities are constructed as combinations of the probabilities of particular processes. The scenarios are based on the observation of events with different signatures which include the AFP information and the number of reconstructed primary vertices. As a result, one gets a set of four non-linear equations.

In accordance with the adopted convention, the equations describing probability $P\left(n_{\text{vtx}},\text{AFP}\right)$ of observing an event with n_{vtx} reconstructed primary vertices and with AFP proton may be written as:

$$P\left(n_{\text{vtx}}=0,\text{AFP}\right)=P\left(n_{\text{tot}}=1,\mu\right)\cdot p_{\text{p}}\,, \tag{7.5}$$

$$P\left(n_{\text{vtx}}=1,\text{AFP}\right)=P\left(n_{\text{tot}}=1,\mu\right)p_{\text{p,vtx}}+P\left(n_{\text{tot}}=2,\mu\right)\binom{2}{1}p_{\text{vtx}}\binom{1}{1}p_{\text{p}}\,, \tag{7.6}$$

$$P\left(n_{\text{vtx}}=2,\text{AFP}\right)=P\left(n_{\text{tot}}=2,\mu\right)\binom{2}{1}p_{\text{vtx}}\binom{1}{1}p_{\text{p,vtx}}+P\left(n_{\text{tot}}=3,\mu\right)\binom{3}{2}p_{\text{vtx}}^{2}\binom{1}{1}p_{\text{p}}\,. \tag{7.7}$$

For instance, observation of an event with one reconstructed primary vertex and a proton in the AFP (see Eq. (7.6)) is possible when there was exactly one process providing both the reconstructed primary vertex and the AFP proton. Another possibility is that there happened two processes: one giving the reconstructed primary vertex and the other one the AFP proton.

Substituting (7.2) and $p_{\text{p,vtx}}=1-p_{\text{p}}-p_{\text{vtx}}$ into (7.5) - (7.7) one gets:

$$P\left(0\text{vtx},\text{AFP}\right)=e^{-\mu}\mu\cdot p_{\text{p}}\,, \tag{7.8}$$

$$P\left(1\text{vtx},\text{AFP}\right)=e^{-\mu}\mu\cdot\left(1-p_{\text{p}}-p_{\text{vtx}}\right)+e^{-\mu}\mu^{2}\cdot p_{\text{vtx}}\cdot p_{\text{p}}\,, \tag{7.9}$$

$$P\left(2\text{vtx},\text{AFP}\right)=e^{-\mu}\mu^{2}\cdot p_{\text{vtx}}\cdot\left(1-p_{\text{p}}-p_{\text{vtx}}\right)+\frac{1}{2}e^{-\mu}\mu^{3}\cdot p_{\text{vtx}}^{2}\cdot p_{\text{p}}\,. \tag{7.10}$$

Left hand-sides of Eqs. (7.8) - (7.10) are measured using data. For that purpose a selection slightly modified with respect to the signal sample selection is used (see Appendix A.2). Namely, the number of reconstructed primary vertices was requested to be 0, 1 or 2.

Probabilities $P\left(n_{\text{vtx}},\text{AFP}\right)$ are calculated separately for every BCID as a fraction of events with n_{vtx} reconstructed vertices and having the AFP proton, $N\left(n_{\text{vtx}},\text{AFP}\right)$, to all events, N_{tot}, in a given bunch crossing within the same time period, t (which is the duration of the selected range of luminosity blocks):

$$P\left(n_{\text{vtx}},\text{AFP}\right)=\frac{\text{AFP\_prescale}\cdot N\left(n_{\text{vtx}},\text{AFP}\right)}{N_{\text{tot}}}\,, \tag{7.11}$$

where N_{tot} is given as:

$$N_{\text{tot}}=f_{\text{rev}}\cdot t\,. \tag{7.12}$$

7.2.1 Parameter μ

Two methods using the data were devised to extract the μ parameter. First method uses information which is stored within the data sample for each BCID and is obtained using the MBTS detector-based off-line `OR` algorithm [51]: the so-called *primary-vertex event counting*, where the event and track selection and the vertex reconstruction requirements are the following:

- an event passed the L1 MBTS single-arm trigger,
- a reconstructed primary vertex is required that is formed from at least two tracks, each with $p_{\mathrm{T}} > 100$ MeV,
- the tracks are required to fulfill the following quality requirements:
  - $|d_0| < 4$ mm,
  - $\sigma(d_0) < 5$ mm,
  - $\sigma(z_0) < 10$ mm,
  - at least 4 hits in the SCT detector,
  - at least 6 hits in the Pixel and SCT detectors in total.

The parameter μ_{MB} is introduced, where “MB" is an acronym from “Minimum Bias”. It is defined as the number of visible (i.e. passing the selection criteria) inelastic interactions per bunch crossing. It is calculated in a given time period from the occuring number of bunch crossings, N_{OR}, in which at least one pp interaction satisfied the event selection criteria and from the total number of bunch crossings, N_{BC}.

Following (7.2), the probability of observing at least one event can be expressed as:

$$P\left(N_{\mathrm{ev}} \geq 1, \mu_{\mathrm{MB}}\right) = 1 - P\left(N_{\mathrm{ev}} = 0, \mu_{\mathrm{MB}}\right) = 1 - e^{-\mu_{\mathrm{MB}}} = \frac{N_{\mathrm{OR}}}{N_{\mathrm{BC}}}, \tag{7.13}$$

where N_{ev} is the number of observed events. Solving (7.13) for μ_{MB}, one gets:

$$\mu_{\mathrm{MB}} = -\ln\left(1 - \frac{N_{\mathrm{OR}}}{N_{\mathrm{BC}}}\right). \tag{7.14}$$

An alternative method of computing parameter μ_{MB} exploits a fit to the distribution of the number of reconstructed primary vertices – for that purpose data sample triggered by the MBTS is used (sample selection summarized in Appendix A.3). The trigger requires at least two hits in MBTS and will be further denoted as “MBTS trigger”; this trigger prescale is 1500 in the analyzed data. For every BCID a fit of formula:

$$P\left(n_{\mathrm{vtx}}, \mu_{\mathrm{MB}}\right) = e^{-\mu_{\mathrm{MB}}} \cdot \frac{\mu_{\mathrm{MB}}^{n_{\mathrm{vtx}}}}{n_{\mathrm{vtx!}}} \tag{7.15}$$

to the n_{vtx} distribution is performed, starting from $n_{\mathrm{vtx}} = 1$. Even though these distributions contain a point corresponding to the absence of reconstructed primary vertices ($n_{\mathrm{vtx}} = 0$), this

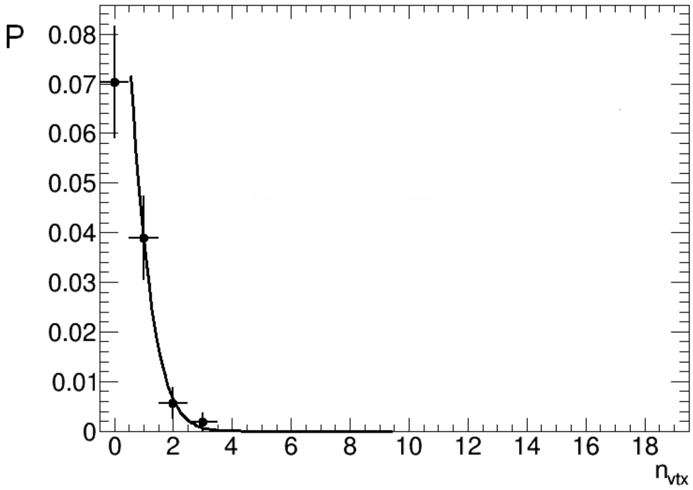

Figure 7.5: Distribution of the number of reconstructed primary vertices for a randomly chosen BCID.

point cannot be used in the fit as the majority of events without a reconstructed primary vertex do not trigger the MBTS. As a result, one gets a value of μ_{MB} for every BCID.

Figure 7.6 presents parameter μ_{MB} and its uncertainty, $\sigma(\mu_{\mathrm{MB}})$, as a function of BCID, calculated using both described methods. Uncertainties in Fig. 7.6(a) are very small and thus not visible. Horizontal axes do not correspond directly to the LHC BCID – only the BCIDs matching the colliding bunches were chosen and they were renumbered afterwards – for a distinction axes are titled as “bcid”. Both methods deliver comparable values of the parameter μ_{MB}. The first one

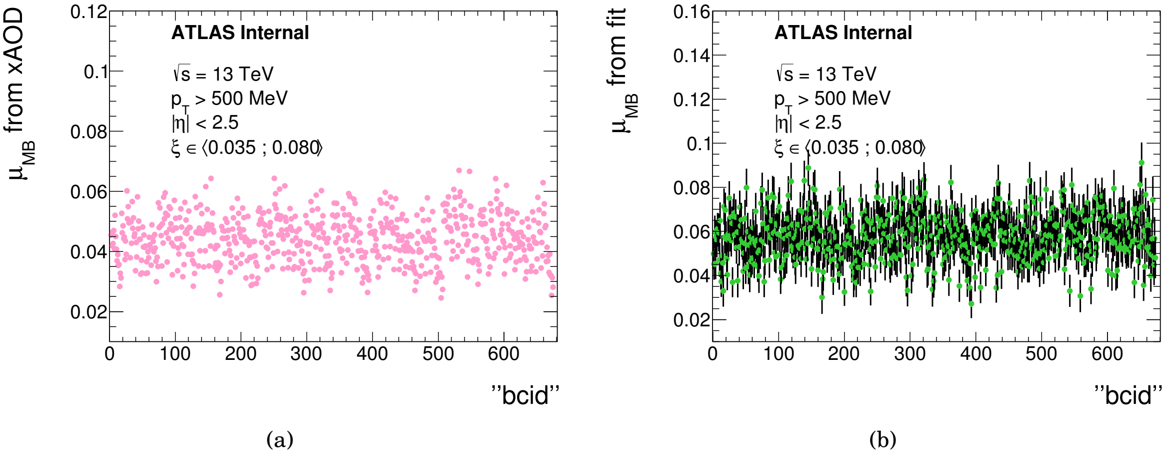

Figure 7.6: The μ_{MB} parameter obtained from (a) the information stored in the data, (b) the Poisson fit to the distribution of the number of the reconstructed primary vertices. Scale on horizontal axes represent renumbered BCIDs of colliding bunches.

was chosen as more reliable and the second one was used to estimate the systematic uncertainty.

It is worth stressing the difference between μ and μ_{MB}. As discussed previously, a process in general does not have to lead to a reconstructed primary vertex, so μ_{MB} is not equal to μ. According to the adopted convention, the formula linking μ and μ_{MB} is:

$$\mu_{\mathrm{MB}} = \mu \cdot \left(p_{\mathrm{vtx}} + p_{\mathrm{p,vtx}}\right), \tag{7.16}$$

what can be written as:

$$\mu_{\mathrm{MB}} = \mu \cdot \left(1 - p_{\mathrm{p}}\right). \tag{7.17}$$

Parameter μ_{MB} refers to the processes with the reconstructed primary vertex, hence the probability $P\left(n_{\mathrm{vtx}}, \mu_{\mathrm{MB}}\right)$ from (7.15) does not take into account processes which lead only to the reconstruction of the AFP proton. However, this formula does not exclude thesm either – their presence would not have changed the shape of the distribution presented in Fig. 7.5. Eqs. (7.5) - (7.7) contain a probability $P\left(n_{\mathrm{tot}}, \mu\right)$ depending on μ. According to (7.3), this probability includes all possible types of processes as:

$$\mu = \mu_{\mathrm{MB}} + \mu_{\mathrm{p}}. \tag{7.18}$$

For instance, $P\left(n_{\mathrm{tot}} = 1, \mu_{\mathrm{MB}}\right)$ is the probability that there was one interaction providing a reconstructed primary vertex; additionally, some other interaction not resulting in a reconstructed primary vertex could also occured. Probability $P\left(n_{\mathrm{tot}} = 1, \mu\right)$ extends the above, irrespectively of the presence of the reconstructed primary vertex.

7.2.2 Other parameters

Eqs. (7.8) - (7.10) and (7.17) have to be considered together as a set of four non-linear equations of three variables. This set of equations was solved numerically by the minimization of the χ^2 function, with help of ROOT `MINUIT` package [93], independently for each BCID. The χ^2 function was constructed as:

$$\chi^2 = \sum_{i=1}^{4} \mathrm{eq}_i^2, \tag{7.19}$$

where eq_i are given by:

$$\mathrm{eq}_1 = \frac{e^{-\mu}\mu \cdot p_{\mathrm{p}} - P\left(0\mathrm{vtx}, \mathrm{AFP}\right)}{\sigma\left[P\left(0\mathrm{vtx}, \mathrm{AFP}\right)\right]}, \tag{7.20}$$

$$\mathrm{eq}_2 = \frac{e^{-\mu}\mu \cdot \left(1 - p_{\mathrm{p}} - p_{\mathrm{vtx}}\right) + e^{-\mu}\mu^2 \cdot p_{\mathrm{vtx}} \cdot p_{\mathrm{p}} - P\left(1\mathrm{vtx}, \mathrm{AFP}\right)}{\sigma\left[P\left(1\mathrm{vtx}, \mathrm{AFP}\right)\right]}, \tag{7.21}$$

$$\mathrm{eq}_3 = \frac{e^{-\mu}\mu^2 \cdot p_{\mathrm{vtx}} \cdot \left(1 - p_{\mathrm{p}} - p_{\mathrm{vtx}}\right) + \frac{1}{2}e^{-\mu}\mu^3 \cdot p_{\mathrm{vtx}}^2 \cdot p_{\mathrm{p}} - P\left(2\mathrm{vtx}, \mathrm{AFP}\right)}{\sigma\left[P\left(2\mathrm{vtx}, \mathrm{AFP}\right)\right]}, \tag{7.22}$$

$$\mathrm{eq}_4 = \frac{\mu \cdot \left(1 - p_{\mathrm{p}}\right) - \mu_{\mathrm{MB}}}{\sigma\left(\mu_{\mathrm{MB}}\right)}. \tag{7.23}$$

The uncertainties on the denominators of Eqs. (7.20) - (7.22) are calculated as:

$$\sigma\left[P\left(n_{\mathrm{vtx}}, \mathrm{AFP}\right)\right] = \frac{\mathrm{AFP\_prescale}}{N_{\mathrm{tot}}} \cdot \sqrt{N\left(n_{\mathrm{vtx}}, \mathrm{AFP}\right)}. \tag{7.24}$$

As a result one gets parameters p_{vtx}, $p_{\mathrm{p,vtx}}$, p_{p}, μ and their uncertainties $\sigma\left(p_{\mathrm{vtx}}\right)$, $\sigma\left(p_{\mathrm{p,vtx}}\right)$, $\sigma\left(p_{\mathrm{p}}\right)$, $\sigma\left(\mu\right)$ for every BCID. Probabilities p_{vtx} and $p_{\mathrm{p,vtx}}$ are presented in Fig. 7.7. Figs. 7.8(a) and 7.8(b) show the obtained values of p_{p} and μ.

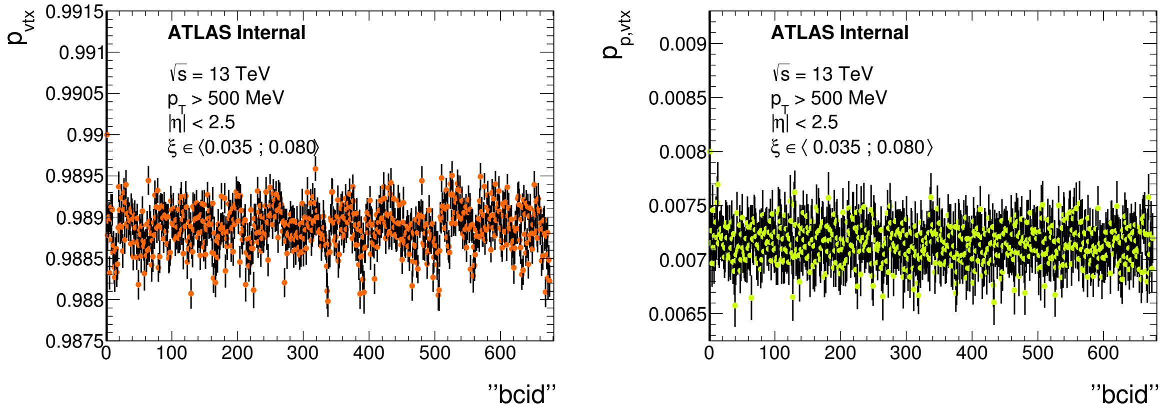

(a) (b)

Figure 7.7: The probability (a) p_{vtx}, (b) $p_{\mathrm{p,vtx}}$ as a function of renumbered BCID.

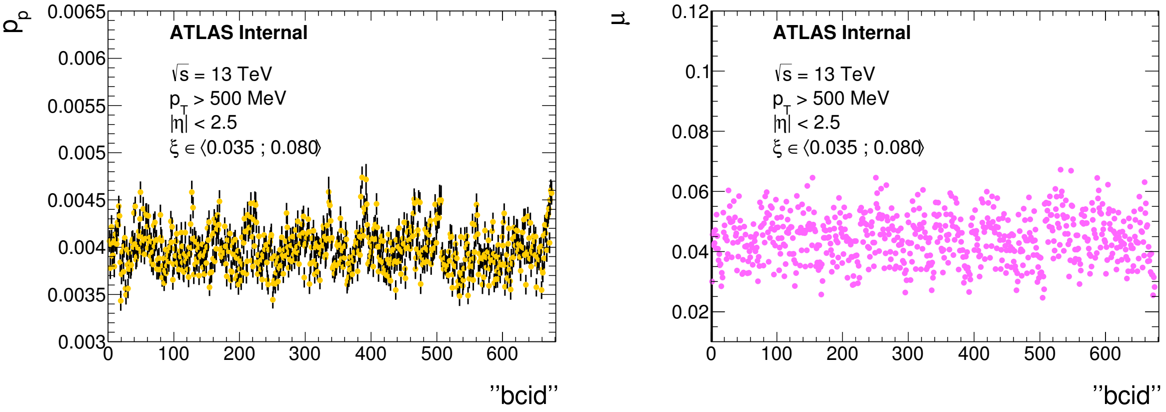

(a) (b)

Figure 7.8: (a) The probability p_{p} as a function of renumbered BCID. (b) The parameter μ as a function of renumbered BCID.

7.2.3 Evaluation of background contribution

To estimate the combinatorial background contribution one has to remember that this kind of background has the same signature as the signal. Formula (7.9) describing probability $P(\text{1vtx},\text{AFP})$ consists of two terms: the first term is the signal one and the second term is due to the combinatorial background. Therefore, the probability of registering a combinatorial background event, $P_{\text{bg}}(\text{1vtx},\text{AFP})$, can be calculated as:

$$P_{\text{bg}}(\text{1vtx},\text{AFP}) = e^{-\mu}\mu^2 \cdot p_{vtx} \cdot p_p \,. \tag{7.25}$$

The combinatorial background event is due to a coincidence of two interactions:

- an interaction with reconstructed primary vertex and without the AFP proton, which probability is given by $P(\text{1vtx},!\text{AFP})$,
- an interaction without a reconstructed primary vertex and with the AFP proton, which probability is given by $P(\text{0vtx},\text{AFP})$.

Since $P(\text{1vtx},!\text{AFP})$ can be expressed as:

$$P(\text{1vtx},!\text{AFP}) = P\left(n_{\text{tot}} = 1, \mu\right) \cdot p_{\text{vtx}} = e^{-\mu} \cdot \mu \cdot p_{\text{vtx}} \,, \tag{7.26}$$

then

$$P_{\text{bg}}(\text{1vtx},\text{AFP}) = P(\text{1vtx},!\text{AFP}) \cdot \mu \cdot p_p \,. \tag{7.27}$$

Transforming the probabilities into the numbers of events, the amount of the combinatorial background can be calculated as:

$$N_{\text{bg}}(\text{1vtx},\text{AFP}) = N(\text{1vtx},!\text{AFP}) \cdot \mu \cdot p_p \,. \tag{7.28}$$

The distributions obtained using the MBTS triggered data sample serve as the combinatorial background distributions. Event selection for the combinatorial background sample requires:

- the MBTS trigger fired,
- no proton on the AFP C side,
- range of the luminosity blocks the same as in the signal event selection,
- exactly one reconstructed primary vertex,
- at least one good ID track.

Then the multiplicity distribution of the combinatorial background can be computed as the sum of distributions obtained for various BCID:

$$N_{\mathrm{bg}}(n_{\mathrm{trk}}) = \sum_{\mathrm{BCID}} N_{\mathrm{MBTS}}(n_{\mathrm{trk}}, \mathrm{BCID}) \cdot \mu(\mathrm{BCID}) \cdot p_{\mathrm{p}}(\mathrm{BCID})\,. \tag{7.29}$$

The distributions $N_{\mathrm{MBTS}}(n_{\mathrm{trk}}, \mathrm{BCID})$ were multiplied by the MBTS prescale. Procedure of calculating the transverse momentum and pseudorapidity distributions and their systematic uncertainties for the combinatorial background is described in Section 7.4.

7.2.4 Systematic uncertainty

As the combinatorial background contribution depends on values of μ and p_{p}, their uncertainties were taken into account when estimating the uncertainty of this background. The uncertainty on the multiplicity distribution related to μ, $\Delta_{\mu}(n_{\mathrm{trk}})$, is given by:

$$\Delta_{\mu}(n_{\mathrm{trk}}) = \left| N_{\mathrm{bg}}\left(n_{\mathrm{trk}}, \mu^{\mathrm{default}}\right) - N_{\mathrm{bg}}\left(n_{\mathrm{trk}}, \mu^{\mathrm{fit}}\right) \right|, \tag{7.30}$$

where μ^{default} is calculated using the information stored in the data and μ^{fit} comes from the Poisson fit (see Section 7.2.1).

The uncertainty on the combinatorial background multiplicity distribution related to p_{p}, $\Delta_{p_{\mathrm{p}}}(n_{\mathrm{trk}})$, is given by:

$$\Delta_{p_{\mathrm{p}}}(n_{\mathrm{trk}}) = \left| N_{\mathrm{bg}}\left(n_{\mathrm{trk}}, p_{\mathrm{p}}\right) - N_{\mathrm{bg}}\left(n_{\mathrm{trk}}, p_{\mathrm{p}}^{\mathrm{max}}\right) \right|, \tag{7.31}$$

where $p_{\mathrm{p}}^{\mathrm{max}}$ is given as $p_{\mathrm{p}}^{\mathrm{max}} = p_{\mathrm{p}} + \sigma\left(p_{\mathrm{p}}\right)$. When calculating $N_{\mathrm{bg}}\left(n_{\mathrm{trk}}, p_{\mathrm{p}}\right)$, the parameter μ^{default} was used.

The final systematic uncertainty on the combinatorial background track multiplicity distribution related to the parameters of the statistical model, $\Delta_{\mathrm{model}}(n_{\mathrm{trk}})$, was calculated as:

$$\Delta_{\mathrm{model}}(n_{\mathrm{trk}}) = \sqrt{\Delta_{\mu}^{2}(n_{\mathrm{trk}}) + \Delta_{p_{\mathrm{p}}}^{2}(n_{\mathrm{trk}})}\,. \tag{7.32}$$

7.3 Correction for the MBTS trigger inefficiency

The MBTS triggered sample was used to determine the combinatorial background distributions. However, there are two effects involved which cause that the calculated track multiplicity distribution coming from the combinatorial background may be underestimated.

First one is related to the geometric acceptance of the MBTS detector. Especially for low multiplicities one can imagine a situation in which few particles are produced within the acceptance of the ID, but none of these particles reaches the MBTS. Such an event would be excluded and as a consequence the number of events with low track multiplicity will be underestimated. Second effect is related to the MBTS inefficiency itself. One of the reasons is aging of the MBTS related to the radiation dose accumulation.

These effects, causing the underestimation of the contribution of the combinatorial background, has to be taken into account. The default correction procedure is described below. Another two methods of calculating the MBTS inefficiency are described in detail in Appendices B.1 and B.2 – they were used for the estimation of the systematic uncertainty.

The default method to correct for the MBTS inefficiency exploits a minimum bias MC sample and the MBTS triggered data sample. It was previously shown [14] that the particle distributions of minimum bias data sample are described quite accurately by a mixture of SD, DD and ND processes generated in PYTHIA 8.2. The same feature was adopted to calculate a correction for the MBTS inefficiency. The data sample triggered by the MBTS with no requirement concerning a proton in the AFP and with exactly one reconstructed primary vertex and at least one good track was selected (see Appendix A.6).

Using the three above mentioned physical processes in PYTHIA 8.2, there was constructed the MC minimum bias sample. Selection criteria were the same as for the data (except for the trigger) Contributions of particular processes were found to be:

(a) single-diffractive: 19.54%,

(b) double-diffractive: 12.88%,

(c) non-diffractive: 67.58%.

Comparing the above contributions to those to the signal sample (listed in Table 5.3), here the non-diffractive processes constitute the majority of the sample.

It is expected that the track multiplicity distribution for minimum bias MC should overlap with the one for for the MBTS triggered data sample for higher values of multiplicity (in the range where the MBTS was efficient), i.e. their ratio should be close to one in this region.

The track multiplicity distribution for the minimum bias MC was normalized to the data by the following formula:

$$N_{\mathrm{MC}}(n_{\mathrm{trk}}) \to N_{\mathrm{MC}}(n_{\mathrm{trk}}) \cdot \frac{L_{\mathrm{int}} \cdot (\sigma_{\mathrm{SD}} + \sigma_{\mathrm{DD}} + \sigma_{\mathrm{ND}})}{N_{\mathrm{MC}}}, \tag{7.33}$$

where N_{MC} is the total number of events before selection in the merged minimum bias MC sample.

The track multiplicity distributions for the MBTS triggered data (multiplied by the trigger prescale) and the minimum bias MC sample and their ratio are shown in Fig. 7.9. One can see that the track multiplicity distributions differ, especially for the lowest multiplicities, where MC predicts more events than observed in the data. For multiplicities above 45 the minimum bias MC underestimates the data. As a result, the correction, G, presented in Fig. 7.9(b) takes values above one for the lowest multiplicities and values close to and below one for higher multiplicities. This effect does not influence the final results as the cut for the high track multiplicities will be introduced later on. In the data sample the contribution of the highest multiplicities can be overestimated due to the effect of merging of two interaction vertices into one and thus merging two events into one (see Chapter 8).

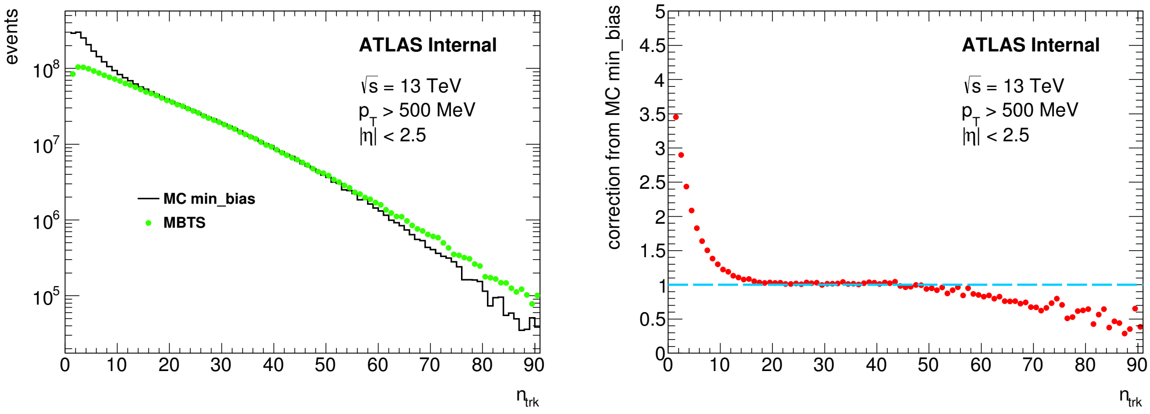

(a)

(b)

Figure 7.9: (a) The track multiplicity distributions for the MBTS triggered data sample (green dots) and for the minimum bias MC sample (black line). (b) The ratio of the minimum bias MC track multiplicity distribution and the track multiplicity distribution for the MBTS triggered data.

The combinatorial background track multiplicity distribution with the applied correction G together with the signal (before background subtraction) track multiplicity distribution are presented in Fig. 7.10. These distributions include the trigger prescales.

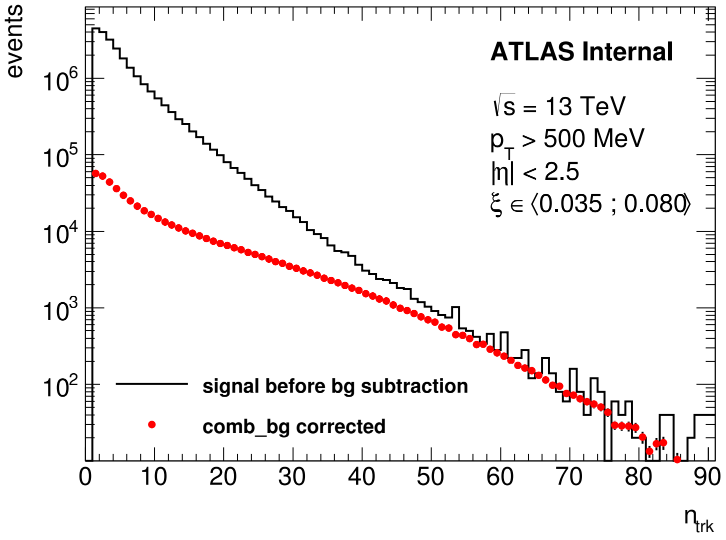

Figure 7.10: The track multiplicity distributions for the signal, before background subtraction (black line) and for the combinatorial background (red dots), with the default correction G applied.

The three corrections calculated for the MBTS inefficiency:

(A) G_{A}: using the minimum bias MC (this section),

(B) G_{B}: using the AFP_MBTS trigger (see Appendix B.1),

(C) G_{C}: using the calorimeter information (see Appendix B.2)

are shown in Fig. 7.11.

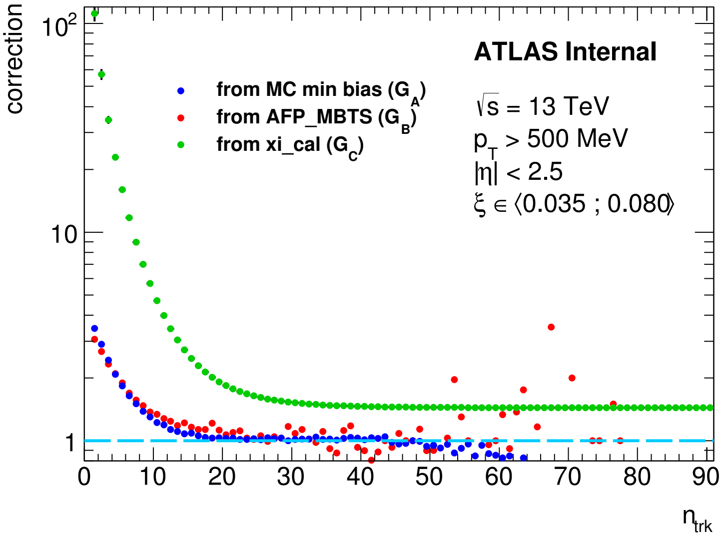

Figure 7.11: Corrections for the MBTS inefficiency calculated using different approaches. Blue curve: correction (A). Red curve: correction (B). Green curve: correction (C). Light blue dashed line corresponds to the value equal to 1.

The values of corrections G_{A} and G_{B} are similar. The correction G_{C} significantly differs from two other for the lowest multiplicities – it is many times larger. Explanation ot this discrepancy is presented in Section B.2. As previously stated, corrections G_{B} and G_{C} are used in the systematic uncertainty estimation.

7.4 Combinatorial background distributions

The track multiplicity distribution

The distributions of the track multiplicity for the data sample (before the background subtraction) and for the combinatorial background are presented in Fig. 7.12. Both distributions were divided by the number of events in the data sample. Systematic uncertainty on the combinatorial background is included – procedure of its estimation is described below.

Uncertainty

Two sources of the uncertainty are considered:

(a) uncertainty related to the statistical model parameters, μ and p_{p} (only these two influence the combinatorial background distribution),

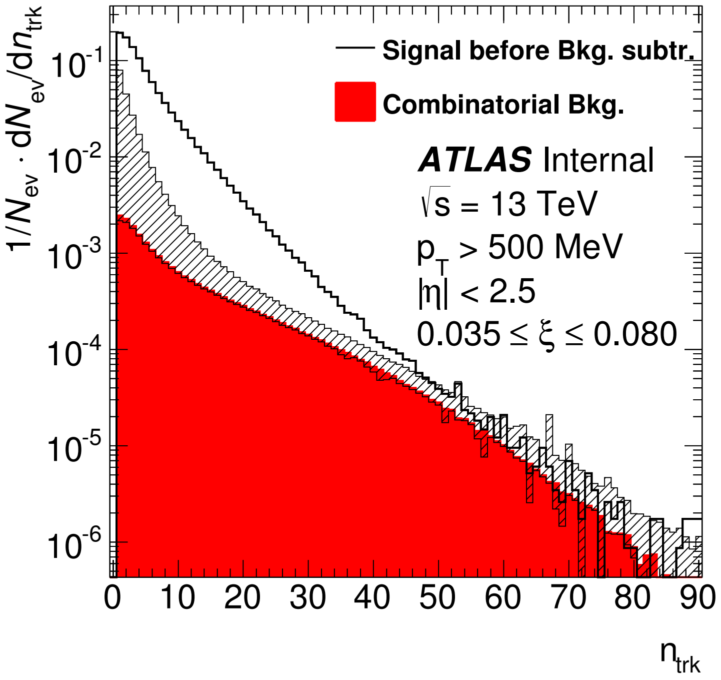

Figure 7.12: The normalized track multiplicity distributions: for the data sample before background subtraction (black line) and for the combinatorial background (red area). The dashed area corresponds to the systematic uncertainty of the combinatorial background distribution – procedure of its estimation is described in a paragraph “Uncertaintiy”.

(b) uncertainty related to the MBTS inefficiency.

The value of the uncertainty on the uncorrected combinatorial background track multiplicity distribution related to the parameters of the statistical model, $\Delta_{\mathrm{model}}(n_{\mathrm{trk}})$, was previously calculated in Section 7.2.4. Now it will be used in the estimation of the uncertainty on the distribution corrected for the MBTS inefficiency.

The uncertainty (b) comes from the differences between the combinatorial background track multiplicity distribution calculated using the default correction G_{A} and calculated using the remaining two corrections.

Five variants of the track multiplicity distributions for the combinatorial background were calculated:

$$\begin{cases} 1.\ N^{\mathrm{corr}}_{1,\mathrm{bg}}(n_{\mathrm{trk}}) = G_{\mathrm{A}}(n_{\mathrm{trk}}) \cdot N_{\mathrm{bg}}(n_{\mathrm{trk}}) \ - \text{ default variant}, \\ 2.\ N^{\mathrm{corr}}_{2,\mathrm{bg}}(n_{\mathrm{trk}}) = G_{\mathrm{B}}(n_{\mathrm{trk}}) \cdot N_{\mathrm{bg}}(n_{\mathrm{trk}}), \\ 3.\ N^{\mathrm{corr}}_{3,\mathrm{bg}}(n_{\mathrm{trk}}) = G_{\mathrm{C}}(n_{\mathrm{trk}}) \cdot N_{\mathrm{bg}}(n_{\mathrm{trk}}), \\ 4.\ N^{\mathrm{corr}}_{4,\mathrm{bg}}(n_{\mathrm{trk}}) = G_{\mathrm{A}}(n_{\mathrm{trk}}) \cdot \left[N_{\mathrm{bg}}(n_{\mathrm{trk}}) + \Delta_{\mathrm{model}}(n_{\mathrm{trk}})\right], \\ 5.\ N^{\mathrm{corr}}_{5,\mathrm{bg}}(n_{\mathrm{trk}}) = G_{\mathrm{A}}(n_{\mathrm{trk}}) \cdot \left[N_{\mathrm{bg}}(n_{\mathrm{trk}}) - \Delta_{\mathrm{model}}(n_{\mathrm{trk}})\right], \end{cases} \tag{7.34}$$

where $N_{\mathrm{bg}}(n_{\mathrm{trk}})$ is given by (7.29).

In the next step, each of these five variants was divided by the number of events in the signal sample. Then, the differences between the default distribution and the distributions in variants 2-5 were calculated (namely, one gets four differences) for each track multiplicity n_{trk}. Each sign differences were added in quadrature separately, resulting in asymmetric errors.

A contribution of the combinatorial background in the signal sample grows with increasing track multiplicity and for the $n_{\mathrm{trk}} \approx 50$ the signal sample is completely dominated by background. Fig. 7.13 presents the signal to background ratio plot. Fig. 7.13(a) shows this ratio for a whole n_{trk} range while Fig. 7.13(b) for a restricted range of $n_{\mathrm{trk}} \geq 30$ where the ratio starts to tend to 1. It was decided to consider the track multiplicity distribution only up to $n_{\mathrm{trk}} < 50$. Therefore, the transverse momentum and pseudorapidity distributions will be determined only for events with the track multiplicity lower than 50.

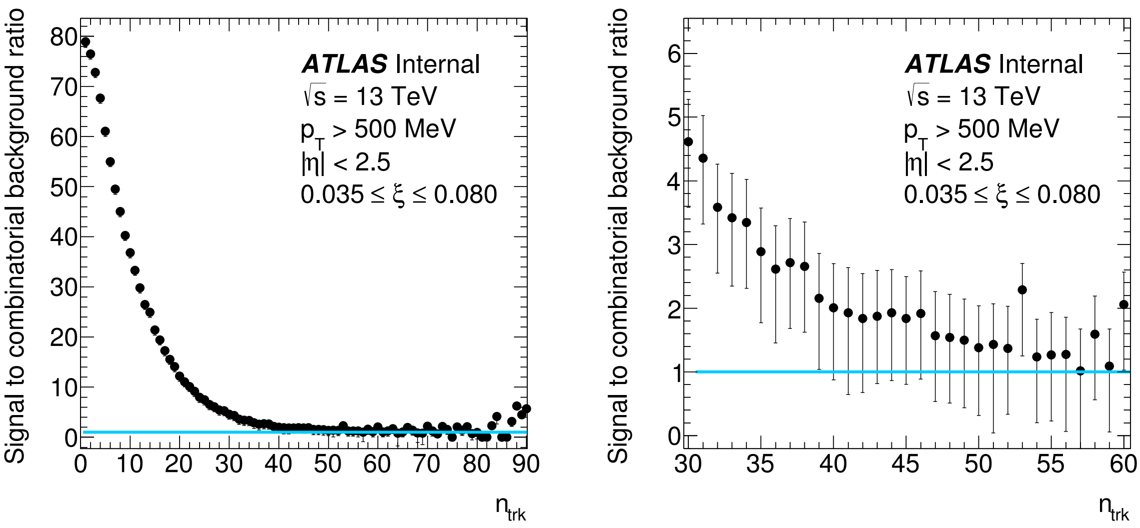

(a)

(b)

Figure 7.13: Ratio of the signal events before background subtraction to the combinatorial background events in the function of track multiplicity (black dots): (a) in the whole range of track multiplicities, (b) in the range of track multiplicites where the ratio starts to approach 1. Light blue dashed line correspond to the value equal to 1.

The transverse momentum distribution

This section describes the procedure valid for obtaining both the transverse momentum and pseudorapidity distributions for the combinatorial background. For sake of simplicity, the description considers only the p_{T} distribution.

To obtain the combinatorial background p_{T} distribution a procedure similar to that used in the case of the n_{trk} distribution was applied. Events from the MBTS triggered data fulfilling the combinatorial background selection were used. Additionally, only events with the track multiplicity lower than 50 were taken into account.

At the first stage, the transverse momentum distribution was constructed separately for each track multiplicity and BCID. Then, these distributions were multiplied by a corresponding factor $\mu(\mathrm{BCID}) \cdot p_{\mathrm{p}}(\mathrm{BCID})$ and eventually summed over BCID:

$$N_{\mathrm{bg}}(p_{\mathrm{T}}, n_{\mathrm{trk}}) = \sum_{\mathrm{BCID}} N_{\mathrm{MBTS}}(p_{\mathrm{T}}, \mathrm{BCID}, n_{\mathrm{trk}}) \cdot \mu(\mathrm{BCID}) \cdot p_{\mathrm{p}}(\mathrm{BCID})\,. \tag{7.35}$$

Next, the default MBTS correction factor $G_{\mathrm{A}}(n_{\mathrm{trk}})$ was applied to each distribution for a given n_{trk}. At the end, the p_{T} distributions for various track multiplicities were summed. A whole procedure is summarized by the following equation:

$$N_{\mathrm{bg}}^{\mathrm{corr}}(p_{\mathrm{T}}) = \sum_{n_{\mathrm{trk}}} \sum_{\mathrm{BCID}} N_{\mathrm{MBTS}}(p_{\mathrm{T}}, \mathrm{BCID}, n_{\mathrm{trk}}) \cdot \mu(\mathrm{BCID}) \cdot p_{\mathrm{p}}(\mathrm{BCID}) \cdot G_{\mathrm{A}}(n_{\mathrm{trk}})\,. \tag{7.36}$$

Uncertainty

The uncertainty on the combinatorial background transverse momentum distribution was estimated in a similar way to that for the track multiplicity. The goal was to get the analogous five variants of the p_{T} distribution. The simplest way to calculate them was to exploit the previously determined five variants of n_{trk} distribution given by (7.34), together with the one calculated directly from the statistical model and given by (7.29).

Each variant of (7.34) was divided by (7.29) – as a result one gets five distributions $H_i(n_{\mathrm{trk}})$, $i = 1,2,3,4,5$. Each of them tells by what function one should multiply the distribution obtained directly from the statistical model to get one of the five corrected variants. The corrected p_{T} distributions were determined using the functions $H_i(n_{\mathrm{trk}})$ as:

$$N_{i,\mathrm{bg}}^{\mathrm{corr}}(p_{\mathrm{T}}) = \sum_{n_{\mathrm{trk}}} N_{\mathrm{bg}}(p_{\mathrm{T}}, n_{\mathrm{trk}}) \cdot H_i(n_{\mathrm{trk}})\,. \tag{7.37}$$

Then the procedure of the p_{T} distribution uncertainty determination for the combinatorial background exactly follows the one for the track multiplicity.

The distributions of the transverse momentum for the data sample (before the background subtraction) and for the combinatorial background are presented in Fig. 7.14(a). The systematic uncertainty on the background distribution is included and marked by the dashed area.

Pseudorapidity distribution

The procedure of determination of the pseudorapidity distribution for the combinatorial background and its uncertainty is analogous to that used in case of the transverse momentum distribution.

The η distributions for the data sample (before the background subtraction) and for the combinatorial background are presented in Fig. 7.14(b). The systematic uncertainty on the background distribution is included and marked by the dashed area.

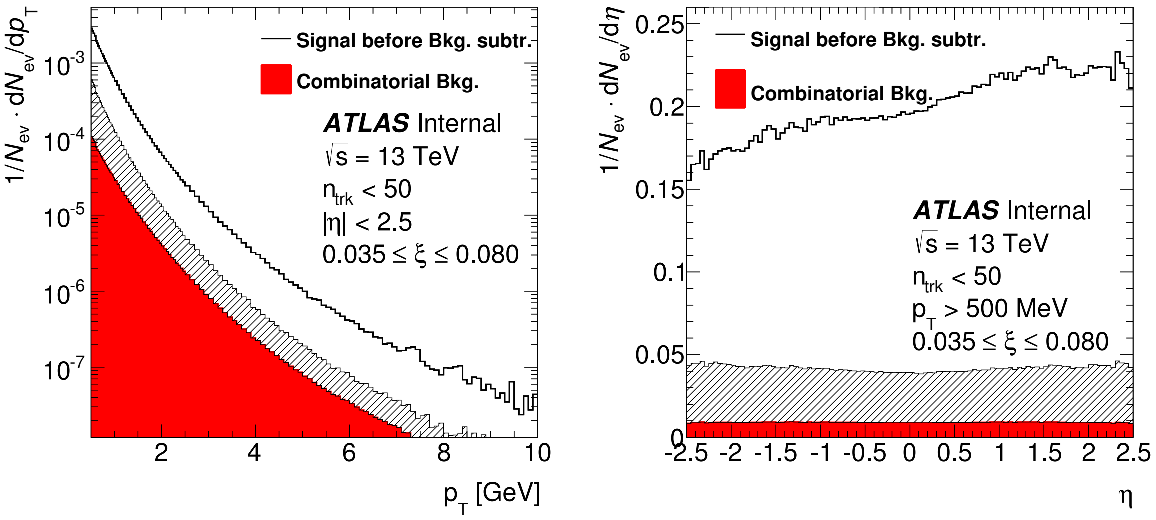

(a) (b)

Figure 7.14: The normalized (a) transverse momentum, (b) pseudorapidity distributions: for the combinatorial background (red area) and for the signal sample before background subtraction (black line). The dashed area corresponds to the systematic uncertainty of the combinatorial background distribution – the procedure of its calculation is described in paragraph “Uncertainty”.

CHAPTER 8

BACKGROUND RELATED TO THE VERTEX RECONSTRUCTION

The primary vertex reconstruction performance is not fully proficient when two or more interactions took place very closely to each other – illustration of such an event is presented in Fig. 8.1. As a consequence, a situation where the vertices may be merged into single one may take place.

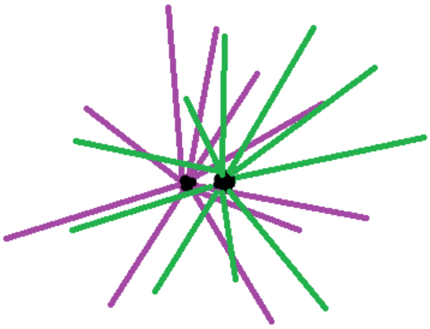

Figure 8.1: Two interactions occuring very close to each other may lead to the incorrect reconstruction of the primary vertices of the interactions.

To estimate the number of events of such a kind, a special set of events was selected. The requirements on the selected events are almost the same as for the signal sample with one modification: two reconstructed primary vertices per event were required. The sample selection is summarized in Appendix A.8.

Then, the distribution of the distance between the two vertices along the z axis, Δz, was constructed. It is shown in Fig. 8.2. One can observe a significant drop in the number of entries in the center of the distribution. This drop will be further denoted as a "well". Missing events can be expected as a migration to the sample wit only one reconstructed primary vertex.

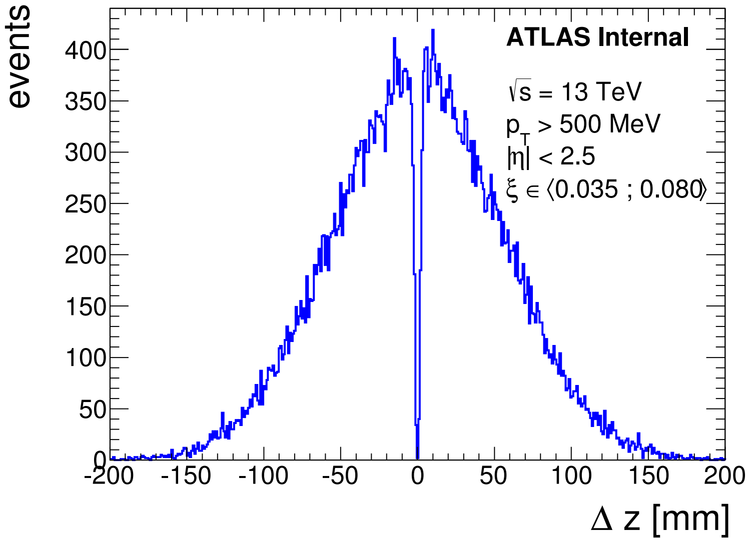

Figure 8.2: The distribution of the distance along the z axis (Δz) between two primary vertices reconstructed in the event for the data sample containing events with exactly two reconstructed primary vertices.

To estimate the number of missing events within the "well" region, N_{miss}, Gaussian distribution was fitted to the distribution of $|\Delta z|$ for $|\Delta z| > 10$ mm. The distribution of $|\Delta z|$ was constructed due to the limited statistics in the selected sample. Since it is expected that the maximum of the distribution should be at zero, it was set as the mean value in the fit. The $|\Delta z|$ distribution together with the fitted function is presented in Fig. 8.3.

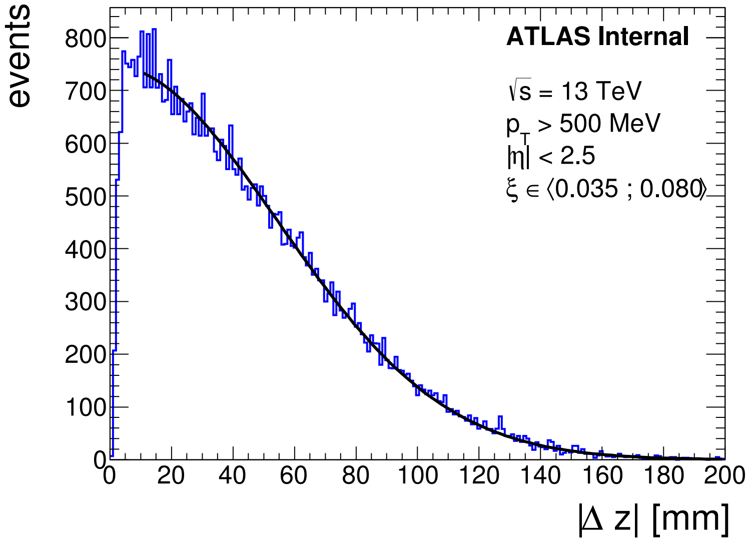

Figure 8.3: The $|\Delta z|$ distribution between two primary vertices reconstructed in the event (blue line). Gaussian distribution with zero mean value was fitted in the range $|\Delta z| > 10$ mm (black line).

The N_{miss} value was calculated as the difference of the integrals of the fitted function and the actual $|\Delta z|$ distribution. Later on, the track multiplicity distribution for the events with two reconstructed primary vertices was normalized to N_{miss} and multiplied by the AFP_prescale – the total factor is denoted by q.

The contribution of background related to the vertex reconstruction to the signal sample is shown in Fig. 8.4, as a function of a n_{trk}. It is only 0.09% in the range of the AFP accepted proton ξ: $\langle 0.035; 0.080\rangle$. The combinatorial background contribution is also presented in this figure.

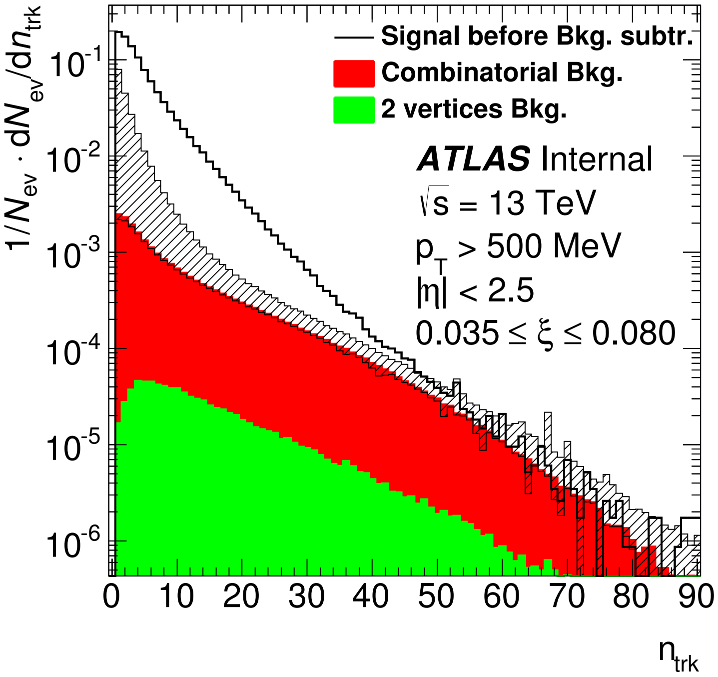

Figure 8.4: The normalized track multiplicity distributions: for the combinatorial background (red area), for the background related to the vertex reconstruction (green area) and for the signal sample before background subtraction (black line). The dashed area corresponds to the systematic uncertainty of the combinatorial background distribution.

To estimate the transverse momentum and the pseudorapidity distributions for the background related to the vertex reconstruction, the p_{T} and η distributions obtained from the selected sample were scaled by the factor q. The resulting background contributions are presented in Fig. 8.5. Since the discussed background contribution is negligible compared to the other considered background, the estimation of its uncertainty was not performed.

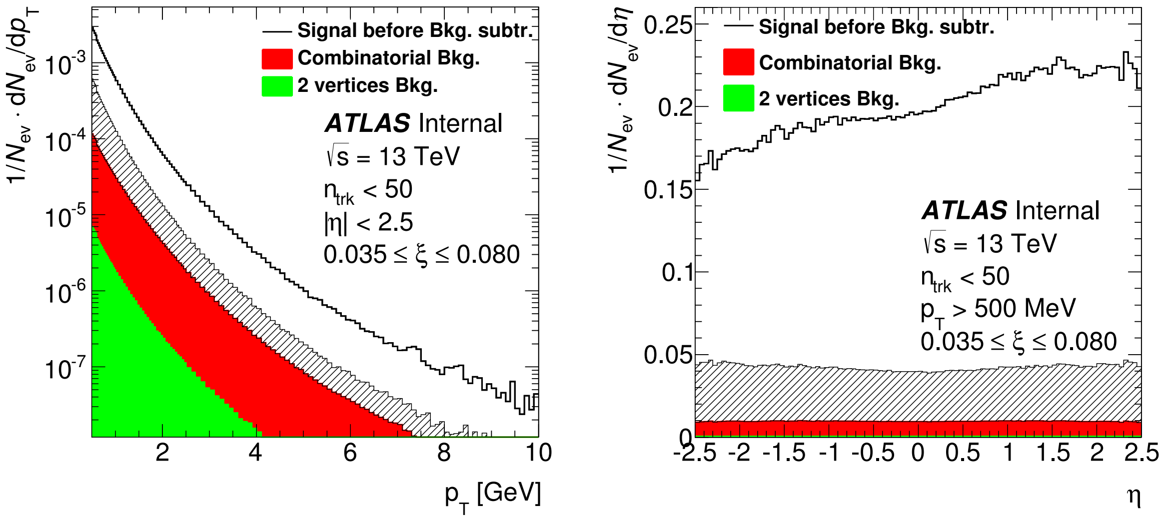

(a) (b)

Figure 8.5: The normalized (a) transverse momentum, (b) pseudorapidity distributions: for the combinatorial background (red area), for the background related to the vertex reconstruction (green area) and for the signal sample before background subtraction (black line). The dashed area corresponds to the systematic uncertainty of the combinatorial background distribution.

CHAPTER 9

UNFOLDING

Below the unfolding procedure applied to the data multiplicity distribution is described. After subtraction of the background distributions from the signal distributions, the remaining detector effects have to be corrected for. The charged track multiplicity has to be related to the charged particle multiplicity. This is done using the iterative bayesian unfolding procedure, described in detail in [94].

Below, a model leading to the formula for the charged particle multiplicity distribution, coming from the distribution of charged tracks, based on [94], is described. One can think of a situation when there exist several independent causes C_i which can produce one effect E. When $\widetilde{n}(E)$ events with the effect E are observed, the number of events related to the i-th cause can be written as:

$$n(C_i) = \widetilde{n}(E) \cdot P(C_i|E)\,. \tag{9.1}$$

Term $P(C_i|E)$ expresses a conditional probability for occuring C_i given that E is true. The effect E can be an observation of a given number of charged tracks, n_{trk}, within the detector acceptance. It may result from events with n_{ch} created particles. The difference between n_{trk} and n_{ch} can be due to the reconstruction procedure.

Following (9.1), the number of events with n_{ch} particles produced, $N_{\mathrm{ev}}(n_{\mathrm{ch}})$, can be related to the observation of $\widetilde{N}_{\mathrm{ev}}(n_{\mathrm{trk}})$ events with n_{trk} reconstructed tracks:

$$N_{\mathrm{ev}}(n_{\mathrm{ch}}) = \widetilde{N}_{\mathrm{ev}}(n_{\mathrm{trk}}) \cdot P(n_{\mathrm{ch}}|n_{\mathrm{trk}})\,. \tag{9.2}$$

When there are several possible effects to be observed, namely several possible track multiplicities n_{trk}, then (9.2) goes into:

$$N_{\mathrm{ev}}(n_{\mathrm{ch}}) = \sum_{n_{\mathrm{trk}} \geq 0} \widetilde{N}_{\mathrm{ev}}(n_{\mathrm{trk}}) \cdot P(n_{\mathrm{ch}}|n_{\mathrm{trk}})\,. \tag{9.3}$$

Terms $N_{\mathrm{ev}}(n_{\mathrm{ch}})$ and $\widetilde{N}_{\mathrm{ev}}(n_{\mathrm{trk}})$ are in fact the multiplicity distributions of the created charged particles and the observed charged tracks, respectively.

There is some fraction of events that are lost due to the track reconstruction inefficiency but otherwise would pass the particle level cuts, i.e. having $n_{\mathrm{ch}} \geq 1$ and $n_{\mathrm{trk}} = 0$. Their number can be recovered using a factor $\varepsilon_{\mathrm{miss}}(n_{\mathrm{ch}})$:

$$\varepsilon_{\mathrm{miss}}(n_{\mathrm{ch}}) = 1 - (1 - \overline{\varepsilon}_{\mathrm{trk}})^{n_{\mathrm{ch}}} \tag{9.4}$$

where $\overline{\varepsilon}_{\mathrm{trk}}$ is the mean tracking efficiency for events with $n_{\mathrm{trk}} = 1$ and is equal to about 0.77 (this is the number averaged over tracks). This factor tells about the efficiency of a reconstruction of all the tracks in the case of n_{ch} particles produced and is significant only for events with lowest n_{ch}. The corrected distribution is given by:

$$N_{\mathrm{ev}}(n_{\mathrm{ch}}) = \frac{1}{\varepsilon_{\mathrm{miss}}(n_{\mathrm{ch}})} \cdot \sum_{n_{\mathrm{trk}} \geq 1} \widetilde{N}_{\mathrm{ev}}(n_{\mathrm{trk}}) \cdot P(n_{\mathrm{ch}}|n_{\mathrm{trk}}), \tag{9.5}$$

The yet unknown term $P(n_{\mathrm{ch}}|n_{\mathrm{trk}})$ can be evaluated applying Bayes' theorem.

In general, Bayes' theorem states that:

$$P(A \cap B) = P(A|B) \cdot P(B) = P(B|A) \cdot P(A) = P(B \cap A), \tag{9.6}$$

where A and B are the events, $P(A)$ and $P(B)$ are the probabilities of observing A and B independently of each other, $P(A \cap B)$ and $P(B \cap A)$ are the joint probabilities, $P(A|B)$ is the conditional probability: the probability of event A occurring given that B is true and $P(B|A)$ is also the conditional probability: the probability of event B occurring given that A is true.

In terms of the track and charged particle multiplicities, (9.6) may be rewritten as:

$$P(n_{\mathrm{trk}}|n_{\mathrm{ch}}) \cdot P(n_{\mathrm{ch}}) = P(n_{\mathrm{ch}}|n_{\mathrm{trk}}) \cdot P(n_{\mathrm{trk}}), \tag{9.7}$$

Transforming (9.7), one gets following equation:

$$P(n_{\mathrm{ch}}|n_{\mathrm{trk}}) = P(n_{\mathrm{trk}}|n_{\mathrm{ch}}) \cdot \frac{P(n_{\mathrm{ch}})}{P(n_{\mathrm{trk}})}, \tag{9.8}$$

which left side, $P(n_{\mathrm{ch}}|n_{\mathrm{trk}})$, is the wanted probability allowing the calculation of the charged particle multiplicity distribution.

The central idea of the Bayesian unfolding is to get an estimate of $P(n_{\mathrm{ch}}|n_{\mathrm{trk}})$ using MC simulation and to improve that estimate iteratively. The conditional probability $P(n_{\mathrm{ch}}|n_{\mathrm{trk}})$ can be treated as a matrix element of the matrix $\mathscr{U}$ called the *unfolding matrix*. For the notation consistency, the conditional probability $P(n_{\mathrm{trk}}|n_{\mathrm{ch}})$ will be referred to as a matrix element of the *response matrix* $\mathscr{R}$.

Then, equations (9.5) and (9.8) may be rewritten as:

$$N_{\mathrm{ev}}(n_{\mathrm{ch}}) = \frac{1}{\varepsilon_{\mathrm{miss}}(n_{\mathrm{ch}})} \cdot \sum_{n_{\mathrm{trk}} \geq 1} \widetilde{N}_{\mathrm{ev}}(n_{\mathrm{trk}}) \cdot \mathscr{U}(n_{\mathrm{ch}}, n_{\mathrm{trk}}), \tag{9.9}$$

$$\mathscr{U}(n_{\mathrm{ch}}, n_{\mathrm{trk}}) = \mathscr{R}(n_{\mathrm{trk}}, n_{\mathrm{ch}}) \cdot \frac{P(n_{\mathrm{ch}})}{P(n_{\mathrm{trk}})}. \tag{9.10}$$

In the first iteration, matrix $\mathscr{U}$ is determined from MC simulation:

$$\mathscr{U}^{(1)}(n_{\mathrm{ch}}, n_{\mathrm{trk}}) = \mathscr{R}(n_{\mathrm{trk}}, n_{\mathrm{ch}}) \cdot \frac{P^{\mathrm{MC}}(n_{\mathrm{ch}})}{P^{\mathrm{MC}}(n_{\mathrm{trk}})}. \tag{9.11}$$

Matrix $\mathscr{R}$ is settled for each iteration as calculated by checking which n_{trk} corresponds to a given n_{ch}. This matrix is normalized to unity in individual columns as to have an interpretation of the probability. Distributions $P^{\mathrm{MC}}(n_{\mathrm{ch}})$ and $P^{\mathrm{MC}}(n_{\mathrm{trk}})$ are the normalized multiplicity distributions $N_{\mathrm{ev}}^{\mathrm{MC}}(n_{\mathrm{ch}})$ and $\widetilde{N}_{\mathrm{ev}}^{\mathrm{MC}}(n_{\mathrm{trk}})$ obtained from the MC simulation.

The matrix $\mathscr{U}^{(1)}$ is applied to:

$$N_{\mathrm{ev}}^{(1)}(n_{\mathrm{ch}}) = \frac{1}{\varepsilon_{\mathrm{miss}}(n_{\mathrm{ch}})} \cdot \sum_{n_{\mathrm{trk}} \geq 1} \widetilde{N}_{\mathrm{ev}}^{\mathrm{MC}}(n_{\mathrm{trk}}) \cdot \mathscr{U}^{(1)}(n_{\mathrm{ch}}, n_{\mathrm{trk}}). \tag{9.12}$$

Subsequently, in each n-th iteration, the matrix $\mathscr{U}$ is calculated again as:

$$\mathscr{U}^{(n)}(n_{\mathrm{ch}}, n_{\mathrm{trk}}) = \mathscr{R}(n_{\mathrm{trk}}, n_{\mathrm{ch}}) \cdot \frac{P^{(n-1)}(n_{\mathrm{ch}})}{P(n_{\mathrm{trk}})}, \tag{9.13}$$

where $P^{(n-1)}(n_{\mathrm{ch}})$ is the normalized particle multiplicity distribution, $N_{\mathrm{ev}}^{(n-1)}(n_{\mathrm{ch}})$, calculated in a previous iteration and $P(n_{\mathrm{trk}})$ is the normalized track multiplicity distribution, $\widetilde{N}_{\mathrm{ev}}(n_{\mathrm{trk}})$, coming from the data sample. Then the estimate of $N_{\mathrm{ev}}(n_{\mathrm{ch}})$ is updated using the matrix $\mathscr{U}^{(n)}$:

$$N_{\mathrm{ev}}^{(n)}(n_{\mathrm{ch}}) = \frac{1}{\varepsilon_{\mathrm{miss}}(n_{\mathrm{ch}})} \cdot \sum_{n_{\mathrm{trk}} \geq 1} \widetilde{N}_{\mathrm{ev}}(n_{\mathrm{trk}}) \cdot \mathscr{U}^{(n)}(n_{\mathrm{ch}}, n_{\mathrm{trk}}). \tag{9.14}$$

The distribution $N_{\mathrm{ev}}(n_{\mathrm{ch}})$ converges after few iterations – it was checked that the number of iterations equal to five is sufficient. It was checked that this method works accurately for the MC.

Matrix $\mathscr{U}^{(1)}$ is presented in Fig. 9.1. One can notice that its values do not extend along the diagonal but populate also higher and lower particle multiplicities. It is an impact of the tracking and other detector related efficiencies. The track multiplicity distribution for the data together with the distribution unfolded to the particle level are presented in Fig. 9.2. Unfolding of p_{T} and η distributions was not considered as having minor impact on the results.

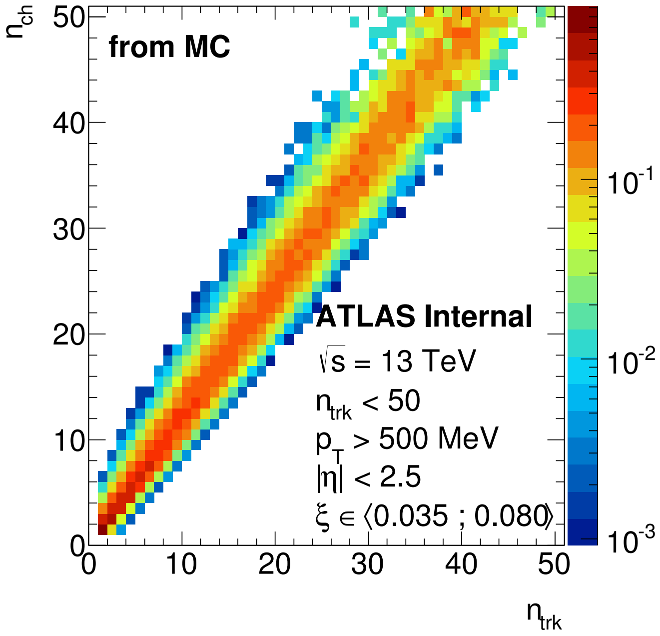

Figure 9.1: The unfolding matrix $\mathscr{U}^{(1)}$ calculated directly from the PYTHIA 8.2 Monte Carlo.

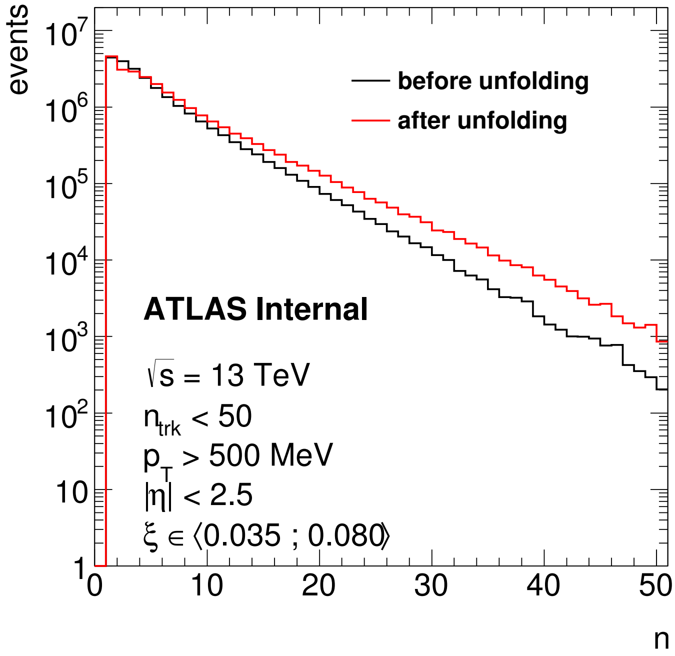

Figure 9.2: The experimentally measured track multiplicity distribution (black line) and the unfolded particle multiplicity distribution (red line) for the signal events.

CHAPTER 10

RESULTS

In this chapter the unfolded data distributions are compared to the distributions obtained using the PYTHIA 8.2 [30] and EPOS [35] generated samples (MC selection on the particle level is summarized in Appendix A.12). One should recall that the experimentally measured distributions were a subject of the following procedure:

(a) signal selection (Section 5.3),

(b) application of the vertex reconstruction efficiency (Section 6.1),

(c) application of the track reconstruction efficiency (Section 6.2),

(d) background subtraction (Chapters 7 and 8),

(e) unfolding in multiplicity (Chapter 9).

The last step is to determine the uncertainty of the final distributions.

Uncertainty determination

As the procedure leading to the uncertainty estimation on the final distributions is practically common for each of the distributions, it will be described generally. When necessary, the narration will be separated into particular distributions (the multiplicity distribution will be treated separately than the transverse momentum and pseudorapidity distributions).

From the orginal distribution for the signal sample, each of the five previously calculated variants of the distribution for the combinatorial background (Section 7.4, Eq. (7.34)) was subtracted separately. As a result, one gets five distributions for the signal after combinatorial background subtraction. Then, from each of them the distribution for the background related to the vertex reconstruction was subtracted, resulting in five distributions after overall background subtraction.

Subsequently, the procedure of the determination of the signal distribution after the background subtraction was repeated for the samples with the AFP relative alignment calculated with respect to the Far AFP station (see Section 4.4.3). However, this distribution was determined only for the default variant of the combinatorial background distribution – this is the sixth variant of the signal distribution after the background subtraction. Thus one gets six variants of the distribution.

In case of the multiplicity distribution, an unfolding procedure was applied on each of these six variants of the distribution.

Later on, each variant of the distribution was divided by the number of events. After that, each of the variants "2" to "6" was separately subtracted from the first, default, variant. It resulted in the contributions of particular sources of the uncertainty to the total uncertainty:

(a) subtraction of variant "2": uncertainty resulting from the estimation of the MBTS inefficiency using ξ_{cal} distributions,

(b) subtraction of variant "3": uncertainty resulting from the estimation of the MBTS inefficiency using AFP_MBTS trigger,

(c) subtraction of variant "4": uncertainty related to the positive uncertainty of the statistical model,

(d) subtraction of variant "5": uncertainty related to the negative uncertainty of the statistical model,

(e) subtraction of variant "6": uncertainty related to the AFP local alignment.

The resulting total uncertainty is asymmetric and calculated as a sum of squares of particular contributions, taking into account the contribution sign.

The multiplicity distributions

The charged particle multiplicity distribution for the whole proton ξ range (0.035 to 0.080), normalized to the number of events, is shown in Fig. 10.1(a), both for the data and the Monte Carlo. There is a significant disagreement between the data distribution and those from both MC predictions. PYTHIA 8.2 overestimates the data on average while EPOS on average underestimates them.

Fig. 10.1(b) presents the total relative error along with the contribution of individual sources of the uncertainty. For low particle multiplicities, the MBTS inefficiency error dominates. For high particle multiplicities (greater than 40) the errors start to grow (apart the error coming from the method exploiting ξ_{cal} method), reaching total relative error of about 100%. The smallest

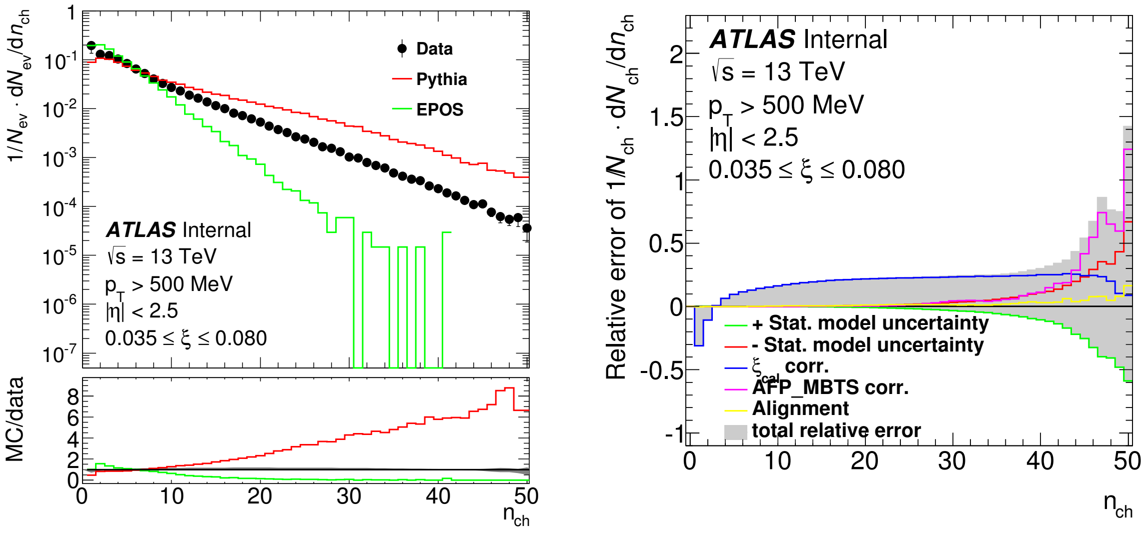

(a)

(b)

Figure 10.1: (a) The normalized multiplicity distribution of charged particles. Black dots represent the data, red line corresponds to PYTHIA 8.2 and green line to EPOS. (b) Relative error of the distribution in 10.1(a). Grey area corresponds to the total relative error while colorful line present contributions of the individual sources of the total uncertainty. The most significant uncertainty in the region of $n_{\mathrm{ch}} < 40$ comes from the estimation of the MBTS inefficiency performed using the ξ_{cal} distributions.

uncertainty is related to the AFP relative alignment – one can conclude that this measurement is not sensitive to the relative alignment settings.

Fig. 10.2(a) compares the charged particle multiplicity distributions for different ξ regions. These distributions are of similar shape, however, one can notice that within the whole region of n_{ch} the distribution for higher values of ξ (blue line) exceeds distributions obtained at lower ranges of ξ.

Fig. 10.2(b) shows a dependence of the mean particle multiplicity, $\langle n_{\mathrm{ch}} \rangle$, on the proton ξ. It grows with increasing ξ value for the data and both MC simulations. This behaviour is expected – the larger value of ξ, the larger amount of energy available in the dissociated centre-of-mass system, thus the greater amount of particles may be produced. However, the value of the $\langle n_{\mathrm{ch}} \rangle$ significantly differs between both MC simulations. EPOS predictions are closer to the data distribution than those of PYTHIA 8.2.

The transverse momentum distributions

The charged particle transverse momentum distribution for the whole range of proton ξ, normalized to the number of particles, is shown in Fig. 10.3(a) for the data and both MC simulations. PYTHIA 8.2 delivers quite a good description of the data, overestimating it by about 20% for the $p_{\mathrm{T}} > 1$ GeV. EPOS distribution has different shape and for $p_{\mathrm{T}} > 2$ GeV it

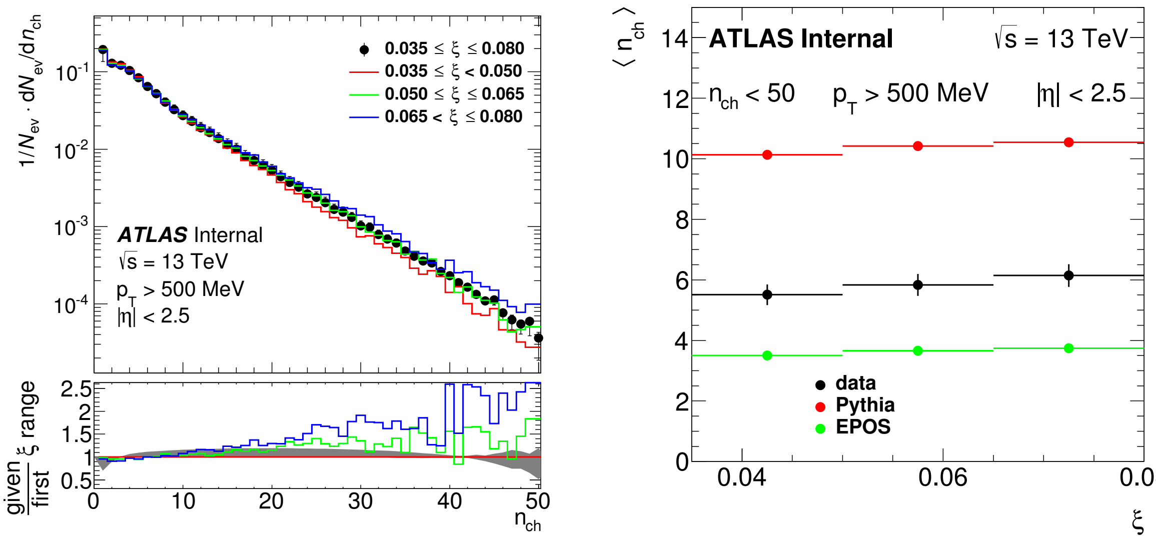

(a) (b)

Figure 10.2: (a) The normalized multiplicity distribution of charged particles in different ranges of a proton ξ. Black dots correspond to the whole range of ξ and colorful lines to the particular intervals of the whole range. The uncertainties related to the distributions marked by lines were not drawn as to preserve the plot clarity. Grey area on lower pad presents the asymmetric uncertainty related to the black points from the upper pad describing the whole range of ξ. b) The distributions of the mean charged particle multiplicities on the proton ξ. Black dots represent the data, red dots correspond to PYTHIA 8.2 and green dots to EPOS.

underestimates the data by a factor of 2.

Fig. 10.3(b) presents the total relative error along with the contribution of individual sources of uncertainty. The largest uncertainty contribution in the whole region of p_T is due to the estimation of the MBTS inefficiency performed using ξ_{cal} distributions.

Fig. 10.4(a) shows a comparison of the transverse momentum distribution of the charged particles for different ξ regions. These distributions have similar shapes. One can notice that within the whole p_T region the distribution for higher values of ξ (blue line) exceeds on average the ones observed for smaller ξ.

Fig. 10.4(b) shows a dependence of the mean particle transverse momentum, $\langle p_T \rangle$, as a function of a proton ξ. The growth of the mean p_T value with the increasing value of a proton ξ is observed for the data and both MC simulations. However, the value of the $\langle p_T \rangle$ significantly differs between two MC predictions and the observed one. PYTHIA 8.2 predictions overestimate the data and EPOS underestimate them.

The pseudorapidity distributions

The charged particle pseudorapidity distribution for the whole range of a proton ξ, normalized to the number of particles, is shown in Fig. 10.5(a) for the data and both MC simulations. One

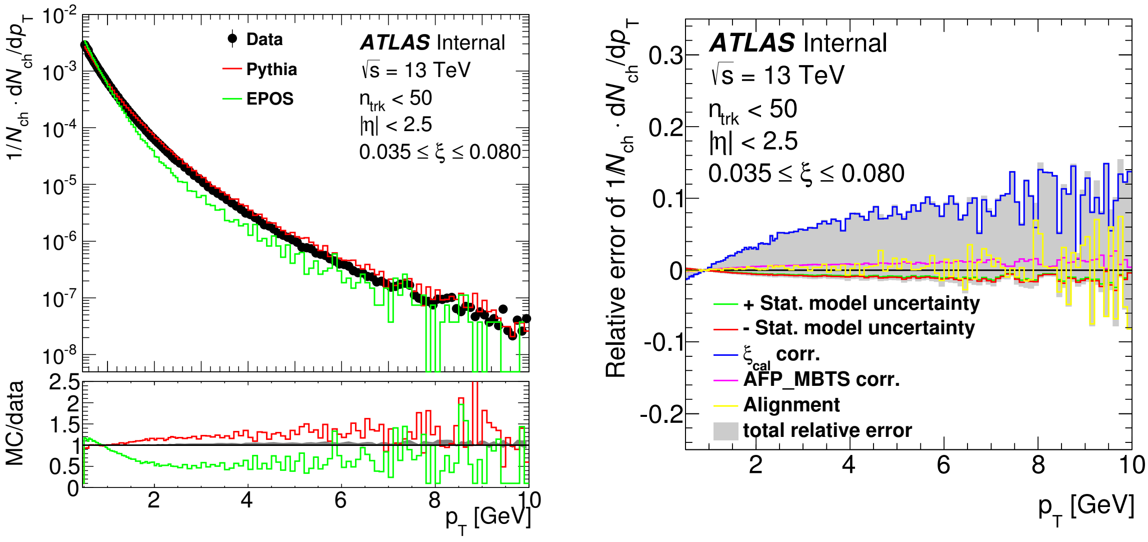

(a) (b)

Figure 10.3: (a) The normalized transverse momentum distribution of charged particles. Black dots represent the data, red line corresponds to PYTHIA 8.2 and green line to EPOS. (b) Relative error of the distribution in 10.3(a). Grey area corresponds to the total relative error while colorful line present contributions of the individual sources of the total uncertainty. The most significant uncertainty in the whole region of p_T comes from the estimation of the MBTS inefficiency performed using the ξ_{cal} distributions.

can notice an essential difference in the slope of the distributions between the data and both MC model predictions. In the data the particles clearly prefer positive values of η. For PYTHIA 8.2 that tendency is also slightly observed, but is definitely less pronounced than in the data. On the other hand, EPOS predicts even opposite behaviour and a bit more particles with negative η. It is worth reminding that the proton was reconstructed on side C, which corresponds to negative values of pseudorapidity.

Fig. 10.5(b) presents the total relative error along with the contribution of individual sources of uncertainty. This is an error with respect to the values in Fig. 10.5(a). The most significant uncertainty contribution in the whole region of η comes from the estimation of the MBTS inefficiency performed with the use of ξ_{cal} distributions.

Fig. 10.6(a) shows comparison of pseudorapidity distribution of charged particles for particular ξ regions. These distributions have similar shapes. One can notice that positive values of η are more favored in the region of lower values of ξ (red line).

In Fig. 10.6(b) one can see a dependence of the mean particle pseudorapidity, $\langle\eta\rangle$, on a proton ξ. Both for the data and PYTHIA 8.2 the decrease of the $\langle\eta\rangle$ value with increasing value of a proton ξ is observed. However, PYTHIA 8.2 largely underestimates $\langle\eta\rangle$. EPOS predicts the opposite dependence of $\langle\eta\rangle$ on the proton ξ and also largely underestimates $\langle\eta\rangle$.

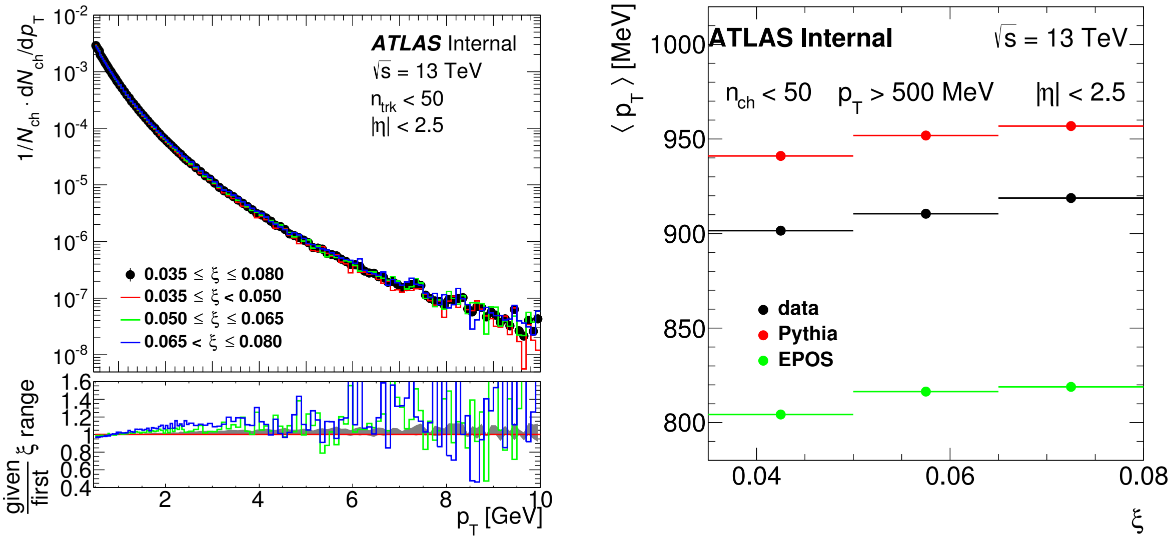

(a) (b)

Figure 10.4: (a) The normalized transverse momentum distribution of charged particles in different ranges of proton ξ. Black dots correspond to the whole range of ξ and colorful lines to the particular intervals of the whole range. The uncertainties related to the distributions drawn with lines were not drawn as to preserve the plot clarity. Grey area on the lower pad presents the asymmetric uncertainty related to the black points from the upper pad (regarding whole range of ξ). b) The distributions of the mean transverse momentum on the proton ξ. Black dots represent the data, red dots correspond to PYTHIA 8.2 and green dots to EPOS.

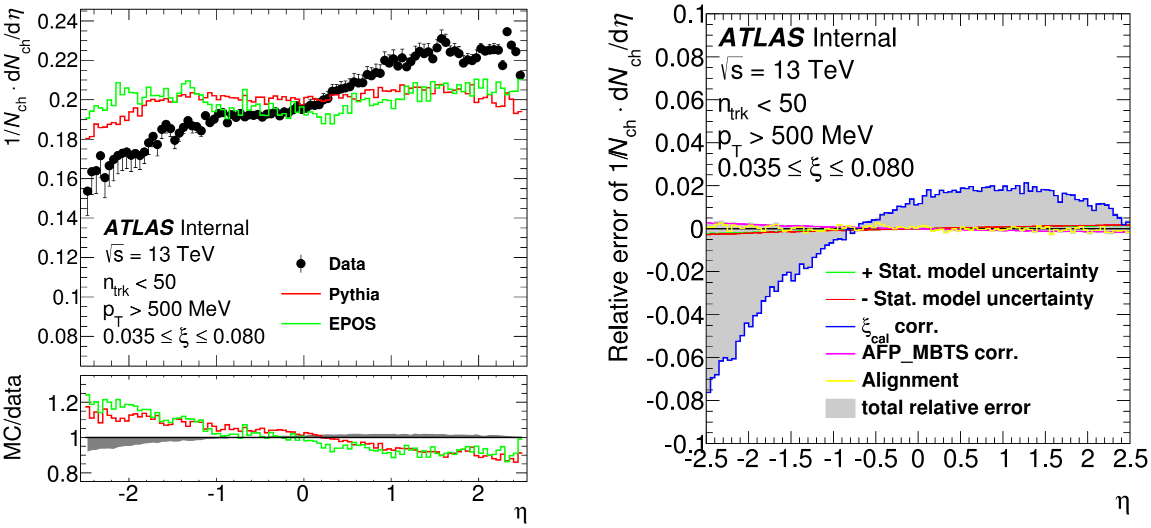

(a)

(b)

Figure 10.5: (a) The normalized pseudorapidity distribution of charged particles. Black dots represent data, red line corresponds to PYTHIA 8.2 and green line to EPOS. (b) Relative error of the distribution in 10.5(a). Grey area corresponds to the total relative error while colorful line present contributions of the individual sources of the total uncertainty. The most significant uncertainty in the whole region of η comes from the estimation of the MBTS inefficiency performed using the ξ_{cal} distributions.

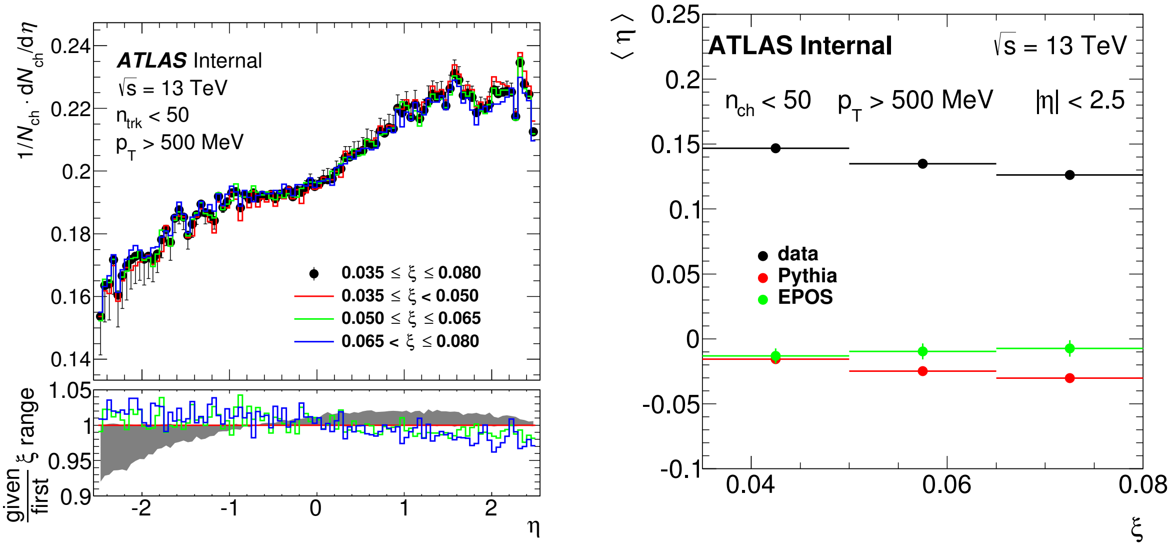

(a)

(b)

Figure 10.6: (a) The normalized pseudorapidity distribution of charged particles in different ranges of a proton ξ. Black dots correspond to the whole range of ξ and colorful lines to the particular intervals of the whole range. The uncertainties related to the distributions drawn with lines were not drawn as to preserve a plot clarity. Grey area on the lower pad presents the asymmetric uncertainty related to the black points from the upper pad describing whole range of ξ. b) The distributions of the mean pseudorapidity on the proton ξ. Black dots represent the data, red dots correspond to PYTHIA 8.2 and green dots to EPOS.

CHAPTER 11

SUMMARY AND CONCLUSIONS

In this dissertation the proton–proton interactions with a forward proton in the final state were investigated. The measurement was performed using the ATLAS detector at the LHC and its forward subdetector – the AFP. The data were collected by the ATLAS experiment in 2017. The integrated data luminosity amounts to about 51 nb^{-1}. The measurement was performed at the centre-of-mass energy $\sqrt{s} = 13$ TeV for the low values of the proton relative energy loss amounting between 0.035 and 0.080, what can be translated into the diffractive mass within the range $\langle 2.4; 3.7 \rangle$ TeV.

The charged-particle multiplicity, its dependence on the transverse momentum and the pseudorapidity are presented. The measurements are performed for charged particles with transverse momentum greater than 500 MeV and absolute pseudorapidity less than 2.5, in events with at least one charged particle satisfying these kinematic requirements. To obtain the results, the ATLAS Inner Detector and MBTS detector inefficiencies were corrected for. Two sources of background were estimated and subtracted. Finally, the unfolding in the multiplicity was performed.

Predictions of the two Monte Carlo simulations have been compared to the data. First of them was PYTHIA 8.2 in tune A2-MSTW2008LO dedicated for minimum bias analysis. In this approach the diffractive proton–proton interactions are treated as non-diffractive hadronic collisions between a proton and a Pomeron. The second involved MC model was EPOS, not using the parton distribution functions, but instead exploiting the Gribov-Regge theory. Here, both the soft and hard interactions are described simultaneously in terms of parton ladders.

In the studied kinematic region there is a clear discrepancy of the multiplicity distribution between the data and MC simulations, with PYTHIA 8.2 overestimating on average the multiplicity and EPOS underestimating it. The transverse momentum distribution is well described by PYTHIA 8.2 only for $p_{\mathrm{T}} > 1$ GeV. For higher p_{T} values it overestimates the data by about 20%. EPOS distribution has different shape and for $p_{\mathrm{T}} > 2$ GeV it underestimates the data by a factor of 2. The pseudorapidity distribution is wrongly described by both MC simulations.

Slight changes of the particle distributions within different regions of the diffractively scattered proton ξ were observed. The growth of the mean charged multiplicity and the mean transverse momentum per particle with the increasing proton ξ is measured. The mean pseudorapidity per particle decreases when the ξ is getting larger. However, the investigated range of ξ was quite narrow: $\xi \in \langle 0.035; 0.080 \rangle$. It can be further expanded into the full range of the AFP detector acceptance: $\xi \in \langle 0.02; 0.1 \rangle$ in the future.

There is a scope for the improvement of the future analysis concerning particle disitributions in the events with the tagged forward proton. For instance, the influence of the global and local AFP alignment should be investigated and included. What is more, the disagreement between the data distributions and MC predictions gives the opportunity of tuning the MC simulations. Additionally, the results concerning background estimation can be further used in other analysis using the AFP detector.

APPENDIX A

SAMPLE SELECTIONS

For the convenience of the reader, the different selection criteria, both for the data sample and MC samples, were collected together in this Appendix. First, the selections for the data samples are listed, starting from the signal sample and then following the order of occurence in the text. One should notice that there is a common selection criteria for each data sample selection: the requirement of the range of the luminosity blocks with the AFP in data taking position and with constant trigger prescales (248 - 453). Afterwards, selection criteria for MC samples are summarized.

A.1 Data – signal sample

- the AFP trigger fired,
- exactly one proton is reconstructed in the AFP on side C and its ξ is within one of the predefined ranges,
- exactly one reconstructed primary vertex in the ID,
- at least one good track in the ID in the event, where a good track is defined as follows:
  - transverse momentum $p_{\mathrm{T}} > 500$ MeV,
  - pseudorapidity $|\eta| < 2.5$,
  - at least 1 hit in the Pixel detector,
  - at least 6 hits in the SCT detector,
  - the transverse impact parameter d_0, calculated with respect to the LHC beam-axis, is smaller than 1.5 mm,

  - the longitudinal impact parameter z_0, calculated withe respect to the primary vertex, multiplied by $\sin(\theta)$, is smaller than 1.5 mm

A.2 Data – sample for the statistical model calculations

- the AFP trigger fired,
- exactly one proton is reconstructed in the AFP on side C and its ξ is within one of the predefined ranges,
- none, one or two reconstructed vertices in the ID and at least one good track in the event (the good track definition the same as in A.1)

A.3 Data – sample for the calculation of parameter μ_{MB} from the n_{vtx} distribution

- the MBTS trigger fired

A.4 Data – combinatorial background sample

- the MBTS trigger fired,
- no proton reconstructed in the AFP on side C,
- exactly one reconstructed primary vertex in the ID and at least one good track in the event (the good track definition the same as in A.1)

A.5 Data – sample for calculation of the MBTS inefficiency using the AFP_MBTS trigger

- the AFP_MBTS trigger fired,
- exactly one proton is reconstructed in the AFP on side C and its ξ is within one of the predefined ranges,
- exactly one reconstructed primary vertex in the ID and at least one good track in the event (the good track definition the same as in A.1)

A.6 Data – sample for calculation of the MBTS inefficiency using minimum bias Monte Carlo

- the MBTS trigger fired,
- exactly one reconstructed primary vertex in the ID and at least one good track in the event (the good track definition the same as in A.1)

A.7 Data – sample for calculation of the MBTS inefficiency using the $\xi_{\mathbf{cal}}$ distributions

- the MBTS trigger fired,
- no proton reconstructed in the AFP on side C,
- exactly one reconstructed primary vertex in the ID and at least one good track in the event (the good track definition the same as in A.1)

A.8 Data – sample for background related to the vertex reconstruction

- the AFP trigger fired,
- exactly one proton is reconstructed in the AFP on side C and its ξ is within one of the predefined ranges,
- two reconstructed primary vertices in the ID and at least one good track in the event (the good track definition the same as in A.1)

A.9 Monte Carlo – signal sample on the track level

- exactly one proton is reconstructed in the AFP on side C and its ξ is within one of the predefined ranges,
- exactly one reconstructed primary vertex in the ID and at least one good track in the event (the good track definition the same as in A.1)

After selection, contributions of particular processes in the merged single-diffractive-like sample for PYTHIA 8.2 in the range of $\xi \in \langle 0.035; 0.080 \rangle$ are the following:

(a) single-diffractive: 88.51 %,

(b) double-diffractive: 9.45 %,

(c) non-diffractive: 2.04 %.

A.10 Monte Carlo – minimum bias sample

- exactly one reconstructed primary vertex in the ID and at least one good track in the event (the good track definition the same as in A.1)

After selection, contributions of particular processes in the merged minimum bias sample for PYTHIA 8.2 are the following:

(a) single-diffractive: 19.54%,

(b) double-diffractive: 12.88%,

(c) non-diffractive: 67.58%.

A.11 Monte Carlo – ND-like sample

- no proton reconstructed in the AFP on side C,
- exactly one reconstructed primary vertex in the ID and at least one good track in the event (the good track definition the same as in A.1)

After selection, contributions of particular processes in the merged non-diffractive-like sample for PYTHIA 8.2 are the following:

(a) single-diffractive: 14.53%,

(b) double-diffractive: 10.50%,

(c) non-diffractive: 74.97%.

A.12 Monte Carlo – signal sample on the particle level

- exactly one truth proton is on side C within one of the predefined ξ ranges,
- exactly one reconstructed primary vertex in the ID,
- at least one charged particle in the final state in the event with $p_{\mathrm{T}} > 500$ MeV and $|\eta| < 2.5$

APPENDIX B

MBTS TRIGGER INEFFICIENCY

This Appendix is dedicated to the description of the two additional methods exploited in the MBTS trigger inefficiency estimation. Both of them are used for the estimation of the systematic uncertainty.

B.1 The MBTS correction with the use of the AFP_MBTS trigger

This method of correcting for the MBTS inefficiency is data driven and directly related to the differences between the Inner Detector and the MBTS acceptances.

The MBTS detector geometric acceptance is different than that of the Inner Detector. Therefore, imposing an additional condition of the MBTS trigger on the signal sample (the AFP triggered sample with a reconstructed primary vertex and at least one good reconstructed track) may change the track multiplicity distribution. This feature was used to calculate the MBTS inefficiency.

An additional data sample was prepared, following almost the same event and track selection as the signal data sample, with the only difference in the choice of the trigger (the sample selection is summarized in Appendix A.5). The trigger based on the coincidence of the AFP and MBTS detector signals was requested. It will be denoted as “AFP_MBTS trigger”. This trigger is prescaled by 40.

The track multiplicity distributions were constructed for both the AFP and the AFP_MBTS triggered samples (see Fig. B.1(a)). Their ratio is presented in Fig. B.1(b). For lowest multiplicities the distribution for the AFP triggered data is higher than the distribution for the AFP_MBTS triggered data – this is the region of the MBTS detector inefficiency. One should notice that this

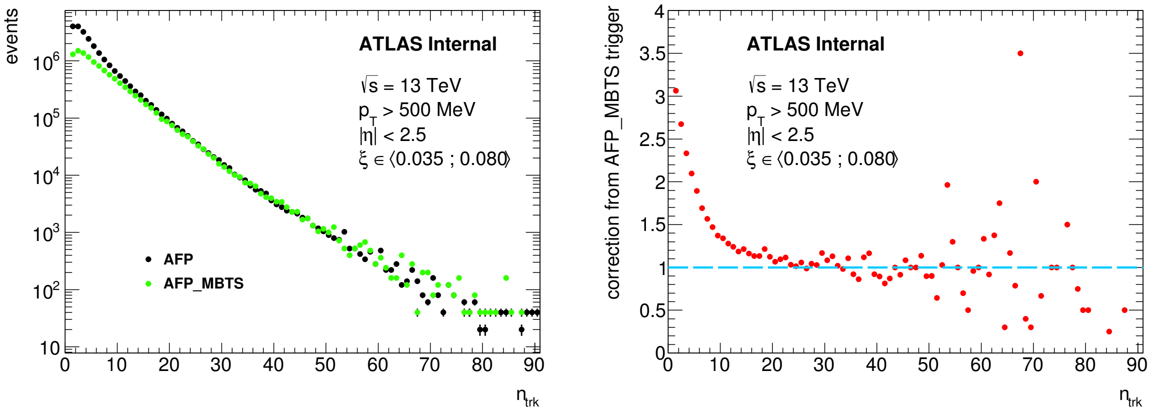

(a) (b)

Figure B.1: (a) The track multiplicity distributions for the AFP triggered sample (black dots) and for the AFP_MBTS triggered sample (green dots), with the appropriate trigger prescales applied. (b) The ratio of the track multiplicity distributions for the AFP triggered sample and the track multiplicity distributions for the AFP_MBTS triggered sample

ratio was calculated using the signal data samples. Therefore, it can be slightly different for the background process for which it is intended to be applied. Even though, this ratio serves as a correction for the track multiplicity distribution of the combinatorial background.

B.2 The MBTS correction with the use of calorimeter

The third method of correcting the combinatorial background multiplicity distribution is based on the distributions of ξ_{cal} (see Eq. (4.1)). In [95] it was pointed that the ξ_{cal} distributions for the MBTS and the AFP triggered samples differ from each other for lower ξ_{cal} values while have the same shape for the higher one (see Fig. B.2). This feature may be used to obtain yet another estimation of the contribution of the combinatorial background.

At first, the Monte Carlo simulation will be presented. The goal of this simulation is to check the shape of the ξ_{cal} distributions for particular processes, the range of values that they span and their separation from each other. It has been performed in case of no pile-up (thus no combinatorial background), using the following samples of PYTHIA 8.2:

- a signal (SD-like) sample; sample selection is summarized in Appendix A.9,
- a non-diffractive-like (ND-like) sample, which analogue in data is the MBTS triggered sample (see sample selection in Appendix A.9). Contributions of particular processes to it are the following:
    (a) single-diffractive: 14.53%,
    (b) double-diffractive: 10.50%,

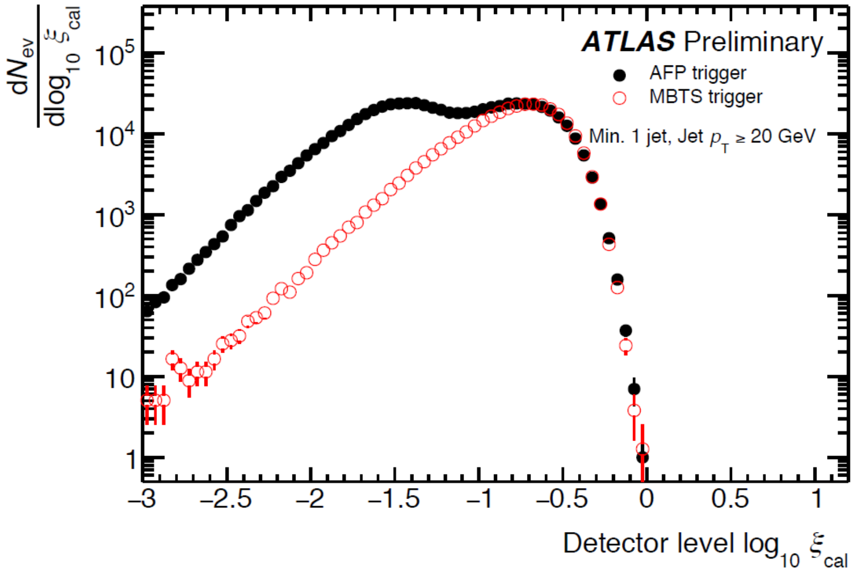

Figure B.2: The $\log_{10}\xi_{\text{cal}}$ distributions for the AFP triggered sample (black dots) and the MBTS triggered sample (red hollow dots). Figure from [95].

(c) non-diffractive: 74.97%.

Even though the sample is prevailed by the non-diffractive processes, the diffractive ones give a non-negligible contribution.

One should notice that (4.1) returns a value even for events in which no proton occured in the final state.

It is expected that the ξ_{cal} distribution shape will depend on the track multiplicity, thus the investigated track multiplicity region was divided into thirteen intervals (see Table B.1 for details): narrower for the smallest track multiplicities and wider for the higher ones. The reason of different interval widths is a limited statistics for high n_{trk}.

In order to draw conclusions about the overlap of the two ξ_{cal} distributions, for each n_{trk} interval the following procedure has been applied. At first, the ξ_{cal} distribution for the ND-like sample was scaled as to make its contribution to the SD-like sample equal to that of the combinatorial background track multilplicity distribution (including correction on the MBTS inefficiency determined using minimum bias MC sample) to the signal one. These contributions are summarized in Table B.1. As the obtained numbers will be used only for some rough estimates, their uncertainties were omitted. Next, both ξ_{cal} distributions (SD-like and ND-like) were summed. Then the resulting disribution was rescaled such that its maximum match that of the AFP ξ_{cal} distribution (the reason for such treatment will be explained further in the text).

The ξ_{cal} distributions for low and large track multiplicities are shown in Figs. B.3(a) ($n_{\text{trk}} = 2$) and B.3(b) ($n_{\text{trk}} \in \langle 40; 49 \rangle$), respectively. One can see in Figs. B.3(a) and B.3(b) that the distribution

Table B.1: Contribution of the combinatorial background to the signal sample (before any background subtraction) in selected track multiplicity intervals for $\xi \in \langle 0.035; 0.080 \rangle$. Contributions in particular n_{trk} intervals are calculated based on the statistical model with the correction on the MBTS inefficiency determined using minimum bias MC sample.

n_{trk}	comb bg contribution [%]
1	1.3
2	1.3
3-4	1.5
5-6	1.8
7-9	2.3
10-14	3.4
15-19	6.0
20-24	10.4
25-29	17.0
30-34	27.2
35-39	40.7
40-49	58.4
50-90	77.4

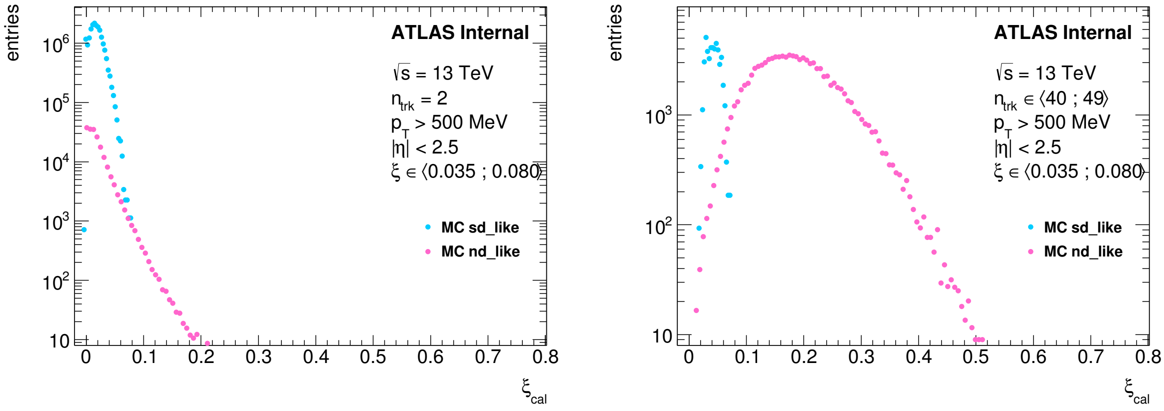

(a) (b)

Figure B.3: The ξ_{cal} distributions for MC SD-like sample (blue dots) and ND-like sample (pink dots) for events with the track multiplicity: (a) equal to 2, (b) between 40 and 49.

for the SD-like sample suddenly vanishes for the least populated values of ξ_{cal}. This effect is caused by a limited statistics of the SD-like sample. To compare the distributions for the two MC samples, the SD-like one was extrapolated assuming that for higher ξ_{cal} values it is of an exponential form: $e^{a+b\cdot\xi_{\text{cal}}}$. The extrapolated distributons are presented in Figs. B.4(a) and B.4(b).

According to PYTHIA 8.2 predictions, the ξ_{cal} distribution for the SD-like processes is narrow both for small and large track multiplicities and covers region of small ξ_{cal} values. For low n_{trk} the ξ_{cal} distribution for the ND-like processes is quite narrow and extending up to 0.2 (see Fig.

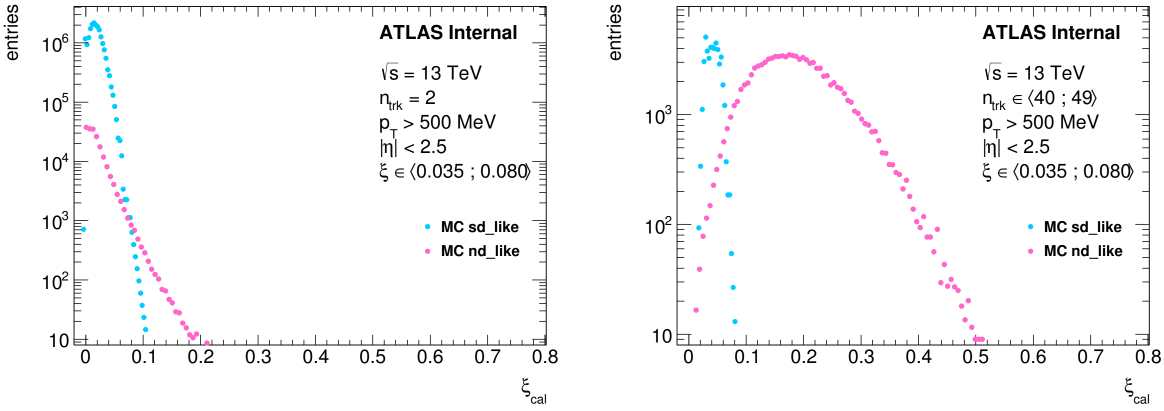

(a) (b)

Figure B.4: The ξ_{cal} distributions for MC SD-like sample (blue dots) and ND-like sample (pink dots) for events with the track multiplicity: (a) equal to 2, (b) between 40 and 49. Distribution for the SD-like sample was extrapolated towards higher values of ξ_{cal} using the function of the form $e^{a+b\cdot\xi_{\text{cal}}}$.

B.4(a)) thus the lack of overlap of these two distributions is observed only in a range of highest ξ_{cal} values. A situation changes for higher n_{trk} (see Fig. B.4(b)), where the distribution for the ND-like sample is wide and extends from small to high values of ξ_{cal}. The ND-like and SD-like distributions overlap in the range of the latter. A substantial shift of the maximum of the ND-like distribution with increasing n_{trk} is also observed. As a result, in case of events with high track multiplicities, the distribution for the SD-like sample is quite well separated from the that for the ND-like sample.

To simulate the shapes of the experimental distributions for the AFP and the MBTS triggered samples (see sample selections in Appendices A.1 and A.4, respectively), one can use the above MC distributions. As already discussed, the AFP triggered sample contains both the signal and the combinatorial background events. Then the ξ_{cal} distribution for the AFP triggered sample can be roughly described as a sum of the ξ_{cal} distributions for the two interactions:

- first one giving a signal only in the AFP and does not resulting in a reconstructed primary vertex, for which it is expected that the high activity in the calorimeter will occur rarely.
- second one resulting in a reconstructed primary vertex and does not giving signal in the AFP, with the calorimeter activity related to the particles coming mainly from the ND-like process.

Thus the ξ_{cal} distribution that will mimic that for the AFP triggered sample was constructed as the sum of the SD-like and the ND-like ξ_{cal} distributions. The ξ_{cal} distribution simulating that for the MBTS triggered sample was taken as the ξ_{cal} distribution for the ND-like sample. They are shown in Fig. B.5.

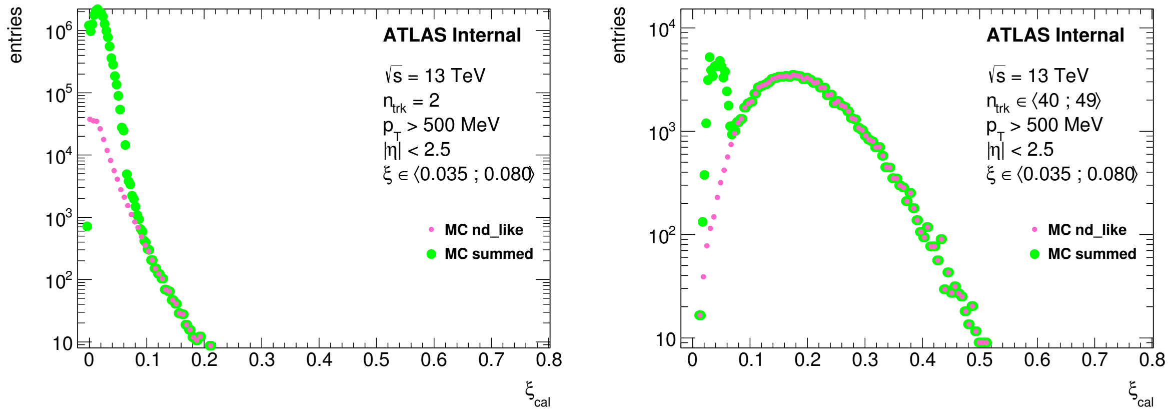

(a) (b)

Figure B.5: The ξ_{cal} distributions for the sum of MC SD-like sample and ND-like sample (green dots) and ND-like sample (pink dots) for events with the track multiplicity: (a) equal to 2, (b) between 40 and 49.

In line with previous observations, for both low and high track multiplicities, the tail of the resulting distribution, denoted as "MC summed", overlaps with that for ND-like sample. The same feature should be observed in the data if the MC description is correct. Namely, the ξ_{cal} distribution for the AFP triggered sample should overlap with that for the MBTS triggered sample assuming correct relative normalization.

In conclusion, this method allows determination of the correction G. Steps of the method are the following:

1. Construct the ξ_{cal} distributions for the AFP and the MBTS triggered samples in the track multiplicity intervals listed in Table B.1 and multiply them by trigger prescales.

2. For each interval multiply the ξ_{cal} distribution for the MBTS triggered sample by the contribution of the combinatorial background estimated from the statistical model, without applying any other corrections.

   The ξ_{cal} distributions obtained at this stage are presented in Fig. B.6, for the same multiplicity intervals as for the MC samples.

3. In each interval compare the shapes of the ξ_{cal} distributions for the AFP and the MBTS triggered samples and find the region of the higher ξ_{cal} values in which these two distributions are "parallel" to each other (in Fig. B.6(a) this is $\xi_{\text{cal}} > 0.45$ and in Fig. B.6(b) this is $\xi_{\text{cal}} > 0.53$).

4. Find a scaling factor G by which the ξ_{cal} distribution for the MBTS triggered sample has to be multiplied to make the high ξ_{cal} regions overlap.

It is done by the minimization of the χ^2 function given by:

$$\chi^2(G) = \sum_i \frac{[y_i(\mathrm{AFP}) - G \cdot y_i(\mathrm{MBTS})]^2}{\sigma_i^2(\mathrm{AFP}) + \sigma_i^2(\mathrm{MBTS})}, \tag{B.1}$$

where the sum runs over ξ_{cal} bins and y_i are the values reached by the ξ_{cal} distributions. The distributions after the fit are presented in Fig. B.7.

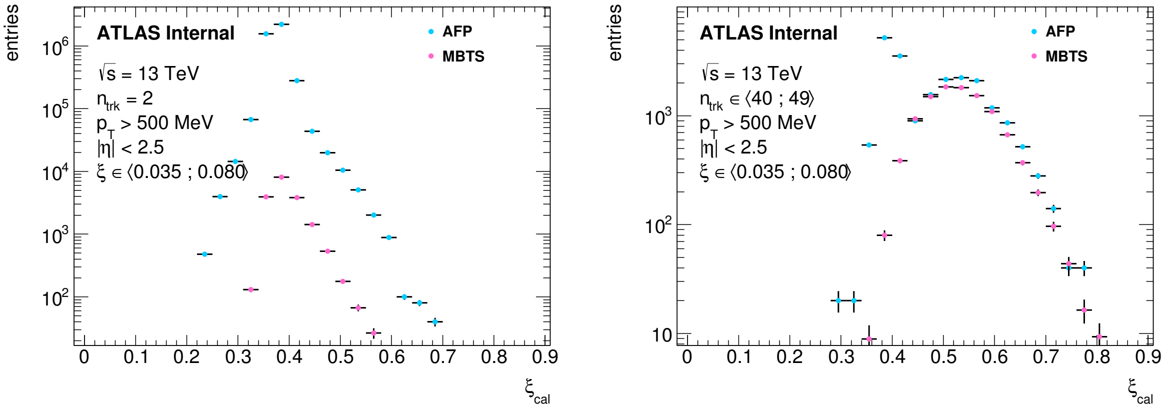

(a) (b)

Figure B.6: The ξ_{cal} distributions for the AFP triggered sample (light blue dots) and the MBTS triggered sample (pink dots) for events with the track multiplicity: (a) equal to 2, (b) between 40 and 49. The distributions for the MBTS triggered sample were normalized to the contribution of the combinatorial background determined in Section 7.2.2.

Values of the correction factors in the track multiplicity intervals are presented in Table B.2. They are the largest for low multiplicities and close to one for high multiplicities. It was found that the multiplicity dependence of the above correction factor G can be described by a function:

$$G(n_{\mathrm{trk}}) = a \cdot e^{b \cdot n_{\mathrm{trk}}^{c}} + d. \tag{B.2}$$

Functional form allows application of the correction for each n_{trk} value. The correction factors and the corresponding correction function fitted into them are presented in Fig. B.8. Parameters of the correction function are listed in Table B.3.

The correction method exploiting ξ_{cal} distributions was applied under the assumption that the MC simulation is trustworthy – that the shapes of the ξ_{cal} distributions for the SD-like and the ND-like processes and their separation will be reproduced by the data. Essentially, to use this correction method, the ξ_{cal} distributions for the SD-like and the ND-like processe have to be well separated from each other in the region of higher values of ξ_{cal}.

The first difference that one can notice between the ξ_{cal} distributions for the MC (see Fig. B.5) and the data (see Fig. B.7) is the populated range of ξ_{cal} values – the data distributions are shifted

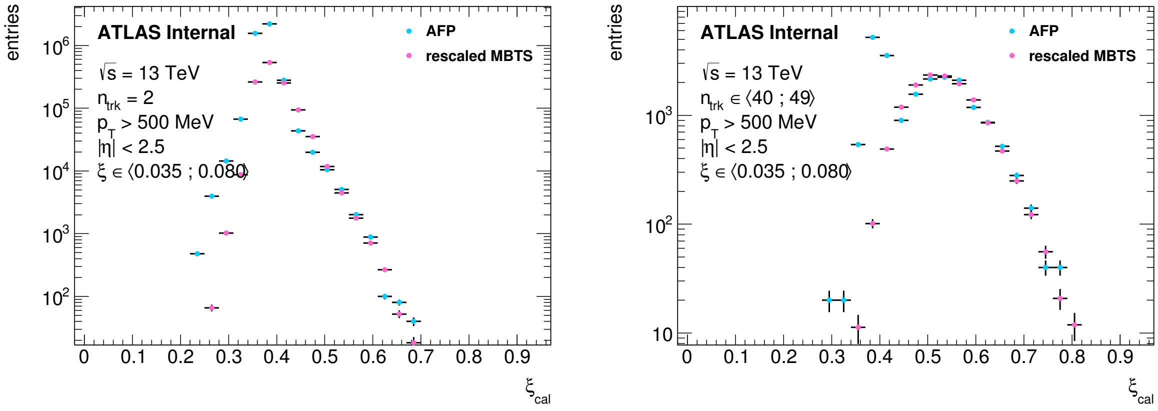

(a) (b)

Figure B.7: The ξ_{cal} distributions for the AFP triggered sample (light blue dots) and the MBTS triggered sample (pink dots) for events with the track multiplicity: (a) equal to 2, (b) between 40 and 49. Distribution for the MBTS trggered sample was fitted to the distribution for the AFP triggered sample in the range of higher values of ξ_{cal}, where the right slope of the distribution for the MBTS triggered data is parallel to the right slope of the distribution for the AFP triggered data.

Table B.2: The correction factors G calculated from the ξ_{cal} distributions

n_{trk}	correction G
1	72.7 ± 4.9
2	66.6 ± 4.0
3-4	31.6 ± 1.1
5-6	13.87 ± 0.41
7-10	5.885 ± 0.083
10-14	2.932 ± 0.030
15-19	1.925 ± 0.020
20-24	1.534 ± 0.017
25-29	1.358 ± 0.016
30-34	1.367 ± 0.026
35-39	1.264 ± 0.027
40-49	1.271 ± 0.022
50-90	1.163 ± 0.022

towards higher values. This shift is due to the fact that the MC simulation does not describe the calorimeter response properly. The shift of the ξ_{cal} distributions of 0.35 for the summed MC samples was added manually and afterwards they were compared to the ξ_{cal} distributions for the AFP triggered sample, as presented in Fig. B.9. There is a significant difference of widths of the data and the MC distributions for the low n_{trk}. However, the difference in shapes between these distributions for the high n_{trk} is rather minor. A conclusion to be drawn is that in the region of

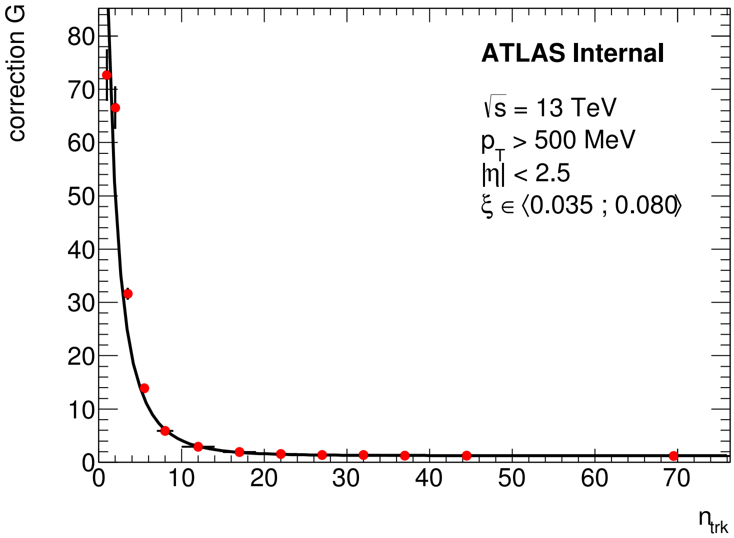

Figure B.8: Red dots depict the correction factors G obtained for thirteen multiplicity intervals. Black curve represents the fiited correction function, given by the formula $G(n_{\text{trk}}) = a \cdot e^{b \cdot n_{\text{trk}}^c} + d$, with parametrs a, b, c and d listed in Table B.3.

Table B.3: The parameters of the fitted correction function, given by the formula $G(n_{\text{trk}}) = a \cdot e^{b \cdot n_{\text{trk}}^c} + d$

	value	error
a	529	97
b	-1.70	0.15
c	0.487	0.022
d	1.256	0.013

the lowest n_{trk} the ξ_{cal} distributions for the SD-like processes and the ND-like processes are in fact not well separated and this method should not be applied in this region.

Uncertainties on the correction

One of the sources of the systematic uncertainty on the G correction is the choice of the lower limit, ξ_i, of the fit of the ξ_{cal} distribution for the MBTS triggered sample to the ξ_{cal} distribution for the AFP triggered sample. It is a point from which the distributions for the AFP and MBTS triggered samples start to have a similar slope. This point is slightly different for each track multiplicity interval. The upper limit of the fit is always set to one. To estimate this uncertainty, in each track multiplicity interval this fit was performed once more, starting from the next ξ_{cal} bin, ξ_{i+1}. The additional correction factors, G_{i+1} and the additional correction function, $G(n_{\text{trk}}, \xi_{i+1})$ were calculated. Then the uncertainty was calculated as:

$$\sigma_{\text{G}}(n_{\text{trk}}) = |G(n_{\text{trk}}, \xi_i) - G(n_{\text{trk}}, \xi_{i+1})| \, . \quad \text{(B.3)}$$

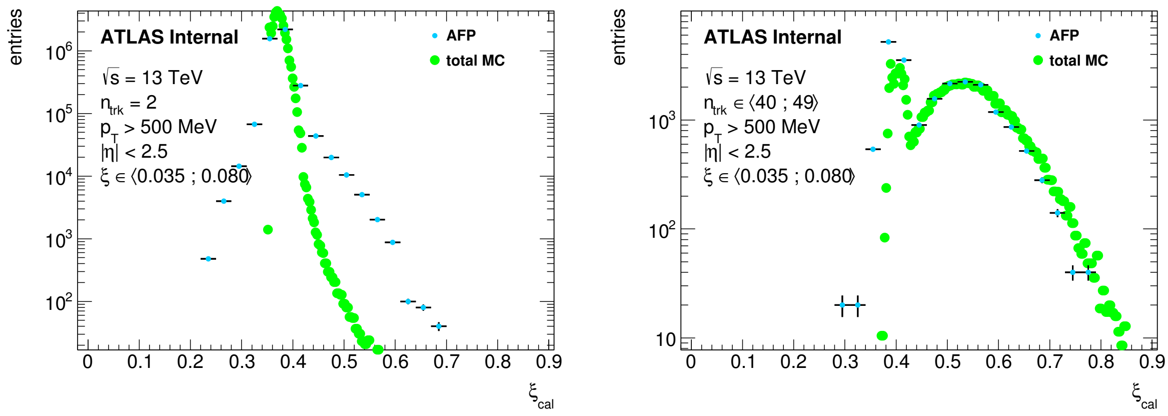

(a) (b)

Figure B.9: The ξ_{cal} distributions for the AFP triggered sample (light blue dots) and the sum of the MC SD-like sample and the ND-like sample (green dots; contribution of the ND-like sample follows Table B.1) for events with the track multiplicity: (a) equal to 2, (b) between 40 and 49. The distribution for the summed MC sample was shifted towards the higher values of ξ_{cal} by 0.36 and rescaled to the data distribution.

In general, two possible scenarios can be considered:

(a) the originally chosen lower limit of the fit, ξ_i, was the first ξ_{cal} bin in which the distributions for the AFP and the MBTS triggered samples have a similar slope. Then the fit starting from the previous ξ_{cal} bin, ξ_{i-1}, would give unreasonable value of G. In turn, a fit starting from the ξ_{i+1} bin would give result similar to the one obtained when starting from ξ_i.

(b) The originally chosen lower limit of the fit, ξ_i, was the second ξ_{cal} bin in which the distributions for the AFP and the MBTS triggered samples had similar slope. Then the fit starting from the ξ_{i-1} bin would give result similar to the one obtained for ξ_i. Likewise, a fit starting from the ξ_{i+1} bin also would give result similar to the one obtained when starting from ξ_i.

Scenario in which the ξ_i bin was chosen uncorrectly, i.e. in region where the distributions for the AFP and the MBTS triggered samples are not parallel to each other, is not taken into account. Considering the above discussion, it was decided to use in (B.3) only the ξ_{i+1} and ξ_i bins to estimate the uncertainty as to avoid scenario (a).

There is a statistical uncertainty related to the fitted correction funtion $G(n_{\text{trk}})$ and coming from the uncertainties of the fit parameters. Correlation matrix of the fit parameters (see Table B.4) shows that parameters a, b and c are strongly correlated which has to be considered in a proper estimation of the error – one has to use the covariance matrix of the fit parameters (see Table B.5).

Table B.4: The correlation matrix of the fit parameters of the correction function $G(n_{\text{trk}})$

	a	b	c	d
a	1	-0.99	-0.97	-0.52
b	-0.99	1	0.99	0.59
c	-0.97	0.99	1	0.64
d	-0.52	0.59	0.64	1

Table B.5: The covariance matrix of the fit parameters of the correction function $G(n_{\text{trk}})$

	a	b	c	d
a	9359	-14	-2.1	-0.64
b	-14	0.022	0.0033	0.0011
c	-2.1	0.0033	0.00051	0.00018
d	-0.64	0.0011	0.00018	0.00016

The statistical uncertainty of the correction function $G(n_{\text{trk}})$ is given by:

$$\widetilde{\sigma}_{\mathrm{G}}(n_{\text{trk}}) = \sqrt{\sum_{i=1}^{4}\sum_{j=1}^{4} \frac{\partial G(n_{\text{trk}})}{\partial x_i} \cdot \frac{\partial G(n_{\text{trk}})}{\partial x_j} \cdot \operatorname{cov}\left(x_i, x_j\right)}\,, \tag{B.4}$$

where $\vec{x} = \begin{pmatrix} a, & b, & c, & d \end{pmatrix}$ and the partial derivatives can be easily calculated.

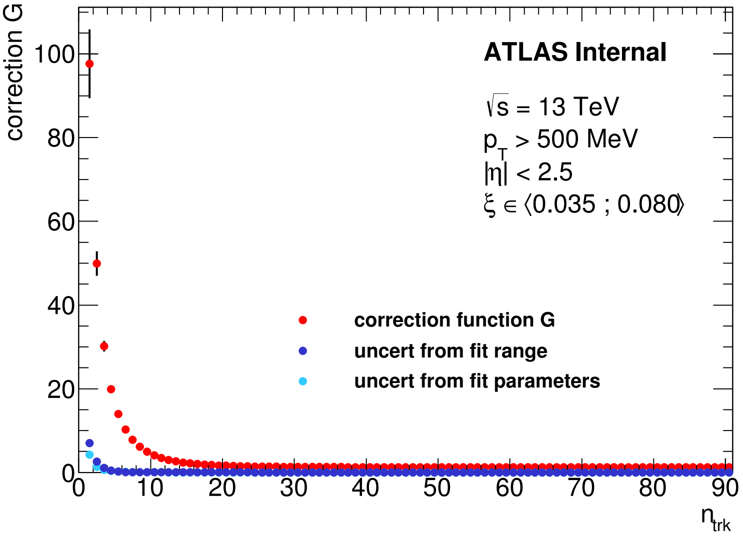

Figure B.10: Red dots represent values of the correction function G. Uncertainty on these points was obtained adding in quadrature the uncertainties due to the fit range (dark blue points, in text denoted as σ_{G}) and those due to the fit parameters (light blue points, in text denoted as $\widetilde{\sigma}_{\mathrm{G}}$).

Fig. B.10 illustrates a correction function $G(n_{\mathrm{trk}})$ together with the uncertainties $\sigma_{\mathrm{G}}(n_{\mathrm{trk}})$ and $\widetilde{\sigma}_G(n_{\mathrm{trk}})$.

APPENDIX C

AFP DCS FSM PANELS

The AFP DSC System is built based on a Finite State Machine (FSM) tool [96]. The FSM tool is used to create a view of the detector as a hierarchical, tree-like structure of well-defined subsystems – FSM nodes (see Fig. C.1). What is more, each FSM node has a set of well-defined possible states and statuses (see Fig. C.2).

The FSM enables full control of the detector hierarchy and serves as a graphical user interface for the operator. The author of this dissertation was responsible for the design and implementation of the AFP FSM panels for few AFP FSM nodes:

1. AFP,
2. infrastructure,
3. arms A and C,
4. Near and Far stations,
5. arm infrastructure,
6. Roman Pot (RPH),
7. SiT,
8. ToF,
9. TDB.

Each panel consists of several parts (see C.3):

- navigation through the detector hierarchy,

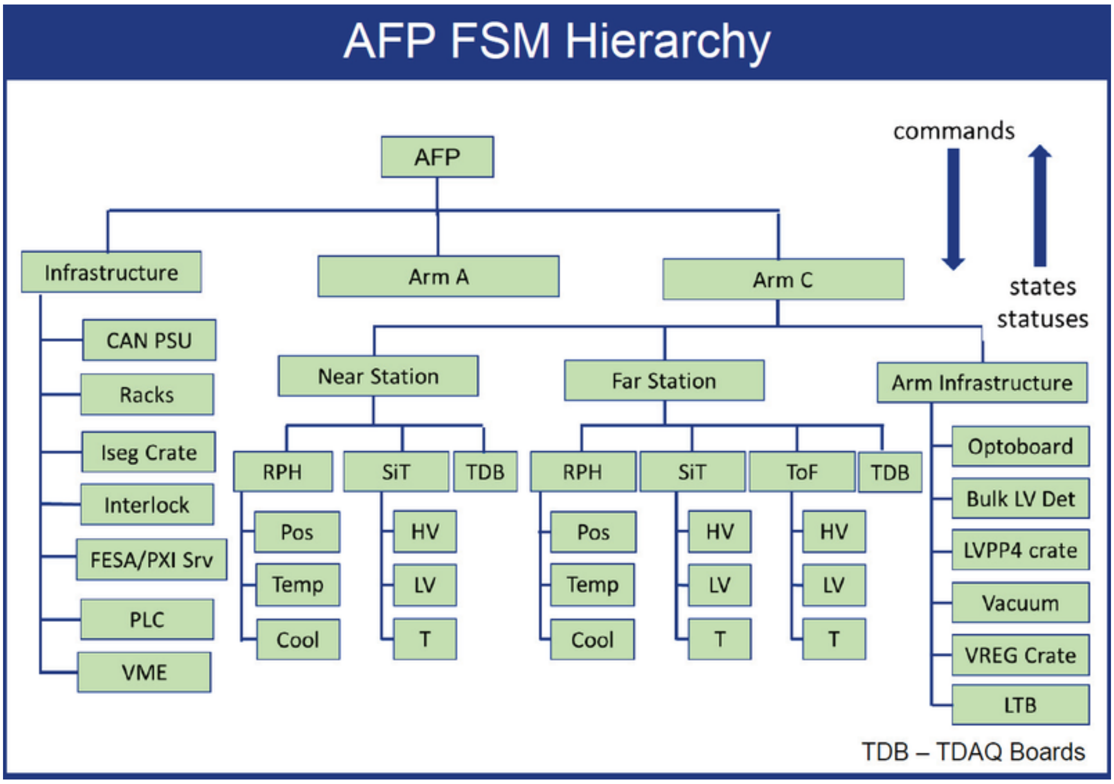

Figure C.1: FSM hierarchy of the AFP detector. Each of the green rectangles represents separate FSM node. Commands issued by the detector operator propagate downwards whilst states and statuses of the FSM nodes – upwards. From [77].

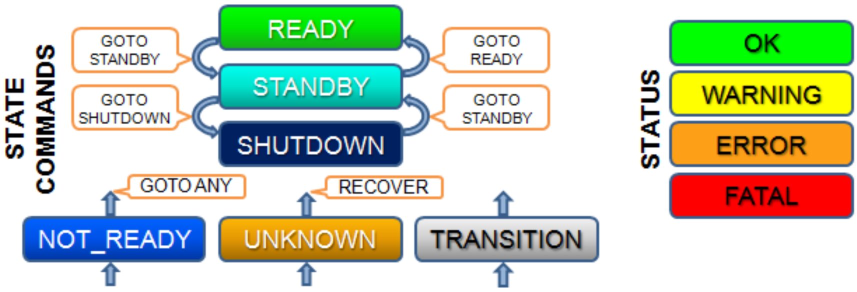

Figure C.2: Possible states and statuses of the AFP FSM node.

- main panel showing the parameters of a selected FSM node,
- secondary panel presenting the most important parameters of a selected FSM node.

Example of main and secondary panels for the FSM node AFP are presented in Figs. C.4 and C.5.

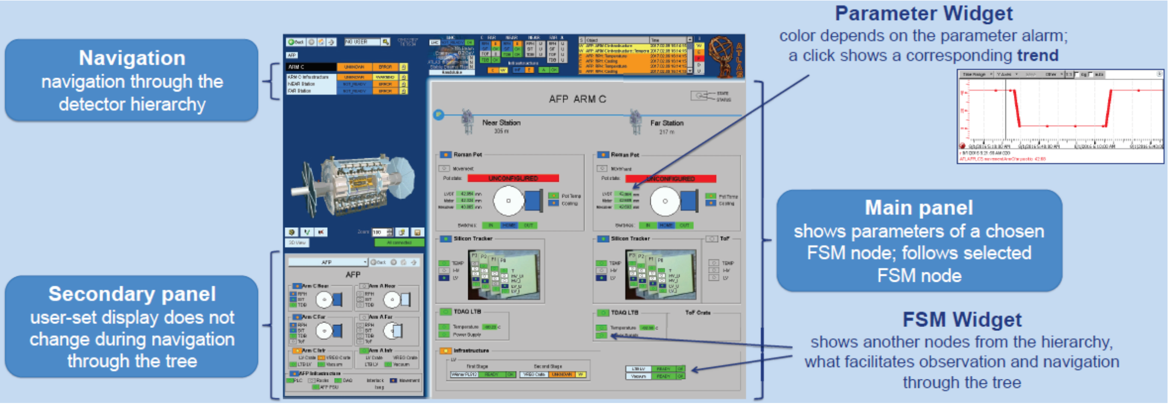

Navigation
navigation through the detector hierarchy

Secondary panel
user-set display does not change during navigation through the tree

Parameter Widget
color depends on the parameter alarm; a click shows a corresponding **trend**

Main panel
shows parameters of a chosen FSM node; follows selected FSM node

FSM Widget
shows another nodes from the hierarchy, what facilitates observation and navigation through the tree

Figure C.3: View of the AFP FSM panel and its main parts.

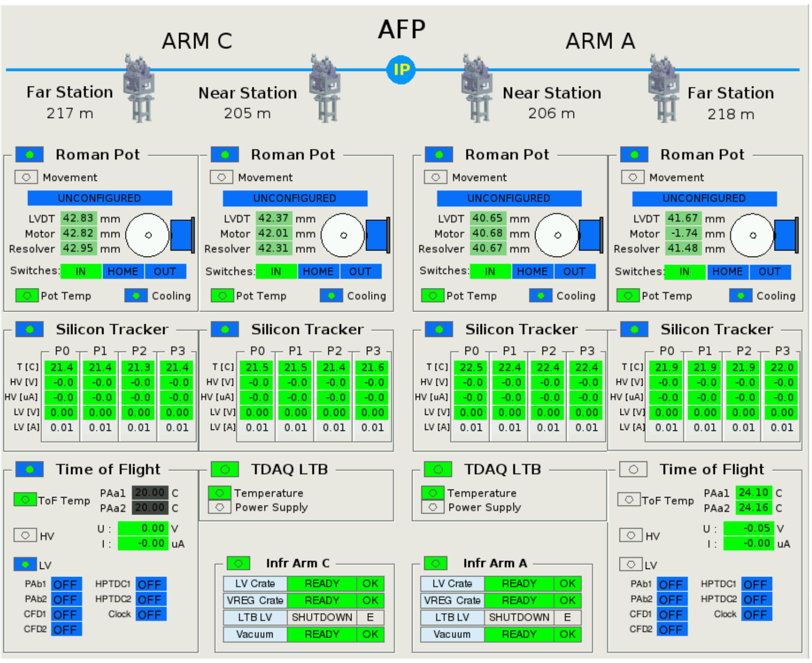

AFP

ARM C

Far Station 217 m | Near Station 205 m

ARM A

Near Station 206 m | Far Station 218 m

Roman Pot

	Far Station (ARM C)	Near Station (ARM C)	Near Station (ARM A)	Far Station (ARM A)
Movement	UNCONFIGURED	UNCONFIGURED	UNCONFIGURED	UNCONFIGURED
LVDT [mm]	42.83	42.37	40.65	41.67
Motor [mm]	42.82	42.01	40.68	-1.74
Resolver [mm]	42.95	42.31	40.67	41.48
Switches:	IN HOME OUT	IN HOME OUT	IN HOME OUT	IN HOME OUT

Silicon Tracker

	P0	P1	P2	P3	P0	P1	P2	P3	P0	P1	P2	P3	P0	P1	P2	P3
T [C]	21.4	21.4	21.3	21.4	21.5	21.5	21.4	21.6	22.5	22.4	22.4	22.4	21.9	21.9	21.9	22.0
HV [V]	-0.0	-0.0	-0.0	-0.0	-0.0	-0.0	-0.0	-0.0	-0.0	-0.0	-0.0	-0.0	-0.0	-0.0	-0.0	-0.0
HV [uA]	-0.0	-0.0	-0.0	-0.0	-0.0	-0.0	-0.0	-0.0	-0.0	-0.0	-0.0	-0.0	-0.0	-0.0	-0.0	-0.0
LV [V]	0.00	0.00	0.00	0.00	0.00	0.00	0.00	0.00	0.00	0.00	0.00	0.00	0.00	0.00	0.00	0.00
LV [A]	0.01	0.01	0.01	0.01	0.01	0.01	0.01	0.01	0.01	0.01	0.01	0.01	0.01	0.01	0.01	0.01

Time of Flight (ARM C)

ToF Temp: PAa1 20.00 C, PAa2 20.00 C
HV: U : 0.00 V, I : -0.00 uA
LV: PAb1 OFF, PAb2 OFF, CFD1 OFF, CFD2 OFF, HPTDC1 OFF, HPTDC2 OFF, Clock OFF

TDAQ LTB: Temperature, Power Supply

TDAQ LTB: Temperature, Power Supply

Time of Flight (ARM A)

ToF Temp: PAa1 24.10 C, PAa2 24.16 C
HV: U : -0.05 V, I : -0.00 uA
LV: PAb1 OFF, PAb2 OFF, CFD1 OFF, CFD2 OFF, HPTDC1 OFF, HPTDC2 OFF, Clock OFF

Infr Arm C

LV Crate	READY	OK
VREG Crate	READY	OK
LTB LV	SHUTDOWN	E
Vacuum	READY	OK

Infr Arm A

LV Crate	READY	OK
VREG Crate	READY	OK
LTB LV	SHUTDOWN	E
Vacuum	READY	OK

Figure C.4: Main FSM panel for the whole AFP detector.

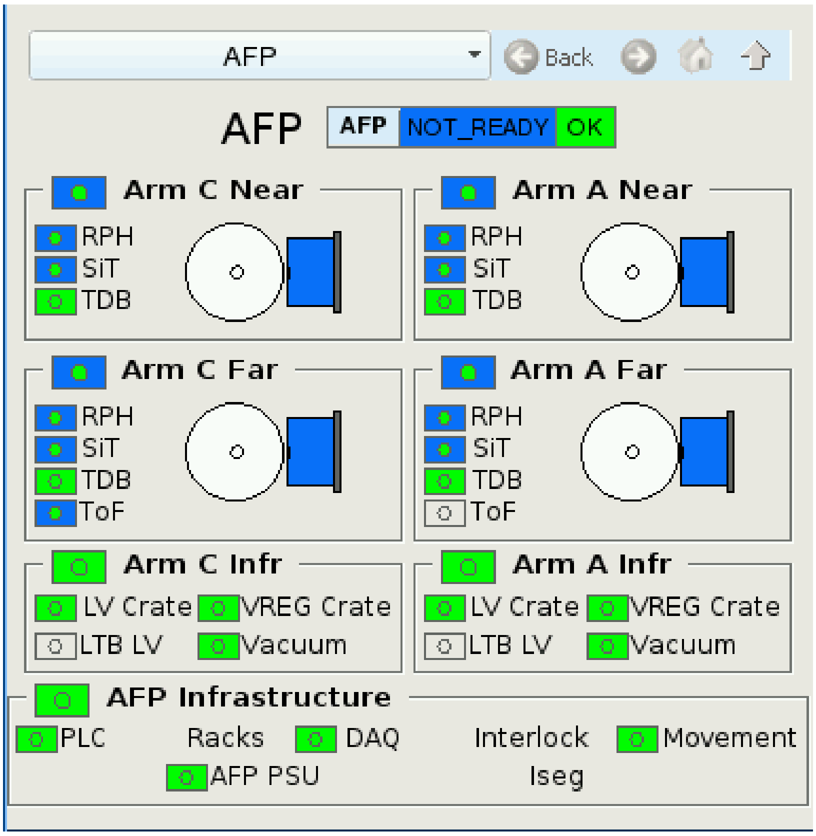

Figure C.5: Secondary FSM panel for the whole AFP detector.

BIBLIOGRAPHY

[1] University of Zurich. Standard Model. `https://www.physik.uzh.ch/en/researcharea/lhcb/outreach/StandardModel.html`. Accessed: 2019-04-16.

[2] G. J. Saraiva. Jet and photon measurements from ATLAS. In *EPJ Web of Conferences*, volume 60, page 14007, Nov 2013.

[3] M. Delmastro. Hadronisation. https://www.borborigmi.org/2012/06/28/rivelatori-di-particelle-a-lhc-ottava-parte-spray-di-particelle-ovvero-come-si-vedono-quark-e-gluoni/. Accessed: 2019-04-16.

[4] M. L. Good and W. D. Walker. Diffraction disssociation of beam particles. *Phys. Rev.*, 120:1857–1860, 1960.

[5] K. A. Goulianos. Diffraction in hadron-hadron interactions. *Nucl. Phys. Proc. Suppl.*, 99A:9–20, 2001.

[6] L. Adamczyk et al. Technical Design Report for the ATLAS Forward Proton Detector. Technical Report CERN-LHCC-2015-009, ATLAS-TDR-024, CERN, Geneva, May 2015.

[7] G. Matthiae. Diffractive physics at the LHC. *Brazilian Journal of Physics*, 30:244 – 250, Jun 2000.

[8] K. A. Goulianos. Diffractive Interactions of Hadrons at High-Energies. *Phys. Reports*, 101:169, 1983.

[9] ATLAS Collaboration. Measurement of Differential Cross Sections for Single Diffractive Dissociation in $\sqrt{s} = 8$ TeV pp collisions using the ATLAS ALFA Spectrometer. Technical Report ATLAS-CONF-2019-012, CERN, Geneva, Apr 2019.

[10] G. Arnison et al. Transverse momentum spectra for charged particles at the CERN proton-antiproton collider. *Phys. Lett. B*, 118(1):167 – 172, 1982.

[11] F. Abe et al. Transverse-momentum distributions of charged particles produced in $\overline{p}p$ interactions at $\sqrt{s} = 630$ and 1800 GeV. *Phys. Rev. Lett.*, 61:1819–1822, Oct 1988.

[12] T. Alexopoulos et al. Multiplicity dependence of transverse momentum spectra of centrally produced hadrons in $\overline{p}p$ collisions at 0.3, 0.54, 0.9, and 1.8 TeV center-of-mass energy. *Phys. Lett. B*, 336(3):599 – 604, 1994.

[13] J. Adam et al. Pseudorapidity and transverse-momentum distributions of charged particles in proton–proton collisions at $\sqrt{s} = 13$ TeV. *Phys. Lett. B*, 753:319–329, 2016.

[14] ATLAS Collaboration. Charged-particle distributions in $\sqrt{s}$ = 13 TeV pp interactions measured with the ATLAS detector at the LHC. *Phys. Lett. B*, 758:67–88, 2016.

[15] S. Donnachie, G. Dosch, P. Landshoff and O. Nachtmann. *Pomeron Physics and QCD*. Cambridge Monographs on Particle Physics, Nuclear Physics and Cosmology. Cambridge University Press, 2002.

[16] P. Collins. *An Introduction to Regge Theory and High Energy Physics*. Cambridge Monographs on Mathematical Physics. Cambridge University Press, 1977.

[17] M. Poghosyan. An introduction to Regge Field Theory. `http://school-diff2013.physi.uni-heidelberg.de/Talks/Poghosyan.pdf`, Sept 2013. Accessed: 2019-04-15.

[18] H. Abramowicz and A. Caldwell. HERA collider physics. *Rev. Mod. Phys.*, 71:1275–1410, 1999.

[19] A. Grau, G. Pancheri, O. Shekhovtsova and Y.N. Srivastava. Modeling pion and proton total cross-sections at LHC. *Phys. Lett. B*, 693(4):456 – 461, 2010.

[20] V. N. Gribov. Possible Asymptotic Behavior of Elastic Scattering. *JETP Lett.*, 41:667–669, 1961.

[21] A. Donnachie and P. V. Landshoff. Total cross-sections. *Phys. Lett. B*, 296:227–232, 1992.

[22] A. Donnachie and P. V. Landshoff. pp and $\bar{\text{p}}$p elastic scattering. *Nucl. Phys. B*, 231(2):189 – 204, 1984.

[23] R. Bonino et al. Evidence for transverse jets in high mass diffraction. *Phys. Lett. B*, 211(CERN-EP-88-60):239–246. 13 p, May 1988.

[24] A. Brandt et al. Evidence for a super-hard Pomeron structure. *Phys. Lett. B*, 297(CERN-PPE-92-179):417–424. 15 p, Oct 1992.

[25] G. Watt. MSTW PDFs and impact of PDFs on cross sections at Tevatron and LHC. *Nucl. Phys. Proc. Suppl.*, 222-224:61–80, 2012.

[26] H.-L. Lai et al. New parton distributions for collider physics. *Phys. Rev. D*, 82:074024, 2010.

[27] P. Jimenez-Delgado and E. Reya. Dynamical NNLO parton distributions. *Phys. Rev. D*, 79:074023, 2009.

[28] T. Sjöstrand. Monte Carlo Generators. In *High-energy physics. Proceedings, European School, Aronsborg, Sweden, June 18-July 1, 2006*, number CERN-LCGAPP-2006-06, pages 51–74, 2006.

[29] C. Patrignani et al. Review of Particle Physics. *Chin. Phys. C*, 40(10):100001, 2016.

[30] T. Sjöstrand et al. An Introduction to PYTHIA 8.2. *Comput. Phys. Commun.*, 191:159–177, 2015.

[31] S. Navin. Diffraction in Pythia. (LUTP-09-23, MCNET-10-09), 2010.

[32] ATLAS Collaboration. Further ATLAS tunes of PYTHIA6 and Pythia 8. Technical Report ATL-PHYS-PUB-2011-014, CERN, Geneva, Nov 2011.

[33] A. Sherstnev and R. S. Thorne. Parton Distributions for LO Generators. *Eur. Phys. J. C*, 55:553–575, 2008.

[34] T. Sjöstrand et al. Tunes of PYTHIA. `http://home.thep.lu.se/Pythia/pythia82html/Tunes.html`. Accessed: 2019-03-12.

[35] S. Porteboeuf, T. Pierog and K. Werner. Producing Hard Processes Regarding the Complete Event: The EPOS Event Generator. In *Proceedings, 45th Rencontres de Moriond on QCD and High Energy Interactions: La Thuile, Italy, March 13-20, 2010*, pages 135–140. Gioi Publishers, 2010.

[36] T. Pierog, Iu. Karpenko, J.M. Katzy, E. Yatsenko and K. Werner. EPOS LHC: Test of collective hadronization with data measured at the CERN Large Hadron Collider. *Phys. Rev. C*, 92(3):034906, 2015.

[37] S. Agostinelli et al. Geant4 – a simulation toolkit. *Nucl. Instrum. Meth. A*, 506:250–303, 2003.

[38] ATLAS Collaboration. The ATLAS Simulation Infrastructure. *Eur. Phys. J. C*, 70:823–874, 2010.

[39] L. Evans and P. Bryant. LHC Machine. *JINST*, 3:S08001, 2008.

[40] S. Myers and E. Picasso. The design, construction and commissioning of the CERN large Electron–Positron collider. *Contemporary Physics*, 31(6):387–403, 1990.

[41] J. Wenninger. Interaction Points. https://www.researchgate.net/figure/Layout-of-the-LHC-with-the-eight-interaction-points-labelled-IP1-to-IP8-The-experiments_fig1_306186204. Accessed: 2019-03-12.

[42] ATLAS Collaboration. The ATLAS Experiment at the CERN Large Hadron Collider. *JINST*, 3:S08003, 2008.

[43] S. Chatrchyan et al. The CMS Experiment at the CERN LHC. *JINST*, 3:S08004, 2008.

[44] K. Aamodt et al. The ALICE experiment at the CERN LHC. *JINST*, 3:S08002, 2008.

[45] A. A. Alves Jr. et al. The LHCb Detector at the LHC. *JINST*, 3:S08005, 2008.

[46] G. Anelli et al. The TOTEM experiment at the CERN Large Hadron Collider. *JINST*, 3:S08007, 2008.

[47] O. Adriani et al. The LHCf detector at the CERN Large Hadron Collider. *JINST*, 3:S08006, 2008.

[48] J. Pinfold et al. Technical Design Report of the MoEDAL Experiment. Technical Report CERN-LHCC-2009-006. MoEDAL-TDR-001, Jun 2009.

[49] J. Wenninger and M. Hostettler. Colliding angle. `https://home.cern/news/news/accelerators/lhc-report-colliding-angle`. Accessed: 2019-03-12.

[50] M. Trzebiński. Machine Optics Studies for the LHC Measurements. *Proc. SPIE Int. Soc. Opt. Eng.*, 9290:929026, 2014.

[51] ATLAS Collaboration. Luminosity Determination in pp collisions at $\sqrt{s} = 7$ TeV using the ATLAS Detector at the LHC. *Eur. Phys. J. C*, 71:1630, 2011.

[52] CMS Collaboration. Coordinate system. `https://wiki.physik.uzh.ch/cms/_media/latex:cms_coordinate_system.png`. Accessed: 2019-03-12.

[53] ATLAS Collaboration. *ATLAS inner detector: Technical design report. Vol. 1.* Number CERN-LHCC-97-16, ATLAS-TDR-4 in Technical Design Report ATLAS. CERN, Geneva, 1997.

[54] ATLAS Collaboration. Inner Detector. `http://atlasexperiment.org/inner_detector.htm`. Accessed: 2019-03-12.

[55] T. G. Cornelissen. *Track Fitting in the ATLAS Experiment.* PhD thesis, Amsterdam U., 2006.

[56] Y. Takubo. The Pixel Detector of the ATLAS experiment for the Run2 at the Large Hadron Collider. *JINST*, 10(02):C02001, 2015.

[57] ATLAS Collaboration. Operation and performance of the ATLAS semiconductor tracker. *JINST*, 9:P08009, 2014.

[58] A. Vogel. ATLAS Transition Radiation Tracker (TRT): Straw tube gaseous detectors at high rates. *Nucl. Instrum. Meth. A*, 732:277–280, 2013.

[59] Dolgoshein, B. Transition radiation detectors. *Nucl. Instrum. Meth. A*, 326:434–469, 1993.

[60] ATLAS Collaboration. *ATLAS liquid argon calorimeter: Technical design report*. Technical Design Report ATLAS. CERN, Geneva, 1996.

[61] ATLAS Collaboration. *ATLAS tile calorimeter: Technical design report*. Technical Design Report ATLAS. CERN, Geneva, 1996.

[62] ATLAS Collaboration. Topological cell clustering in the ATLAS calorimeters and its performance in LHC Run 1. *Eur. Phys. J. C*, F77:490, 2017.

[63] J.J. Goodson. *Search for Supersymmetry in States with Large Missing Transverse Momentum and Three Leptons including a Z-Boson*. PhD thesis, Stony Brook University, May 2012. Presented 17 Apr 2012.

[64] ATLAS Collaboration. *ATLAS muon spectrometer: Technical Design Report*. Number CERN-LHCC-97-022 in Technical Design Report ATLAS. CERN, Geneva, 1997.

[65] ATLAS Collaboration. Muon reconstruction performance in early $\sqrt{s} = 13$ TeV data. Technical Report ATL-PHYS-PUB-2015-037, CERN, Geneva, Aug 2015.

[66] ATLAS Collaboration. TDAQ. `https://atlas.cern/discover/detector/trigger-daq`. Accessed: 2019-03-12.

[67] L. Fabbri. Forward Detectors in ATLAS: LUCID, ZDC and ALFA. In *Proceedings, 17th International Workshop on Deep-Inelastic Scattering and Related Subjects (DIS 2009): Madrid, Spain, April 26-30, 2009*, page 166, Berlin, Germany, 2009. Science Wise Publ.

[68] A. Sidoti. Minimum Bias Trigger Scintillators in ATLAS Run II. *JINST*, 9(10):C10020, 2014.

[69] M. Bruschi. The ATLAS luminosity monitor. *Nucl. Instrum. Meth. A*, 623:371–373, 2010.

[70] G. Avoni et al. The new LUCID-2 detector for luminosity measurement and monitoring in ATLAS. *JINST*, 13(07):P07017, 2018.

[71] P. Jenni, M. Nessi and M. Nordberg. Zero degree calorimeters for ATLAS. Technical Report CERN-LHCC-2007-001, LHCC-I-016, CERN, Geneva, Jan 2007.

[72] P. Jenni, M. Nordberg, M. Nessi and K. Jon-And. *ATLAS Forward Detectors for Measurement of Elastic Scattering and Luminosity*. Number ATLAS-TDR-18, CERN-LHCC-2008-004 in Technical Design Report ATLAS. CERN, Geneva, 2008.

[73] ATLAS Collaboration. Measurement of the total cross section from elastic scattering in pp collisions at $\sqrt{s} = 7$ TeV with the ATLAS detector. *Nucl. Phys. B*, 889:486–548, 2014.

[74] I. Raynova. Collimators description. `https://home.cern/news/news/experiments/collimators-lhcs-bodyguards`. Accessed: 2019-03-12.

[75] The AFP group. AFP figures. `https://twiki.cern.ch/twiki/bin/view/Atlas/AFP_Figures`. Accessed: 2019-04-04.

[76] J. Lange et al. Beam tests of an integrated prototype of the ATLAS Forward Proton detector. *JINST*, 11(09):P09005, 2016.

[77] E. Banaś et al. Detector Control System for the AFP detector in ATLAS experiment at CERN. *J. Phys. Conf. Ser.*, 898(3):032022, 2017.

[78] B. Dehning. Beam Loss Monitors at LHC. In *Proceedings, 2014 Joint International Accelerator School: Beam Loss and Accelerator Protection: Newport Beach, CA, USA, November 5-14, 2014*, pages 303–318, 2016.

[79] K. Korcyl, M. Kocian, I. L. Paz and G. Avoni. Readout and Trigger for the AFP Detector at the ATLAS Experiment at LHC. *J. Phys. Conf. Ser.*, 898(3):032025, 2017.

[80] I. L. Paz. *The one-armed ATLAS Forward Proton detector*. PhD thesis, Mar 2018. Presented 22 May 2018.

[81] T. Cornelissen et al. Concepts, Design and Implementation of the ATLAS New Tracking (NEWT). Technical Report ATL-SOFT-PUB-2007-007, ATL-COM-SOFT-2007-002, CERN, Geneva, Mar 2007.

[82] ATLAS Collaboration. Performance of the ATLAS Inner Detector Track and Vertex Reconstruction in the High Pile-Up LHC Environment. Technical Report ATLAS-CONF-2012-042, CERN, Geneva, Mar 2012.

[83] G. Welch and G. Bishop. An Introduction to the Kalman Filter. *Proc. Siggraph Course*, 8, 1995.

[84] R. Castaldi. Tracking at LHC (Calibration and Alignment). `http://www.le.infn.it/lhcschool/talks2010/Lecture2_FV.pdf`. Accessed: 2019-04-02.

[85] R. O. Duda and P. E. Hart. Use of the Hough Transformation to Detect Lines and Curves in Pictures. *Commun. ACM*, 15(1):11–15, Jan 1972.

[86] ATLAS Collaboration. Performance of primary vertex reconstruction in proton-proton collisions at $\sqrt{s}$ =7 TeV in the ATLAS experiment. Technical Report ATLAS-CONF-2010-069, CERN, Geneva, Jul 2010.

[87] W. Lampl et al. Calorimeter clustering algorithms: Description and performance. Technical Report ATL-LARG-PUB-2008-002, ATL-COM-LARG-2008-003, CERN, Geneva, Apr 2008.

[88] J. C. Collins. Light cone variables, rapidity and all that. (hep-ph/9705393), May 1997.

[89] ATLAS Collaboration. Dijet production in $\sqrt{s} = 7$ TeV pp collisions with large rapidity gaps at the ATLAS experiment. *Phys. Lett. B*, 754:214–234, 2016.

[90] F. Schmidt. Mad-X User's Guide. `http://mad.web.cern.ch/mad`, 2005. Accessed: 2019-03-12.

[91] P. Bussey. FPTrack Programme. `http://www.physics.gla.ac.uk/~bussey/FPTRACK`. Accessed: 2019-03-12.

[92] R. Staszewski and J. Chwastowski. Transport Simulation and Diffractive Event Reconstruction at the LHC. *Nucl. instrum. meth. A*, 609:136–141, 2009.

[93] F. James. Minuit description. `https://root.cern.ch/sites/d35c7d8c.web.cern.ch/files/minuit.pdf`. Accessed: 2019-03-12.

[94] G. D'Agostini. A Multidimensional unfolding method based on Bayes' theorem. *Nucl. Instrum. Meth. A*, 362:487–498, 1995.

[95] I. L. Paz. Proton tagging with the one arm AFP detector. Technical Report ATL-PHYS-PUB-2017-012, CERN, Geneva, Jul 2017.

[96] Wikipedia. Finite State Machine. `https://en.wikipedia.org/wiki/Finite-state_machine`. Accessed: 2019-06-13.